8-2022

Studies on Magnetic Kagome Metals

Rui Xue
rxue@vols.utk.edu

To the Graduate Council:

I am submitting herewith a dissertation written by Rui Xue entitled "Studies on Magnetic Kagome Metals." I have examined the final electronic copy of this dissertation for form and content and recommend that it be accepted in partial fulfillment of the requirements for the degree of Doctor of Philosophy, with a major in Physics.

David Mandrus, Major Professor

We have read this dissertation and recommend its acceptance:

Cristian Batista, Jian Liu, Haidong Zhou

Accepted for the Council:

Dixie L. Thompson

Vice Provost and Dean of the Graduate School

(Original signatures are on file with official student records.)

Studies on Magnetic Kagome Metals

A Dissertation Presented for the

Doctor of Philosophy

Degree

The University of Tennessee, Knoxville

Rui Xue

August 2022

To my parents, Tao Xue and Junli Zhang

Acknowledgements

I would like to express my most profound appreciation to my advisor, Prof. David Mandrus, for leading me into the magnificent research world. Dr. Mandrus has always been so supportive and encouraging to all his students. During my Ph.D., Dr. Mandrus inspired me with his creative mind. Thanks to him, I dare to take on challenges and accomplish tasks that seem impossible. I really enjoyed the time he spent teaching me about the hardware building for our cryostats and arc-melter. It was a precious memory that I will carefully keep in my mind.

I want to thank Dr. Takahiro Matsuoka in our group. He is so knowledgeable and warm-hearted. He taught me so many instrument-building basics. He is my mentor in designing measurement systems. I always learn so many things from our discussions. Working with Dr. Matsuoka is one of my best memory in our labs.

I am grateful to Prof. Cristian Batista, Prof. Jian Liu, and Prof. Haidong Zhou as my doctoral dissertation committee. Their advice is beneficial and inspiring.

I would like to thank my collaborators: Dr. Feng Ye Dr. Jiaqiang Yan, Dr. Raphael Hermann, Dr. James Torres, and Dr. Veerle Keppens. They have been accommodating and supportive of my Ph.D. thesis work.

I can not finish my Ph.D. work without help from our research group members. Thanks to (soon to be) Dr. Hasitha Suriya Arachchige, Dr. Nan Huang, and Dr. Candice Kinsler-Fedon. The friendship we established is rigid and valuable.

I want to thank all my friends. They gave me the strength to march on while I was in depression and started to doubt myself. Thanks to Dr. Qing Huang for his listening and

accompanying. Thanks to Ruike He and Dr. Feihu Xi for their caring like my real sister and brother. Thanks to Cheng-Ru Chang for being an important role in my PhD life.

Finally, I want to thank my family for their love and support, specially my cousin, Zheng Duan. I appreciate him visiting me from time to time and bring me the warmth from our family. Also, I want to thank my cat Luna for being my beloved fur baby.

Abstract

Magnetic kagome lattice compound has drawn much attention with their high possibilities of holding the unique magnetic structures, which bring enormous extraordinary physics phenomena, such as frustrated magnetism, electronic correlation, and topological electronic structure. In this study, rare earth compounds RMn_6Sn_6 (R = Y, Sc, Lu) are investigated. The Topological Hall effect was proved to be a common figure in those three materials. Also, they all have a complicated magnetic phase competing before spin saturation. Magnetization, electrical transport, and transverse properties of those materials are explored. Type-II Weyl semimetal $Co_3Sn_2S_2$ is also studied using Resonant Ultrasound spectroscopy(RUS). From previous studies, a transition in $Co_3Sn_2S_2$ around 125 K was under debate. Our RUS result shows a high sensitivity to ultrasound frequency changes at the transition temperature. Also, the elastic modulus as a function of temperature is studied. By performing those studies on our kagome metals, a better understanding of the relationship between the magnetic structure and intrinsic physical properties will be established.

Table of Contents

List of Tables

List of Figures

Chapter 1

Introduction

This chapter will give a brief overview of topological kagome metals. Firstly, a background review of topological materials with the motivation of studying topological materials is stated. Then, the background of kagome metals is presented. After that, study cases like 166 rare earth compounds and Weyl semimetals are introduced.

1.1 Topological materials

Research on topological materials has been the most extraordinary study in condensed matter physics in the past few decades [1–3]. One early discovery of topological materials is the Topological insulator(TI). TIs were theoretically predicted and experimentally proved in both two-dimensional and three-dimensional materials. [4–6] HgTe and Bi_2Se_3 are famous examples [7–10]. From former prediction work, TI's abnormal band structure shows a full energy gap in bulk and no gap on the surface. This band structure leads to insulation in bulk and conducting on the surface of TIs. Moreover, this bizarre band structure is topologically protected by time-reversal symmetry [11, 12]. TI's topological properties will be rigid despite the material's shape and dimensions. The discovery of TI has opened a gate for research focused on topological materials. Investigations on other topological

materials were constantly brought out. Tremendous topological quantum phenomena are experimentally discovered and theoretically explained.

Another famous example is Weyl and Dirac semimetals. They attracted attention by presenting their linearly dispersed electric band structure. It is referred to as the Dirac cone [13, 14]. The cross point of Dirac cones is named Weyl point. With the influence of Spin-orbital coupling(SOC), a Weyl semimetal will form when the time-reversal symmetry or inversion-symmetry is broken. Weyl points inside Weyl semimetals come in pairs and have opposite chirality. Thus, Weyl semimetal provided an excellent platform for Berry curvature, which function as topological magnons [15, 16]. A variety of exotic electromagnetic properties are discovered in Weyl semimetals due to Berry curvatures, such as the anomalous Hall effect(AHE) and anomalous Nernst effect(ANE) [17, 18]. For instance, $Co_3Sn_2S_2$ is a well-known Weyl semimetal. Both its Anomalous Hall effect and Anomalous Nernst effect are predicted to be non-trivial theoretically and discovered experimentally [19]. Berry curvature causes a fictitious magnetic field in momentum space and roots the ANE and AHE.

The motivation pushing scientists to research topological materials is the potential to revolutionize the technical field. Topological materials would be a candidate for building next-generation information storage instruments [20, 21]. Topological materials can host multiple electronic states simultaneously. As a result, they are also expected to create quantum bits and help build quantum computers [22, 23].

1.2 Kagome magnets

The kagome structure is a hexagonal mesh lattice that is named from the traditional Japanese woven bamboo pattern, with the same structure containing hexagons and corner shared triangles [24]. Fig.1.1 is a plot of kagome net. Kagome systems have been attracting interest for many reasons. In insulators, the kagome net is highly magnetically frustrated and is believed to be an excellent platform to search for quantum spin liquids. Herbertsmithite,

for example, is a kagome system [2, 25]. The kagome magnets are materials with kagome lattices consisting of magnetic ions.

In recent years, studies found that kagome metals have provided a great platform to study electrically correlated topological materials. It was both theoretically and experimentally proven that both Dirac and flat-band exist simultaneously in lots of kagome metals, such as Fe_3Sn_2, FeSn and YMn_6Sn_6 [26–29] (See Fig.1.2). Investigating them is believed to be a promising approach to introducing strong correlations into topological band structures. kagome metals have also drawn a lot of attention with their high possibilities of holding magnetic structures bringing enormous number of special physics properties, such as frustrated magnetism, electronic correlation, and topological electronic structure [30]. Moreover, in recent years, successful investigations have shown that kagome metals are able to host the magnetic frustration which will promote a topologically nontrivial spin state, i.e., magnetic skyrmions [31]. There are two types of skymions, Néel type, and Bloch type. They both have the center spin pointing down and edge spin pointing up.

1.3 Study cases

We are interested in finding topological magnon states in kagome magnets. Two groups of materials had attracted our attention and we found they are promising. One is 166 rare-earth compounds another is Weyl semimetal $Co_3Sn_2S_2$.

1.3.1 166 rare-earth compound

166 rare earth compounds were slightly studied in the 1990s. In previous research, experiments are mainly focused on magnetization and detection of their magnetic spin structures. 166 rare earth compounds have the chemical formula of one rare earth metal, six 3d transition metals, and six nonmagnetic metals such as Sn, In, Ge, and Ga.

Very recently, one subgroup in 166 compounds has become a new hot spot in topological materials. It is the RMn_6Sn_6 group. R is a representation of nonmagnetic rare earth Y, Lu,

and Sc. RMn_6Sn_6 are layered materials; they belong to P6/mmm group [32]. Mn is the only magnetic ion. Mn forms magnetic layers along the crystal's ab plane. YMn_6Sn_6 was the first one to be looked into. It was reported to host a large near room temperature topological Hall effect [33, 34]. YMn_6Sn_6 is an AFM with a Neél temperature $T_N = 345$ K. Below that temperature, it will form a colinear AFM structure above 333 K. In the AFM temperature window, Mn forms an inner layer ferromagnetic structure. However, at the inter-layer level, Mn layers have an anti-parallel spin with their neighbor layers.

1.3.2 YMn_6Sn_6 spin structure and Topological Hall effect

Because of the complexity of magnetic kagome lattice, YMn_6Sn_6 have a variety of magnetic spin structures. A systematic study about YMn_6Sn_6 spin structure and the Topological Hall effect is provided in [33]. Their research tested electromagnetic transport to confirm that their sample has the large Topological Hall effect. Then neutron diffraction was performed with and without a magnetic field.

From their experiment result, they claimed that at the ground state, Mn layers in YMn_6Sn_6 show a "double flat spiral" structure as proposed decades ago [32, 35]. It means along the sample's c axis, Mn has an inner layer FM state. However, the spin angles difference between Mn layers is in the order of α - β - α - β. The angle between two Mn layers have the Y in between is β. The angle between two Mn layers absent of Y is α. They follow this relationship $\alpha + \beta = 90°$.(See Fig.1.3)

When a magnetic field gets involved, the Mn spin structure will travel through multiple phases before saturating. A clear phase diagram was provided to show the spin states at different temperatures and magnetic fields. (See Fig 1.4) There are, in total, four spin states found inside YMn_6Sn_6, which are "distorted spiral"(DS), "transverse conical spiral"(TCS), "fan-like"(FL), and "forced FM"(FF). A cartoon also explains the spin direction and nature during every state. (Fig 1.5) Among those magnetic states, large THE are only found in the TCS state. Theoretical work was performed based on the TCS state. With continuous approximation, the TCS state can hold an extra component in the direction perpendicular

to the external field. As a result, a topological chiral field will be provided. Thus THE arises(Fig. 1.6).

This discovery opened an avenue for detecting the topology in RMn_6Sn_6. We have the curiosity to figure out if $LuMn_6Sn_6$ and $ScMn_6Sn_6$ have similar topological properties. To answer the question, we performed magnetization, electromagnetic transport, and neutron diffraction measurements on RMn_6Sn_6. The result and details will be explained in Chapter 3.

1.3.3 Weyl semimetal

As mentioned previously, Weyl semimetals have unique band structures in which the conducting band and the valence band overlap each other on the Weyl points in momentum space. There are two types of Weyl semimetals. The first type has pointed like Weyl points and straight Dirac cones, while the second kind has tilted Dirac cones, and the crossover is no longer point-like [36]. Obtaining a Weyl semimetal requires inversion symmetry or the time-reversal symmetry to be broken [37]. Due to the chiral anomaly of Weyl points, exotic properties such as nonlinear optical responses could be introduced. Especially for type-II Weyl semimetal, attractive properties like superconductivity and quantum oscillations can be produced by the unconventional Fermi surface structure [**liu2020quantum**].

$Co_3Sn_2S_2$

Topological properties such as anomalous Hall effect and anomalous Nernst effect are found in various Weyl semimetals such as $Co_3Sn_2S_2$, TaAs, etc [38, 39]. Among them, we take $Co_3Sn_2S_2$ as our study case. It is a time-reversal symmetry breaking, type-II Weyl semimetal.

$Co_3Sn_2S_2$ belongs to the R3m space group, and it has a rhombohedral-hexagonal structure. $Co_3Sn_2S_2$ has a layered structure on ab plane stacking along the c-axis. As the only magnetic element, Co lies along the ab plane and forms the kagome lattice. (Fig. (3.15))

From early studies, $Co_3Sn_2S_2$ was believed to be a ferromagnet(FM) with a curie temperature T_C= 175 K. The spins are collinear and aligned with the c axis [39, 40]. However, more profound studies were pushed out in recent years, and shreds of evidence show the magnetic structure below T_C is more complicated than that. Both neutron diffraction and muon-spin rotation researches (μMR) suggest there is more than one magnetic phase under Curie temperature [41, 42]. In ref. [42], it was pointed out that there is an in-plain 120 degree antiferromagnetic(AFM) order competing with the out-of-plane FM state between 90 K and 177 K. The AFM state is predicted to generate Weyl nodes in the Brillouin zone. Also, with the introduce of an external field, the Co aligns parallel with the c axis. The conduction and valence bands overlap on a circle in reciprocal space, which is called a nodal line [39, 43]. The topology of the electronic band enhanced the importance of figuring out the magnetic states inside $Co_3Sn_2S_2$ at different temperatures.

Another main interest is an unexplained transition at a lower temperature. More than one study has reported the discovery of T_A=125 K transition showing the magnetic susceptibility, transport measurements, and optical measurements [44, 45]. A debate has been going on in the past few years about the $Co_3Sn_2S_2$ magnetic spin structure below T_C. Research has found anomalies in performing electromagnetic transport experiments on $Co_3Sn_2S_2$. After $Co_3Sn_2S_2$ sample experiences a field cooling process, the zero-field warming measurements show a sharp jump around 125 K [44]. The latest studies focused on this transition. They performed magneto-optical Kerr-effect on $Co_3Sn_2S_2$. From their results, they claimed for a field-cooled sample, a single magnetic domain will split into multiple smaller domains at the temperature of 125 K. A variety of macroscopic physical properties show the exotic transition as a result of changes in the domain wall [46, 47].

In our work, we employed Resonant Ultrasound Spectroscopy (RUS) to detect the 125 K transition using sound velocity. Also, the elastic constants are inspected. (see Chapter 4)

Chapter 2

Experimental Techniques

In this chapter, experimental methods are explained both theoretically and experimentally in detail. A workflow of synthesizing and characterizing our samples will be shown.

2.0.1 Sample Growth

Flux method

Flux growth is a commonly used method to gain high-quality single crystals. The basic idea of flux growth is to put all the ingredients into a crucible and seal it into a quartz tube under a vacuum condition [48]. Then melt the ingredients in a molten solvent with a high temperature. After dwelling in a high temperature for a long time (around one day), the solution will be cooled down with a prolonged cooling rate, usually 3 degrees per hour. Single crystals will grow in this process. The centrifuge will be performed to filter away the rest of the solution while it's still above the melting temperature. There are many materials that can be used as the flux to accomplish the reaction. Which works the best depends on the single crystals. (See Fig. 2.1 for a flux growth photo)

In my samples there are three systems of single crystals: RMn_6Sn_6 (R=Y,Lu), RMn_6Ge_6 (R=Y,Lu) and Co3Sn2S2. They are all grown from the flux method, but the processes have some differences.

For RMn_6Sn_6 (R=Y,Lu) single crystals, we used the method reported in Ref[**zhang2005unusual**]. Sn was used as the flux material, and the atomic ratio is R:Mn:Sn=1:10:30. The ingredient mixture was heated up to 1000 °C and kept for 12 hours. The temperature was cooled by 50 °C and heated up again to 990 °C. This step is to reduce the seed number so that more large single crystals can be grown. The centrifuge temperature was 600 °C. Large and thick hexagonal-shaped single crystals are found in the crucibles.

For RMn_6Ge_6 (R=Y,Lu) single crystals, they also grown by flux method. With the ratio R:Mn:Ge:In=1:6:20:20 and the similar heating process with RMn_6Sn_6, hexagonal pieces are obtained.

For $Co_3Sn_2S_2$, we used the method in Ref[49]. Sn is used as the flux. The ratio is $Co : Sn : S = 8 : 6 : 86$. The dwell temperature is 1100 °C, and the centrifuge temperature is 700 °C. We can get larger and thicker single crystals compared to the In flux with the Sn flux.

Modified Bridgeman method

Another growth method we use to gain single crystals is the modified Bridgeman method. We used it on synthesizing $Co_3Sn_2S_2$ as described in [50]. First, we measure all ingredients' powder in stoichiometric ratio. After that, a mortar and pestle mix the ingredients well. A 3g pellet sample will be formed after applying the pellet press. The pellet will be sealed under a vacuum inside a quartz tube to protect it from oxidizing. The tube will be placed inside a furnace vertically. We do that because we need to create a temperature gradient in the vertical direction to mimic the Bridgeman method. The quartz was heated to 1050 °C and cooled down to 700 °C with a rate of 4 °C per hour [45]. After cooling, the sample pellet will become a rod with metallic color. That is, cluster a multiple grains single-crystal $Co_3Sn_2S_2$. After cleaving, the chunk will split into multiple pieces with a clean cleaving surface. Powder X-ray diffraction was tested to check the right phase. To ensure those are single-phase crystals, we performed Laue single crystal diffraction to confirm.

2.0.2 Sample orientation and polishing

For the hexagonal layered single crystals, there is a low symmetry along the c-axis. As a result, it is worth studying the physics properties along different crystal orientations. A Laue system is used to detect the crystal structure. After that, the single crystals can be cut and polished in a rectangular shape using diamond saws and polishing stages. Our samples are metallic, and the electric signals are small. As a result, polishing the samples to a reasonably thin thickness is essential.

2.0.3 Magnetization measurements

Samples magnetization was measured by the commercial model SQUID Magnetometer from Quantum Design. The temperature range is 2 to 400K, and the largest magnetic field it reaches is 7 Tesla.

2.0.4 Resistivity measurements

Two experimental instruments are used for resistivity measurement. One of them is the Physical properties measurement system (PPMS) from Quantum Design, and the other is a self-built closed-cycle cryostat (CCR). The commercial model PPMS provides a temperature range of 2 K to 400 K. The resistivity puck gives the connections from the sample leads to the bottom pins in the PPMS chamber. Four electric probes were contacted on the sample to avoid contact resistivity.

Closed Cycle Cryostat (CCR) building for resistivity

Our CCR was built based on a purchased 4K Sumitomo cold head. It consists of two parts, a cold head and a He gas compressor. After filling the compressor with high purity He gas, the compressor will press the He gas to the bottom of the cold head. The He gas will be condensed into a liquid. Because of the cooling power of liquid He, the cold finger on the cold head will be cooled downed to 4 K in the best performance.

However, a single commercial model cold head could not finish the resistivity measurement. More parts are required before the CCR is put into use. We designed a copper-made thermal radiation shield from the which was fabricated in the UTK machine shop to surround the sample. As a result, the sample's thermal radiation from the outside environment will be prevented. Besides the shield, a vacuum chamber is also necessary for the CCR. Our vacuum chamber was made of stainless steel. It is clamped outside of the radiation shield to create a vacuum condition. On the chamber, several connections are provided for electric connectors and vacuum hose connections. We need a vacuum for our experiments as follows 1. A vacuum is the best thermal insulator. It will reduce the heat flow to the fewest between the sample and the outside environment. 2. We are mainly detecting physics properties in low temperatures. The vacuum will prevent the water, nitrogen, and other gas from being liquefied and condensed from the air. Then condensed gas will be a big disturbance for the experiment accuracy.

A vacuum station pumps out the air inside the whole system and creates a vacuum condition for the experiment. We purchased the Hicube station from Pfeiffer company. It contains a turbopump which provides a high vacuum option for us. After finishing assembling the parts, we tested the vacuum. We turn the station on and let it work for half-hour to stabilize the pressure inside. After we confirm the vacuum is good, we can move on to the following electronic step.

A copper-made sample holder is attached to the cold finger. On the sample holder, there are 12 pins. We will use 4 of the pins to perform the four-probe resistivity measurement on samples. The other four pins will be used to make the electrical connection for the temperature sensor. We also need another two pins to provide a current for the heater to control the temperature. Three sets of 4-twisted copper wires are soldered to those pins. On the other end, if the wires are connected to glass-sealed connectors in the vacuum chamber. A 12-wire cable was made to connect the inner electron circuit to a breakout box. The circus is led to a current source meter, a nano-voltmeter, and a temperature controller from the breakout box. The source meter will provide a stable direct current to samples,

and the nano-voltmeter will pick up the voltage difference. By applying a Lakeshore 335 temperature controller, we are able to read the temperature near the sample with a silicon diode thermometer and control the sample temperature with a 50 Ohm resistance heater.

In order to make data collecting automatic, we use LabView programs to control the experiment process. The LabView program will be introduced in detail in the following LabView code session.

After assembling everything, our CCR can achieve a temperature range from 4 K to at least 400 K. Up to amperes level, current can be applied to the sample, and nanovolt level signal can be collected.

2.1 Electric, magnetic and thermal transport properties

2.1.1 Hall effect, anomalous Hall effect, and topological Hall effect

Hall effect is a fundamental also essential electrical-magnetic property that plays a vital role in material characterizations. The Hall effect was firstly discovered by Edwin Hall [51]. It was described as a charge carrier movement under a magnetic field due to the existence of the Lorentz force. In the past few decades, scientists have discovered that some materials can hold a very complex Hall effect caused by some intrinsic properties [33]. We study the Hall effect on our kagome metals and hope to relate their magnetic structure with their exotic transport properties.

Ordinary Hall effect and anomalous Hall effect

For the normal Hall effect, it was expected to be linearly increasing according to the magnetic field growth. A few decades later, a much larger Hall effect signal than the linear Hall effect was raised up to form ferromagnets and became an enigmatic problem for almost a century [52]. The understanding of AHE (anomalous Hall effect) became more clearly understood

after the concepts of the Berry phase were proposed [53]. Pugh and Lippert found that in most cases, the Hall effect can be considered as a simple summary of the ordinary Hall effect (OHE) from the Drude model and anomalous Hall effect (AHE), which is proven to be linearly related to the material's magnetization. AHE is considered as the Berry phase impacting the momentum space. It is an intrinsic property and is dominated by different coefficients depending on which regime the material belongs to [54]. Therefore, we can interpret the Hall resistivity as follows:

$$\rho_{xy} = R_0 H_z + R_s M_z \tag{2.1}$$

In here, H_z is the exterior magnetic field and the M_z is the magnetization. The Hall coefficient R_0 in the OHE term is related to the carrier density, while the R_z in the AHE term is material dependent.

Topological Hall effect

The understanding of the AHE has been taken one step further in recent years. With more profound research on the frustrated ferromagnetic systems with non-coplanar magnetic moments, the Berry phase also influenced real space. In the topologically non-trivial (chiral) spin texture, such as skyrmions, a new mechanism give to a non-vanishing Hall effect, the so-called topological Hall effect [55, 56]. Therefore the third term was added to the equation above.

$$\rho_{xy} = R_0 H_z + R_s M_z + \rho_T \tag{2.2}$$

Both Hall effect and magneto-resistance measurements are performed in PPMS. Because of the possibility of existing anisotropy in my samples, we prepare the sample as Hall bars with different orientations to control the current and magnetic field directions. There is a maximum of 8 Tesla applying to the samples.

For the magneto-resistance, other than adding a magnetic field, the sample setups are the same with resistivity measurement in the PPMS.

2.1.2 Thermal transport effects

One of the reasons that thermoelectricity is very promising in the application tier is that it allows people to use waste heat [57]. In our study, the Seebeck effect and Nernst effect are measured on our kagome metals. We hope to discover how the complex magnetic spin structure in kagome metals affects their thermal transport properties.

Seebeck effect

The Seebeck effect is a famous thermoelectric effect discovered by German scientist Thomas Johann Seebeck over one century ago [58]. It was described as an electrical potential difference building up while a conductive material experiences a heat flow(Fig 2.2(b)). We use the ratio between temperature and electric voltage difference as the Seebeck coefficient.

$$S = \Delta V / - \Delta T \tag{2.3}$$

The Seebeck effect was well applied in plenty of applications evolved with the temperature measurements. Thermocouples are good examples.

Nernst effect

Nernst effect is a thermoelectric effect that appears under thermal gradient and magnetic field interaction. It was first found by Walther Nernst and Albert von Ettingshausen [59]. They found if the heat flow is in a perpendicular direction to the magnetic field, in the third orthogonal direction, an electric field will build-up, and a voltage potential is accumulated. Experimentally the equation to calculate the Nernst coefficient is as follows:

$$S_N = \triangle V / - \triangle T \tag{2.4}$$

In a recent study on magnetic kagome metals, evidence showing anomalous Nernst effect (ANE) is obtaining attention. The Nernst effect is the counterpart of the Seebeck effect under the influence of the magnetic field [39]. Theoretically, when the Berry phase arises, an ideally maximized anomalous Hall effect appears. Hence as the thermal counterpart, the anomalous Nernst effect is expected to be detected around the Fermi energy [60]. As a result, ANE is direct evidence of Berry curvature.

Experimental setup for Nernst and Seebeck effect

Using the PPMS to provide a temperature and controllable magnetic environment, we implemented thermal transport properties on an empty PPMS puck. The puck was purchased from Quantum Design. Unlike a resistivity puck, the empty puck does not have insulator layers or exposed leads. We need to hand-make 12 exposed leads for samples and temperatures. Copper wires are used for leads. They are soldered to the puck bottom channels. The wires are then brought up to the puck top surface and fixed using captain tapes.

According to the common figure of the Nernst and Seebeck effect, we need two thermometers to measure the temperature difference on both the cold end and hot end. A heater is required to heat the hot end and create the temperature difference between the two ends. Two leads will be left for the Nernst voltage measurement on samples. Fig.2.2 is a photo of the setup on an empty puck. We cut a fiber class board to the same size as the puck top to use as the insulator layer on that puck. Then GE varnish was applied to stabilize the board. We dug a slot on the insulation layer and inserted copper pieces as a sample extension to place the heater and thermometers on the hot and cold sides. Because we want to test thermoelectric transport and transverse properties on both 0 field condition and magnetic field applied condition, Cernox thermometers are required. The Cernox thermometer's calibration curve is still good even with the field applied. Since our samples are small and it is impossible to place thermometers directly on the sample, we take benefit from copper's high thermal conductivity and place the thermometers on the copper

pieces. For the same reason, we fixed the chip heater with GE vanish. So the 12 pins for PPMS inner electricity circuit are divided into four groups. There are four pins for each thermometer, two pins for the chip heater, and two for sample measurement. Then we build a 12-channel cable to connect the PPMS inner electricity pattern to the meters (temperature controller, source meter, nanovolt meters).

With the same puck, we can perform both Seebeck and Nernst tests by changing the geometry of the electrodes. For the Nernst effect, the two electrodes for voltage should have as less longitudinal offset as possible. On the perpendicular to the heat gradient direction, the voltage is measured. We can calculate the Nernst coefficient by the voltage and temperature difference provided by those two thermometers. For Seebeck measurements, the experiment process is similar, except the voltage difference is measured along the direction of the thermal gradient.

There is no suitable program on PPMS that follows our customized designs. So LabView programs are used to automate the experiment controlling and data collecting. Details are given in the following LaView session.

2.1.3 Resonant Ultrasound Spectroscopy

Resonance Ultrasound spectroscopy (RUS) is a method to detect the material's phase transition using mechanical resonance. It has been used for a long time to find the structural and magnetic transitions and has proved to be extremely sensitive to thermodynamic anomalies [61–64]. Usually, a rich range of ultrasound spectroscopy is applied to the sample material. Meanwhile, the sound velocity is measured. The elastic constants of the sample can be derived from the velocity. Theoretically, elastic constants give a direction to the atomic bonding of the material. They are also the second derivatives of free energy with respect to strain [65]. As a result, detecting elastic constants provides scientists with an accurate way to determine the phase transitions happen inside the sample. There are multiple examples indicate that RUS is very reliable. The changing of magnetic spin structure states was found between paramagnetic to ferromagnetic or antiferromagnetic states using RUS [66]. RUS is

also able to detect short-range magnetic order, such as spin glass [66–68]. Because of the diversified magnetic spins, a very noticeable phenomenon is expected in the RUS results. In our study, we apply RUS to our kagome materials.

Our lab uses digital RUS equipment to send high-frequency mechanical vibrations up to 30 MHz. The vibration was send to the samples by the direct touch with transducers. The top transducer converts the electric signal into mechanical vibrations and interacts with the lattice vibration. Another transducer picks up the resonance signal on the sample bottom and transforms it into an electric signal. From the scanned spectroscopy, we can easily position the resonance. Resonance peaks shift with the changes in the sample's phase transitions. By tracking them, we have a clear idea of the existence of the transition and how it influences the sample's intrinsic frequencies. A continuous scan is performed on a small range of frequencies during the data collection. The temperature difference within each scan can be trivial with a prolonged temperature changing rate.

2.1.4 LabView programming

LabView is a graphical programming language we use to control the instruments for experiments. For resistivity on CCR and customized thermal transport and transverse measurement, we made three programs to implement them. In the following paragraphs, the logic of those three experiments will be presented.

Resistivity

Resistivity measure is straightforward, following Ohm's law. Theoretically, all we need to collect is the current(I) we applied to the sample and the voltage difference(V) caused by the current. By applying the following equation, resistance can find out by division.

$$R = V/I \tag{2.5}$$

However, in reality, it is more complicated. We can not ensure the temperatures on two voltage measurement leads. Due to the thermopower effect, an extra longitudinal thermal voltage will be collected as well. That extra component needs to be eliminated. We can use the symmetry of the signal to achieve that.

If we use V_R to represent the voltage difference caused by sample resistance, V_th to represent the thermal voltage, and V_total to represent the total voltage measured from the voltmeter, we will have:

$$V_{total} = V_R + V_t \tag{2.6}$$

Among that component, the V_R's direction is dependent on the current direction. This means we will get a positive V_R when the current is in a positive direction and a negative V_R when reversing the current. The measured V_total will also be positive. However, the temperature gradient between the two voltage leads does change. So for a negative current, we have:

$$-V_{total} = -V_R + V_t \tag{2.7}$$

We can get the pure V_R if we minus equation 2.6 by equation 2.7 and divide the result by two; we can get the pure V_R. From that, we can calculate the accurate resistivity.

The LabView code logic follows this order:

First, set starting and ending temperatures. Turn on the cooling process, and make the thermometer read the environment temperature continuously. The temperature controller will execute the heating process when the temperature reaches the starting point.

During the heating process, every measurement and data recording needs to be done briefly to decrease the temperature change as much as possible. The current source will output a current, and the voltmeter will pick up the data. Then, the current source meter will output another current with the same value and opposite direction. The voltmeter will

also pick up the second signal. After that, the program will do a quick calculation and record the resistance result and the real-time temperate.

Seebeck coefficient

For the Seebeck coefficient, we can directly calculate equation 2.3.

We are performing the measurement using LabView along with the PPMS Multiview system. So a connection is needed to ensure the communication between two systems. We downloaded the Multiview command package from the Quantum Design website. Using the elements inside the package, we can read the temperature and magnetic field inside the PPMS sample chamber.

The basic logic is collecting the Seebeck coefficient as a function of temperature. First, we must create a temperature gradient between the sample's hot and cold end. We use a temperature controller to output a constant current to the heater chip on the hot end copper plate to achieve that. After that, Multiview will set a starting temperature and ending temperature. We keep an eye on the chamber temperature. When it reaches the starting temperature, the measurement process will be activated. Two Cernox thermometers will collect the cold and hot end temperature simultaneously. The temperature difference will be calculated and divided by the voltage difference picked up by the voltmeter.

Nernst effect

When we measure the Nernst effect, we usually need to find out the Nernst coefficient as a function of the magnetic field. So similar to the Hall effect measurement, we need to sweep a continuously changing magnetic field on the sample.

Using the same LabView-Multiview package, we can design the measurement step by step at different temperatures. A couple of target temperatures are given, and the experiment temperature will be adjusted to the target temperature in the given order. A waiting time will be taken to stabilize the temperature at each temperature. After that, the temperature will heat the hot end, and a constant temperature difference will appear between the two ends.

After that, the LabView program will send the command to control the PPMS sweeping magnetic field with a customized field range and changing rate. In the meantime, the voltage difference perpendicular to the heating gradient is continuously collected. The field at each data taken point is also recorded simultaneously.

Chapter 3

RMn_6Sn_6 rare earth intermetallic compound

The Rare earth intermetallic compound RMn_6Sn_6 (R for rare earth elements) has a $MgFe_6Ge_6$-type structure and belongs to the space group P6/mmm. The Mn atoms distribute along the ab plane and form into a kagome lattice. [32, 35, 69].

3.1 YMn_6Sn_6

3.1.1 Motivation

The complicated magnetic structure attracts our attention to detect more potential than 166 materials may contain. As reported in previous literature, every 166 compounds experience multiple nontrivial magnetic states before the moments are saturated. From Nirmal's study, we know the YMn_6Sn_6's near-room-temperature THE is due to the Transverse conical spiral (TCS) spin motivated by a high magnetic field. The multiple transitions inside YMn_6Sn_6 suggest that a few phases are competing when different fields are induced. Besides the magnetic field, we want to see if there are other methods to tune the magnetic structure

inside YMn_6Sn_6. In order to answer this question, we designed an electric current applied neutron diffraction experiment.

3.1.2 Experiments and results

The work done by Wang et al. reported the existence of the topological Hall effect when the field is set along [100], and the current is along [001]. However, they didn't find the topological Hall effect in the H along [001] and current along [100].

Later, Ghimire et al. studied the magnetic spin structure in more detail. They claimed four nontrivial spin structures with the increasing magnetic field from analyzing the neutron data with a high magnetic field applied in the ab plane. They are Distorted spiral (DS), Transverse conical spiral (TCS), Fan-like (FL), and Forced-ferromagnetic (FF). THE is only found in the TCS state and reaches the highest amplitude in 245K. The TCS provides pairs of magnons with the same energy and opposite chirality from their theory. In this case, a chiral field rises, and the topological Hall resistivity is proportional.

Our experiment is interested in how magnetic structure would change with a current applied. We first grew the single crystals with the flux method described in chapter 2. We take measurements on temperature-dependent magnetization along both a and c directions. We found that the transition from antiferromagnetic to paramagnetic happens around 350 K in both crystal directions. (Fig. 3.1) It was the same as the previous reports.

After using the Laue to achieve the crystal alignment, we cut the crystal into a small parallelepiped shape with a cross-section of $0.5mm * 0.8mm$ (Fig.3.2). The a-axis is along the longest edge and the c-axis points outside the picture.

Low resistance wires are needed because a large current density is required in our experiments. We used thick copper to conduct the current to the sample. The unique craft was performed on both ends of the copper wires. They are first pressed into thin flat surfaces, and then the two edges are bent up and form a boat shape. The two ends of the sample can sit inside the boat and have a sizeable conducting surface with the copper wires. After that, the parallelepiped shape sample has the two ends tied by thin copper wires with

the copper boat ends. Indium solder is applied on both sides to make good electrically conductive joints. A neutron beam was applied along the c axis, and scans along (00L) were collected. (Fig.3.3)

Results without current applied are shown in Figure 3.4. diffraction peaks are collected at 300K. Two incommensurate peaks appear at 300K, which fit the reported double spiral structure. Temperature-dependent zero current diffraction was also collected, shown in Figure 3.5. When the temperature is lower than 350 K, those two incommensurate peaks dominate, which means the double spiral structure is the only structure. As the temperature goes up, a commensurate magnetic peak arises. It was because of the colinear antiferromagnetic order [33].

We estimated the heat produced by the sample when the different values of currents were applied. The heating power is very small and should not affect the measurement. We still decided to add pulse current to lower the risk of the sample getting burned.

Two groups of data were collected and shown in Fig. 3.5. At temperature 340 K, diffraction peaks are collected for 0 A and 20 A conditions. The 20 A current drives the change of spin configuration. One most prominent feature enhances the weaker satellite peak by adding current. There is an enhancement of the weak satellite peak at every incommensurate position.

3.1.3 Discussion and future plans

From the current added neutron diffraction experiment, we can conclude that (1) So far, the current does not cause experimental environment temperature changes. (2) Electric current is modifying the spin structure. With the promising conclusion we make, more YMn_6Sn_6 neutron diffraction measurement is well worth looking into. In the future study, we hope to answer the relationship between the adding current value and the Mn spin structure at different temperatures. Meanwhile, it is also worth testing diffraction peaks switch the sample orientation, which means applying current along the c-axis.

3.2 $ScMn_6Sn_6$

3.2.1 Motivation

In order to exame if the TCS that caused THE is a unique structure of YMn_6Sn_6, research on similar materials is essential. Previous studies have shown that $LuMn_6Sn_6$ and $ScMn_6Sn_6$ have plenty of similarities in their crystal and magnetic structures with YMn_6Sn_6 [35]. However, there were no transport studies on $ScMn_6Sn_6$ or $LuMn_6Sn_6$, which leaves us a question about whether these 166 compounds contain THE. To answer that question, we need to detect the physics properties of both $ScMn_6Sn_6$ or $LuMn_6Sn_6$ single crystals.

$ScMn_6Sn_6$ is an excellent material to start with. In [35], when the magnetic field is set along an a-axis, its field-dependent magnetization is reported to have a metamagnetic transition before saturation. With the same sample orientation, YMn_6Sn_6 also has that figure, and THE happens between the metamagnetic transition and saturation point. With the flux growth method, we grow single crystals large enough to detect transport properties in all orientations. The experimental method and result are introduced in the following context.

3.2.2 Sample preparation

Single crystals of $ScMn_6Sn_6$ were synthesized from excess Sn following a procedure similar to that described in [35]. Sc(Alfa Aser 9999%) and Mn(Alfa Aser 9999%) pieces were combined with Sn shot in the atomic ratio $Sc : Mn : Sn = 1 : 6 : 30$. The starting materials were placed in a Canfield crucible set and sealed in a silica tube under vacuum. The tube was heated at 50 °C per hour until it reached 973 °C and allowed to dwell for 48 hours. The tube was then cooled at a rate of 3 °C /hr to 923 °C and then reheated to 963 °C at 50 °C /hr. This step was to reduce nucleation sites and yield larger crystals. Lastly, the tube was cooled at a rate of 3 °C/hr to 600 °C, and the crystals were separated from the flux by centrifugation. The crystals grew as hexagonal cylinders, with the c-axis along the cylinder axis (see Fig. 3.7(d)). The crystals ranged from 3-7 mm in the largest dimension and grew as long cylinders

and plate-like cylinders. Powder X-ray diffraction (PXRD) was performed on single crushed crystals using a PANalytical Empyrean diffractometer in Bragg-Brentano geometry utilizing a PIXcel3D area detector with a Cu-K source. Crystallographic parameters were refined using GSAS II. Energy-dispersive X-ray spectroscopy was performed on several crystals to confirm that the crystals are chemically homogeneous. Elemental mappings for one of the samples can be found in the Supplemental Material. Laue diffraction was used to orient the single crystals. The edges of the 120° angles were along [100] as expected (see Fig. 3.7(d)). The crisp Laue patterns confirmed the crystals were high-quality single crystals with no sign of twins, apparent defects, or residual strain.

After orientation, the single crystals were cut and polished into thin rectangular plates. We prepared two types of crystal orientation. In Type I, the [100] axis was parallel to the long side of the rectangular plate (see Fig.3.7(e)). This allows the magnetic field to be applied perpendicular to the kagome planes. In Type 2, the [100] axis was parallel to the thin dimension of the plate (see Fig.3.7(e)), allowing the magnetic field to be applied parallel to the kagome planes. Magnetization measurements were performed using a Quantum Design Magnetic Property Measurement System. We changed the temperature from 2 K to 390 K with an applied magnetic field of 1000 Oe, along [100] and [001] directions. We obtained the magnetic susceptibility as a function of temperature. Magnetic isotherms were obtained by sweeping the magnetic field from -7 T to 7 T at several fixed temperatures.

Magneto-transport measurements were carried out using a Physical Property Measurement System(PPMS) from Quantum Design. The figure shows the configuration of electrical resistivity, magnetoresistance, and Hall effect measurements with the orientation of the kagome planes in the sample indicated by fine lines. Magnetoresistance was calculated as $100 * (R_H - R_o)/R_o$. For the Hall effect measurements, we acquired the data for each sample from -8 T to 8 T. The misalignment voltage was removed by subtracting the measured voltage at positive and negative fields and dividing by two. Single-crystal neutron diffraction experiments were performed on the HB-3A DEMAND diffractometer at the High Flux Isotope Reactor (HFIR) at Oak Ridge National Laboratory (ORNL). A crystal of $3*3*2cm^3$

was mounted on an aluminum pin. Measurements were performed between 15 and 410 K in a closed-cycle refrigerator with an incident neutron wavelength of 1.542 A. Refinements of the nuclear and magnetic structures were performed using the FullProf program[70].

3.2.3 Result

Crystal structure, magnetism, and resistivity

The single-crystal of the ScMn6Sn6 single-crystal belongs to the hexagonal MgFe6Ge6-type structure P6/mmm space group [30]. Our refined lattice parameters are a=5.464(0.00002)$\mathring{A}$; c=8:959(0:0002) $\mathring{A}$. The refinement is done using software GSASII. They are comparable with lattice parameters a= 5:48 $\mathring{A}$, c= 8:98 $\mathring{A}$, reported in [32]

Fig.3.8 shows the magnetic susceptibility and two crystal orientations changes with temperature. When H is along [100], chi shows a tremendous change in temperature. This anisotropy indicates that the easy axis is lying along the ab plane. It agrees with the previous literature.[34, 69] The previous neutron study describes the magnetic structure as helimagnetic when the temperature is below 200K.[69] In our data, a sharp peak appears around 380 K when the magnetic field is applied along both orientations. It is the Néel temperature. From our result, there is only one magnetic phase below Néel temperature. We performed neutron diffraction experiments to confirm that. The detailed results are shown later.

We define the dimensions [100], [110], and [001] as x, y, z-axes. Fig. 3.9 gives the two longitudinal resistivities along [100] and [001] (labeled as xx and zz). They both have metallic behavior. An anisotropy appears between the two resistivities. Field-dependent magnetization, Hall effect, and magnetoresistance are also measured and presented below.

Fig. 3.10(a) gives the results when the magnetic field is set along the x-axis. The magnetization vs. field data was recorded at constant temperatures. From the graph, we can see a sudden transition arises at around 1.5 T at all temperatures. With the temperature going lower, the critical field goes to higher regions. In the former report, it was considered the metamagnetic transition when the magnetic moments transform from

spirals to antiparallel [34]. The saturation field starts from 2 T at room temperature. When the temperature goes down, the saturation field enhances to a more significant value. At 70 K, it becomes larger than 5 T. For Hall resistivity, and we define xz as the current along the z-axis and field along the x-axis. The voltage difference was measured along the y-axis. Similarly to M vs. H, we found the same transition at all temperatures. However, The critical fields are slightly larger than M vs. T. By plotting the M vs.H, and the Hall effect together(Fig 3.12), we see the hysteresis in the Hall effect is very clear. Moreover, as the field increases, a significant bump appears in the Hall effect. The bump starts from 260 K. When the temperature cools down; the bump becomes more stands out. After that, the bump decreases. At 70 K, the bump vanishes. There is no sign showing the same bump on the M vs. H data. In other field regions, the Hall effect curve has a high similarity with magnetization at the same temperature condition. For the magneto-resistance(MR), the metamagnetic transitions appear on the same critical field as the Hall effect. MR also shows a slope change around the critical fields. In those fields, the bumps on the Hall effect reach their maximum values. When magnetic fields grow to a little bit higher than the saturation points, another slope change happens on the MR curves. After that, the MR curves are linear to the field.

Fig. 3.10(a) gives the results when the magnetic field is set along the x-axis. The magnetization vs. field data was recorded at constant temperatures. From the graph, we can see a sudden transition arises at around 1.5 T at all temperatures. With the temperature going lower, the critical field goes to higher regions. In the former report, it was considered the metamagnetic transition when the magnetic moments transform from spirals to antiparallel [34]. The saturation field starts from 2 T at room temperature. When the temperature goes down, the saturation field enhances to a more significant value. At 70 K, it becomes larger than 5 T. For Hall resistivity, and we define xz as the current along the z-axis and field along the x-axis. The voltage difference was measured along the y-axis. Similarly to M vs. H, we found the same transition at all temperatures. However, The critical fields are slightly larger than M vs. T. By plotting the M vs.H, and the Hall effect

together(Fig 3.12), we see the hysteresis in the Hall effect is very clear. Moreover, as the field increases, a significant bump appears in the Hall effect. The bump starts from 260 K. When the temperature cools down; the bump becomes more stands out. After that, the bump decreases. At 70 K, the bump vanishes. There is no sign showing the same bump on the M vs. H data. In other field regions, the Hall effect curve has a high similarity with magnetization at the same temperature condition. For the magneto-resistance(MR), the metamagnetic transitions appear on the same critical field as the Hall effect. MR also shows a slope change around the critical fields. In those fields, the bumps on the Hall effect reach their maximum values. When magnetic fields grow to a little bit higher than the saturation points, another slope change happens on the MR curves. After that, the MR curves are linear to the field.

The same measurements were performed on samples with different orientations (Fig. 3.11). This time sample's z-axis was aligned along the field. At all temperatures, magnetization and yx show linear growth as the field increases. In the Hall effect data, there is no clear evidence showing extra components(bumps). The MR curve first shows a curve with slop decreasing. After the saturation fields, MR becomes linear to the field growth.

3.2.4 Neutron Diffraction

Fig.3.13 summarizes our neutron diffraction results in zero fields. Below TN 390 K, magnetic reflections belonging to the propagation vector (0,0,L) are observed. At the base temperature of 15 K, the magnetic structure is refined to be a double-helical order with an ordered moment of 2.55(5) μ_B/Mn, which is consistent with the previous study on a powder sample [32]. The length of the propagation vector increases with temperature, reaching a value of = 0.31 at 380 K just below TN. In contrast to YMn_6Sn_6 where a collinear magnetic phase with = 0.5 is observed in a narrow temperature regime below T_N [33, 34], the incommensurate in $ScMn_6Sn_6$ indicates a noncollinear double-helical structure throughout the long-range ordered phase.

3.2.5 Discussion and conclusion

Following the previous literature, the Hall effect consists of 3 components. As shown in the following equation: $R_Hall = R_o * H + a * M + THE$. The first component is linear to the external field and is considered the normal Hall effect. The second component is proportional to the sample's magnetization and is the anomalous Hall effect(AHE). The third component is the topological Hall effect(THE). From observing our data, we can see that yz contains all three elements. The bump is a clear sign leading to THE. We compare the magnetization with the Hall effect in the same graph(Fig.3.12). We can see the difference between the two results starting from the spin-flop field. It grows larger with the field increasing. By comparing the THEhanging the non-magnetic rare earth elements might not change the topology of this

We can see many similarities by comparing our results with the previous study on YMn_6Sn_6. Their Neél points are above room temperature, and they are both good metals. Their magnetization, Hall measurement, and MR show spin reorientation at relatively small fields. YMn_6Sn_6 was proved to host a THE. The THE has a maximum value of 245 K [33]. We observed a THE in $ScMn_6Sn_6$ with the same sample symmetry, and the maximum value is at 220 K. In [33], researchers claimed THE inside YMn_6Sn_6 is a consequence of a special spin structure. The magnetic spins are described as tilted conical spirals(TCS). A chiral field forms as a result and leads to THE. By Studying the $ScMn_6Sn_6$ samples, we obtained THE with the same magnitude as what is reported for the YMn_6Sn_6 compound. This makes the ScMn6Sn6 sample a good candidate for novel spintronic just as YMn6Sn6. One advantage of $ScMn_6Sn_6$ over YMn_6Sn_6 is that the THE happens at much lower magnetic field which makes this compound more suitable for application. However, the magnetic structure causes the THE inside $ScMn_6Sn_6$ is still unrevealed. We arranged a field applied neutron diffraction measurement. We will have a microscopic view when we have the result. There is one thing worth noting. For YMn_6Sn_6, there is only a TCS phase between the helical and AFM phase at 245 K. The TCS phase is the only phase causing THE. However, $ScMn_6Sn_6$ might not be the same case. At 220 K, the M vs.H result contains a slope change around 3 T.

That suggests there might be more than one magnetic phase between helical and forced ferromagnetic structure. THE appears in Both phases. This phenomenon will distinguish $ScMn_6Sn_6$ from YMn_6Sn_6.

Another significant difference between YMn_6Sn_6 and $ScMn_6Sn_6$ is they have different zero field magnetic structure. Unlike YMn_6Sn_6, $ScMn_6Sn_6$ only has the double spiral structure when the temperature is below the Néel temperature. The colinear AFT state in the YMn_6Sn_6 is not presenting in $ScMn_6Sn_6$. However, the lack of colinear AFM does not eliminate the THE.

Our magneto-resistance data exhibits different behavior from YMn_6Sn_6 as well. In YMn_6Sn_6, zz holds a negative value in low temperatures. It turns positive when the temperature reduces to a lower region. In $ScMn_6Sn_6$, at all temperatures, MR obtains a minimal positive value when the magnetic field is within the helical magnetic phase. As the field grows, MR shows a drop around the spin-flop transition, then changes its value to negative. Around THE range, MR shows anomalies. At 220 K, it behaves as a slope change. At lower temperatures, the anomaly changes to a remarkable transition. From the consistency between MR and field-dependent magnetization, we can conclude that the magnetic configuration influences MR heavily.

3.3 $LuMn_6Sn_6$

3.3.1 Sample preparation

$LuMn_6Sn_6$ single crystals were grounded into fine powders to check the powder X-ray diffraction (PXRD).

We confirmed the good quality of the single crystal by obtaining a clear Laue pattern (see supplementary). Using the software Orientexpress, we find out the orientation of single crystals. Cutting and polishing let us get thin bar-shaped single crystals with surfaces perpendicular to [100] and [001] directions.

The magnetization measurements were performed using a Quantum Design Magnetic Property Measurement System. Single crystal's magnetic moments were measured from 2 K to 300 K in a 1000 Oe field, along with [100] and [001] directions. We also set several constant temperatures and swept the magnetic field from negative 7 Tesla to 7 Tesla to obtain the field-dependent magnetization data.

Electric and electromagnetic transport properties were performed using a Quantum Design Physics Properties Measurement system. We set the surface of the bar-shaped sample perpendicular to the magnetic field to ensure the field direction is along [001] or [100]. In this case, the four electric leads are put along [100] or [001] for resistivity measurements under field zero fields. Similarly, in the Hall effect measurement, the current was sent along [100] or [001], while the leads measuring the voltage difference were set along the [110] direction.

3.3.2 Crystal structure and magnetism

The $LuMn_6Sn_6$ single crystal belongs to hexagonal MgFe6Ge6-type structure P6/mmm space group [30, 35]. Fig. 3.13 is our refined result of powder X-ray diffraction result. Our refined parameters are $a = 5.50814$ $\mathring{A}$, $c = 8.98729$ $\mathring{A}$. As shown in Fig. 3.14(a), in the c direction, $LuMn_6Sn_6$ single crystals are formed by Mn-Sn-Sn-Sn-Mn slabs and Mn-(Lu-Sn)-Mn slabs overlapping each other as layers. Mn atoms distribute along the ab plane and form into kagome lattice (Fig. 3.14(b)) [30, 35].

With the coexisting of the two slabs, $LuMn_6Sn_6$ is an antiferromagnet with a Néel point around 400 K[35]. Fig. 3.15 shows how the magnetic susceptibility changes with temperature. It was measured along with both [001] and [100] directions under a 1000 Oe field. The temperature-dependent heat capacity and RUS were also measured, as shown in Fig. 3.17 Fig. 3.18.

3.3.3 Resistivity, magnetism, and Hall effect

Two kinds of the thin bar (thickness 0.1mm) shaped samples with different dimensions were prepared. One kind has surfaced as [001] plane, and the other has [100] plane. Here, we define the dimensions [100], [110], and [001] as x, y, and z.

Fig. 3.19 gives the two longitudinal resistivities along [001] and [100]. An anisotropy appears between two ρ, showing metallic behavior. The ρ along the z-axis has a larger magnitude than along the a-axis, and the ratio decreased by approximately 1 with the 370 K increase in temperature (Fig. 3.20).

Field-dependent magnetization, Hall effect, and magneto resistivity are also measured and presented below. Fig. 3.21 gave the results when the magnetic field was set along [001]. The magnetization vs. field was taken under constant temperatures. A transition appears when it is cooler than 250K. As the temperature decreases, a critical transition field stays around 3.5 Tesla. For Hall resistivity, we define ρzx as the current along z and field along x. We measured the voltage difference along y. Similar to M vs. H, the same transition arises below 250 K and enhances to above 3 Tesla at a lower temperature. For the magneto-resistance, sharp peaks appear as an agreement to the transitions that happen to magnetization and the Hall effect. There is no hysteresis loop observed in non of the measurements.

Same measurements were performed on samples with different orientations (Fig. 3.22). This time sample's z-axis was aligned along the field. At all temperatures, magnetization shows linear growth as the field increases. Like before, we define ρxz as the Hall resistivity when current is applied along the x-axis and field is along the z-axis, and the voltage along y is measured. No transition shows up either, suggesting only anomalous and normal Hall effects exist. The MR data is relatively small. Also, no hysteresis loop appears.

3.3.4 High field study

No evidence shows that the topological Hall effect exists in the low field region(8 T). We are curious if there are more magnetic phases when a higher magnetic field is applied. We tested the magnetization and transport properties on our $LuMn_6Sn_6$ with a 35 Tesla magnet.

Fig. 3.23 to 3.24 shows the magnetization measured in the High magnetic lab. Fig. 3.25 shows the Hall effect we measured. The magnetic field is set along the a-axis, and an electric current is applied on the c-axis. Similar to our previous small field measurement, the metamagnetic transition happens around 5 T. However, when the field is in a higher region, the Hall effect at all temperatures shows a bump before saturation point. These bumps are distinguished from the M vs. H curve. Following the calculation instruction in [33], we subtracted the normal Hall effect and anomalous Hall effect (Fig. 3.26). Magnetization data is from previous literature [35]. The rest part is pure topological Hall effect we detected in $LuMn_6Sn_6$. Similar to YMn_6Sn_6, the topological Hall effect behaves like a hump. While the temperature is cooling down, THE area grows larger. It indicates that the magnetic structure is causing THE increases in its region on the magnetic field. One thing worth noticing is that in 272 K, the metamagnetic transition vanished. However, THE is still rigid. The magnetic structure causing THE is robust through all temperatures.

Magnetoresistance is also measured with high magnetic applied (Fig. 3.27). The experiment applies the magnetic field along the crystal's a-axis, and an electric current is applied along the c-axis. The data agree with the Hall effect result. At 272 K, no sign of metamagnetic transition shows. At lower temperatures, the metamagnetic transition appears. The MR shows a dramatic decrease between the metamagnetic transition and the saturation field in all temperatures. They happen at the same magnetic fields as the THE. It suggests that these decreases should be caused by the same structure leading to the THE.

3.3.5 Discussion and conclusion

$LuMn_6Sn_6$ share the same crystal structure with YMn_6Sn_6, $ScMn_6Sn_6$. Their lattice parameters have small differences. $LuMn_6Sn_6$ has the magnetic structure more similar to

YMn_6Sn_6. With the absence of magnetic field and a lower temperature, the angle between Mn layers in Mn-Sn-Sn-Sn-Mn slabs is different from the angle between Mn layers in Mn-(R-Sn)-Mn (R = Y and Lu) slabs. When the temperature warms up, the double spiral structure turns to a colinear AFM order. Their transition temperatures have different value, but they are both below their individual Néel temperature. However, $ScMn_6Sn_6$ does not have the colinear AFM order.

For $LuMn_6Sn_6$, Large anisotropy also arises on the magnetization and transport result with the introduction of the magnetic field. When field is along an a-axis, both magnetization and Hall effect data show sizable transitions at relatively small field when temperature is below 250 K. Those transition are the matamagnetic transitions, same as YMn_6Sn_6 and $ScMn_6Sn_6$. The high similarity between magnetization and the Hall effect below those critical fields suggests the anomalous Hall effect is dominating. When magnetic field increases, $LuMn_6Sn_6$ Hall effect shows a large bump which is not present in magnetization. That bump is the THE inside $LuMn_6Sn_6$. $LuMn_6Sn_6$ has larger value THE than other two 166 materials. Also the THE in $LuMn_6Sn_6$ is very rigid at high temperatures.

In the future study,we need to detect magnetic applied neutron diffraction to know the spin structure for sure. By comparing the refined magnetic structures in YMn_6Sn_6, $LuMn_6Sn_6$ and $ScMn_6Sn_6$, a better understanding about the magnetic chiral structures and the THE they caused.

Chapter 4

Weyl Semimetal $Co_3Sn_2S_2$

4.1 Motivation

Since $Co_3Sn_2S_2$ was proved to be a type-II Weyl semimetal, scientists have performed a large number of experiments to determine the different magnetic phases in $Co_3Sn_2S_2$. Now the clear pattern is, $Co_3Sn_2S_2$ has a paramagnetic to ferromagnetic transition at 175 K. As the temperature decreases, the magnetic structure becomes completed. More than one phase arises, and an anomalous transition appears. A mysterious transition at 125 K has attracted attention. The transition shows in small field magnetization and the Hall effect. However, the thermal conductivity and resistivity show no anomaly around 125 K. Several explanations about this transition are carried out. Competing AFT state, domain size change, and spin glass structure are the leading opinions on causing the transition.[46] We wonder if this 125 K transition can be detected by the Ultrasound resonance and how magnetic domains would affect the sample's elastic modulus. We grew single crystals with both flux and Bridgman method and performed Ultrasound Resonance Spectroscopy (RUS) on them. Experimental details and results are provided in the following context.

4.2 Sample preparation and basic characterizations

$Co_3Sn_2S_2$ is also a magnetic kagome metal. It belongs to R3m space group and it has the rhombohedral-hexagonal structure []. $Co_3Sn_2S_2$ is a layered structure material and Co is the only magnetic ion. Co distributed along the ab plane and form kagome nets. (Fig. 4.1)

We want to confirm our sample's good quality, so we did magnetic measurements on our $Co_3Sn_2S_2$ single crystals. Fig(4.2) gives us the magnetic susceptibility as a function of temperature. Anisotropy appears when field along the a and c-axis. Both axes show the transition at Neél temperature 175 K. It matches with former studies.[] Beside T_N, we also found another transition T_c around 125 K. It shows a wavy curvature on both of the susceptibility.

We also tested the magnetization as a function of the magnetic field (Fig.4.3). Like previous literature [71], the magnetization saturates at a microscopic field and holds a hysteresis loop when the temperature is below T_N. The area of hysteresis becomes larger when the temperature decrease. From our Hall effect measurement, we found a high similarity to magnetization (Fig. 4.4). It indicates the anomalous Hall effect (AHE) is dominating [71].

Besides the AHE, ANE is also a nontrivial property found in $Co_{23}Sn_2S_2$.[] We performed thermo-electric experiments on our $Co_3Sn_2S_2$ with our own designed equipment. The experimental setup was described in the experimental method part in Chapter 3. Our result shows in picture 4.5. The non-linear pattern shows our sample contains an anomalous Nernst effect. Our Nernst effect data consists of two components. One component is linear to a magnetic field, and the other is proportional to the $Co_3Sn_2S_2$ magnetization. From previous literature, we know the ANE is a direct way to test the Berry curvature. We claim that the Berry curvature causes a strong effect in our sample.

Ultrasound Resonant Spectroscopy study

From our magnetization vs temperature data, we know there is a magnetization transition T_c locates around 125 K. Electric transport properties are also measured to detect the T_c.

(Fig.4.2) Our result shows the temperature-dependent resistivity we measured on our sample. At $T_N = 175$ K, the transition shows a behavior as a slope change. However, there is no clear evidence showing the T_c transition around 125 K from the R vs. T curve (Fig. 4.6).

In order to answer the question if the 125 K transition exists, we decided to perform Ultrasound spectroscopy on our sample and test its resonances reacting with temperature changing.

We made a small frequency range resonance scan for the experimental setup, which provided a short scan time. We continuously scan the same frequency range and cool down the experimental temperature with a prolonged cooling rate. By doing those, the temperature change within one scan is trivial.

We tested thousands of scans for one temperature cooling procedure. We tested the procedure with different magnetic fields added to the sample. As shown in Fig 4.7 to Fig 4.11, we chose the frequency between 1.38 MHz to 1.44 MHz. In this frequency region, there are three resonances. With the temperature decreasing, they all move to a higher frequency. When there is no magnetic field, the ferromagnetic transition show as a turning point around 175 K. We can not see clear evidence of the 125 K transition. However, when we increase the field to 200 Oe, a step-like transition appears around $T_c = 125$ K. When the field increases to 400 Oe, the 125 K transition becomes more standout. However, when the magnetic field increases to higher than 600 Oe, the 125 K transition seems to be suppressed with the increasing magnetic field(Fig.4.10, Fig.4.11).

Elastic modulus studies

The elastic constants of Co3Sn2S2 were determined by inverting the ultrasound spectrum following the procedure established by Leisure and Willis [72]. In this fitting procedure, the elastic constants were adjusted iteratively until the difference between the measured and calculated spectra were minimized. To our best knowledge, the constants for $Co_3Sn_2S_2$ have not been measured experimentally but rather they have been estimated based on density functional theory calculations [73] (see Table 4.1), which are estimated to be within 15% of

experimental values. Thus, we used these theoretical constants as starting values. In our initial fits, we observed that c_{33} and c_{23} were anticorrelated to within a factor of about two (see Fig. 4.12), meaning these constants cannot be fit independently. Therefore, we fixed the c_{33} to its theoretical value, allowed c_{23} to fit initially, and then fixed them both for all proceeding fits. The dimensions were allowed to be fit at room temperature and did not change significantly, which confirms a good fit to the shape. The dimensions were fixed to the RT fitted values for all other temperatures.

A total of 41 out of the first 45 modes were used to fit the elastic constants wherein we excluded modes that became buried in noise at some temperatures. The goodness of fit is assessed by the root-mean-squared (rms) error between the frequencies of the measured and calculated modes, which was nominally 0.6-0.7%. The relatively high error may be attributed to slightly imperfect shape as confirmed by systematically varying the dimensions and mass, calculating the ultrasound spectrum at constant density, and comparing to the measured spectrum. Despite this relatively high experimental uncertainty, the frequencies of the resonant modes, including the gaps between modes, aligned well with the model, as shown in Figure 4.13. Furthermore, we find the room-temperature bulk modulus K, shear modulus G, and Poisson's ratio of 91.7 GPa, 55.8 GPa, and 0.247 respectively, agree with the corresponding theoretical values of 97 GPa, 56.5(5) GPa, and 0.26 within the estimated uncertainty of 15% [73]. At each temperature, the data were fit three times by assuming different starting values ($\pm 2\%$ of initial) for the elastic constants, and the error bars were estimated from the variation in the results for the same rms error.

Because the elastic constants scale with the square of the resonant frequencies, the position of a frequency serves as sensitive, model-free method of tracking the temperature dependence of the elastic moduli. For example, the position and ultrasound attenuation factor Q^{-1} of a few n modes are plotted in Figure 4.14. The attenuation factor is a measure of internal friction in the sample [74]. The abrupt decrease in temperature dependence of the frequencies around 170 K along with a local maximum in Q^{-1} are clearly observed and attributed to the Curie transition at $T_c = 175$ K through magnetoelastic coupling. The data

also suggest two additional transitions, a small one near 130 K and a broad one around 250 K, both of which are characterized by the change in temperature dependence of the peak shift combined with a rise in Q^{-1}.

Fitting the elastic constants below room temperature proceeded by fixing the dimensions and propagating the room-temperature solution using the same modes with their new frequencies. The rms error remained stable around 0.60-0.70% throughout the experiment. The temperature dependence of the elastic constants is shown in Fig. 4.15(a). Clearly, the Neél transition is coupled with compressional moduli, e.g., c_{11}, identified by the drop at 171 K. Similarly, the sound velocity in Figure 3b shows a change in slope at the same temperature. The observed peak shift and attenuation increase around 250 K is connected to fluctuations in the c_{14} constant.

4.3 Conclusion

We used RUS to detect its magnetic transitions in the $Co_3Sn_2S_2$ study. After tracking the ultrasound resonances with temperature decreasing, both Curie point and 125 K transition were found. The Curie point is rigid with the change of magnetic field. The 125 K transition shows up in a small field and fades out when the field increases. The fitting of elastic moduli delivers the idea that those two transitions are related to different moduli.

More experiments on the magnetic field added elastic moduli fitting are expected in future studies. A better explanation of how elastic moduli affect the 125 K transition will be revealed.

Chapter 5

Summary

A variety of kagome metals are successfully synthesized in single crystal form. Rare earth 166 compound RMn_6Sn_6 and Weyl semi-metal $Co_3Sn_2S_2$. Transport properties were measured, and anomalous behaviors were discovered due to the exotic magnetic structure. Our study investigated materials with R = Y, Sc, and Lu. Single crystals are grown from the flux method. After surface cleaning and polishing, magnetization, neutron diffraction, and transport-transverse properties were tested on every material. All three materials show excellent electric conductivity. AFM was found to be the ground state of those three materials. A metamagnetic transition was found in a relatively small field in all three materials. After YMn_6Sn_6 was discovered to hold a near room temperature THE, $ScMn_6Sn_6$ and $LuMn_6Sn_6$ were investigated with the same method. $ScMn_6Sn_6$ and $LuMn_6Sn_6$ also present large THE with different critical magnetic fields. The general exiting THE might indicates those three materials have the same particular spin structure. To prove that, field-induced neutron diffraction should be performed. The differences in critical fields and temperatures might result from different sizes of rare-earth Lu, Y, Sc, and different lattice parameters.

$Co_3Sn_2S_2$ is proved to be a type two Weyl semi-metal whose band structure contains Berry curvature. The Berry curvature functions as magnetic monopoles and causes exotic transport properties. AHE and ANE were both found in $Co_3Sn_2S_2$. Using RUS, we studied a magnetic

state still under debate. The transition show up when we track resonance frequencies with changing temperatures. Elastic constants were also calculated in our study. By tracking all the elastic constants changing with temperature, there is a clear dependence between different transitions and elastic constants.

Kagome metals are a hot topic and are researched heavily by scientists worldwide. There is still much potential for these materials. Over 100 types of materials are in the same group of 166 materials, and they are not well detected yet. Except for the experiments in this paper, there are plenty of measurements worth looking into, such as ARPES(Angular resolved) and current-induced magnetic structure detection. In conclusion, kagome metals will provide a scientific playground waiting for scientists to explore.

Bibliography

[1]A. Burkov, "Topological semimetals", Nature materials **15**, 1145–1148 (2016).

[2]M. A. de Vries, J. R. Stewart, P. Deen, J. Piatek, G. Nilsen, H. Rønnow, and A. Harrison, "Scale-free antiferromagnetic fluctuations in the s= 1/2 kagome antiferromagnet herbertsmithite", Physical review letters **103**, 237201 (2009).

[3]J. E. Moore, "The birth of topological insulators", Nature **464**, 194–198 (2010).

[4]M. Neupane, S.-Y. Xu, R. Sankar, N. Alidoust, G. Bian, C. Liu, I. Belopolski, T.-R. Chang, H.-T. Jeng, H. Lin, et al., "Observation of a three-dimensional topological dirac semimetal phase in high-mobility cd3as2", Nature communications **5**, 1–8 (2014).

[5]V. S. Pribiag, A. J. Beukman, F. Qu, M. C. Cassidy, C. Charpentier, W. Wegscheider, and L. P. Kouwenhoven, "Edge-mode superconductivity in a two-dimensional topological insulator", Nature nanotechnology **10**, 593–597 (2015).

[6]Y. Zhang, K. He, C.-Z. Chang, C.-L. Song, L.-L. Wang, X. Chen, J.-F. Jia, Z. Fang, X. Dai, W.-Y. Shan, et al., "Crossover of the three-dimensional topological insulator bi2se3 to the two-dimensional limit", Nature Physics **6**, 584–588 (2010).

[7]J. Li, C. He, L. Meng, H. Xiao, C. Tang, X. Wei, J. Kim, N. Kioussis, G. Malcolm Stocks, and J. Zhong, "Two-dimensional topological insulators with tunable band gaps: single-layer hgte and hgse", Scientific Reports **5**, 1–9 (2015).

[8]X. Liu, D. Smith, J. Fan, Y.-H. Zhang, H. Cao, Y. P. Chen, J. Leiner, B. J. Kirby, M. Dobrowolska, and J. K. Furdyna, "Structural properties of bi2te3 and bi2se3 topological

insulators grown by molecular beam epitaxy on gaas (001) substrates", Applied Physics Letters **99**, 171903 (2011).

[9]M. Durnev and S. Tarasenko, "Magnetic field effects on edge and bulk states in topological insulators based on hgte/cdhgte quantum wells with strong natural interface inversion asymmetry", Physical Review B **93**, 075434 (2016).

[10]R. Tarasenko, M. Vališka, M. Vondráček, K. Horáková, V. Tkáč, K. Carva, P. Baláž, V. Hol, G. Springholz, V. Sechovsk, et al., "Magnetic and structural properties of mn-doped bi2se3 topological insulators", Physica B: Condensed Matter **481**, 262–267 (2016).

[11]L. J. Maczewsky, B. Höckendorf, M. Kremer, T. Biesenthal, M. Heinrich, A. Alvermann, H. Fehske, and A. Szameit, "Fermionic time-reversal symmetry in a photonic topological insulator", Nature Materials **19**, 855–860 (2020).

[12]P. S. Mandal, G. Springholz, V. V. Volobuev, O. Caha, A. Varykhalov, E. Golias, G. Bauer, O. Rader, and J. Sánchez-Barriga, "Topological quantum phase transition from mirror to time reversal symmetry protected topological insulator", Nature communications **8**, 1–7 (2017).

[13]R. Okugawa and S. Murakami, "Dispersion of fermi arcs in weyl semimetals and their evolutions to dirac cones", Physical Review B **89**, 235315 (2014).

[14]B. Singh, A. Sharma, H. Lin, M. Hasan, R. Prasad, and A. Bansil, "Topological electronic structure and weyl semimetal in the tlbise 2 class of semiconductors", Physical Review B **86**, 115208 (2012).

[15]Y. Su, X. Wang, and X. Wang, "Magnonic weyl semimetal and chiral anomaly in pyrochlore ferromagnets", Physical Review B **95**, 224403 (2017).

[16]Y. Su and X. Wang, "Chiral anomaly of weyl magnons in stacked honeycomb ferromagnets", Physical Review B **96**, 104437 (2017).

[17]T. Miyasato, N. Abe, T. Fujii, A. Asamitsu, S. Onoda, Y. Onose, N. Nagaosa, and Y. Tokura, "Crossover behavior of the anomalous hall effect and anomalous nernst effect in itinerant ferromagnets", Physical review letters **99**, 086602 (2007).

[18]H. Zhang, C. Xu, and X. Ke, "Topological nernst effect, anomalous nernst effect, and anomalous thermal hall effect in the dirac semimetal fe 3 sn 2", Physical Review B **103**, L201101 (2021).

[19]H. Yang, W. You, J. Wang, J. Huang, C. Xi, X. Xu, C. Cao, M. Tian, Z.-A. Xu, J. Dai, et al., "Giant anomalous nernst effect in the magnetic weyl semimetal co 3 sn 2 s 2", Physical Review Materials **4**, 024202 (2020).

[20]M. J. Gilbert, "Topological electronics", Communications Physics **4**, 1–12 (2021).

[21]F. Tang, H. C. Po, A. Vishwanath, and X. Wan, "Comprehensive search for topological materials using symmetry indicators", Nature **566**, 486–489 (2019).

[22]G. Scappucci, P. Taylor, J. Williams, T. Ginley, and S. Law, "Crystalline materials for quantum computing: semiconductor heterostructures and topological insulators exemplars", MRS Bulletin **46**, 596–606 (2021).

[23]H. P. Paudel and M. N. Leuenberger, "Three-dimensional topological insulator quantum dot for optically controlled quantum memory and quantum computing", Physical Review B **88**, 085316 (2013).

[24]I. Syôzi, "Statistics of kagomé lattice", Progress of Theoretical Physics **6**, 306–308 (1951).

[25]D. E. Freedman, T. H. Han, A. Prodi, P. Muller, Q.-Z. Huang, Y.-S. Chen, S. M. Webb, Y. S. Lee, T. M. McQueen, and D. G. Nocera, "Site specific x-ray anomalous dispersion of the geometrically frustrated kagomé magnet, herbertsmithite, zncu3 (oh) 6cl2", Journal of the American Chemical Society **132**, 16185–16190 (2010).

[26]M. Kang, L. Ye, S. Fang, J.-S. You, A. Levitan, M. Han, J. I. Facio, C. Jozwiak, A. Bostwick, E. Rotenberg, et al., "Dirac fermions and flat bands in the ideal kagome metal FeSn", Nature Materials **19**, 163–169 (2020).

[27]N. J. Ghimire and I. I. Mazin, "Topology and correlations on the kagome lattice", Nature Materials **19**, 137–138 (2020).

[28]M. Kang, S. Fang, L. Ye, H. C. Po, J. Denlinger, C. Jozwiak, A. Bostwick, E. Rotenberg, E. Kaxiras, J. G. Checkelsky, et al., "Topological flat bands in frustrated kagome lattice CoSn", arXiv preprint arXiv:2002.01452 (2020).

[29]Y. Xu, J. Zhao, C. Yi, Q. Wang, Q. Yin, Y. Wang, X. Hu, L. Wang, E. Liu, G. Xu, et al., "Electronic correlations and flattened band in magnetic weyl semimetal $Co_3Sn_2S_2$", arXiv preprint arXiv:1908.04561 (2019).

[30]Q. Wang, Q. Yin, S. Fujitsu, H. Hosono, and H. Lei, "Near-room-temperature giant topological hall effect in antiferromagnetic kagome metal YMn_6Sn_6", arXiv preprint arXiv:1906.07986 (2019).

[31]T. Kurumaji, T. Nakajima, M. Hirschberger, A. Kikkawa, Y. Yamasaki, H. Sagayama, H. Nakao, Y. Taguchi, T.-h. Arima, and Y. Tokura, "Skyrmion lattice with a giant topological hall effect in a frustrated triangular-lattice magnet", Science **365**, 914–918 (2019).

[32]G. Venturini, D. Fruchart, and B. Malaman, "Incommensurate magnetic structures of RMn_6Sn_6 (r= sc, y, lu) compounds from neutron diffraction study", Journal of alloys and compounds **236**, 102–110 (1996).

[33]N. J. Ghimire, R. L. Dally, L. Poudel, D. Jones, D. Michel, N. T. Magar, M. Bleuel, M. A. McGuire, J. Jiang, J. Mitchell, et al., "Competing magnetic phases and fluctuation-driven scalar spin chirality in the kagome metal ymn6sn6", Science Advances **6**, eabe2680 (2020).

[34]Q. Wang, K. J. Neubauer, C. Duan, Q. Yin, S. Fujitsu, H. Hosono, F. Ye, R. Zhang, S. Chi, K. Krycka, et al., "Field-induced topological hall effect and double-fan spin structure with a c-axis component in the metallic kagome antiferromagnetic compound y mn 6 sn 6", Physical Review B **103**, 014416 (2021).

[35]A. Matsuo, K. Suga, K. Kindo, L. Zhang, E. Brück, K. Buschow, F. De Boer, C. Lefèvre, and G. Venturini, "Study of the mn–mn exchange interactions in single crystals of RMn_6Sn_6 compounds with r= sc, y and lu", Journal of alloys and compounds **408**, 110–113 (2006).

[36]H. Zheng and M. Zahid Hasan, "Quasiparticle interference on type-i and type-ii weyl semimetal surfaces: a review", Advances in Physics: X **3**, 1466661 (2018).

[37]A. Zyuzin, S. Wu, and A. Burkov, "Weyl semimetal with broken time reversal and inversion symmetries", Physical Review B **85**, 165110 (2012).

[38]B. Lv, H. Weng, B. Fu, X. P. Wang, H. Miao, J. Ma, P. Richard, X. Huang, L. Zhao, G. Chen, et al., "Experimental discovery of weyl semimetal taas", Physical Review X **5**, 031013 (2015).

[39]S. N. Guin, P. Vir, Y. Zhang, N. Kumar, S. J. Watzman, C. Fu, E. Liu, K. Manna, W. Schnelle, J. Gooth, et al., "Zero-field nernst effect in a ferromagnetic kagome-lattice weyl-semimetal $Co_3Sn_2S_2$", Advanced Materials **31**, 1806622 (2019).

[40]P. Vaqueiro and G. G. Sobany, "A powder neutron diffraction study of the metallic ferromagnet co3sn2s2", Solid state sciences **11**, 513–518 (2009).

[41]Q. Zhang, S. Okamoto, G. D. Samolyuk, M. B. Stone, A. I. Kolesnikov, R. Xue, J. Yan, M. A. McGuire, D. Mandrus, and D. A. Tennant, "Unusual exchange couplings and intermediate temperature weyl state in co 3 sn 2 s 2", Physical Review Letters **127**, 117201 (2021).

[42]Z. Guguchia, J. Verezhak, D. Gawryluk, S. Tsirkin, J.-X. Yin, I. Belopolski, H. Zhou, G. Simutis, S.-S. Zhang, T. Cochran, et al., "Tunable berry curvature through magnetic phase competition in a topological kagome magnet", arXiv preprint arXiv:1904.09353 (2019).

[43]D. Liu, E. Liu, Q. Xu, J. Shen, Y. Li, D. Pei, A. Liang, P. Dudin, T. Kim, C. Cacho, et al., "Direct observation of the spin–orbit coupling effect in magnetic weyl semimetal co3sn2s2", npj Quantum Materials **7**, 1–5 (2022).

[44]E. Lachman, R. A. Murphy, N. Maksimovic, R. Kealhofer, S. Haley, R. D. McDonald, J. R. Long, and J. G. Analytis, "Exchange biased anomalous hall effect driven by frustration in a magnetic kagome lattice", Nature communications **11**, 1–8 (2020).

[45]Y. Okamura, S. Minami, Y. Kato, Y. Fujishiro, Y. Kaneko, J. Ikeda, J. Muramoto, R. Kaneko, K. Ueda, V. Kocsis, et al., "Giant magneto-optical responses in magnetic weyl semimetal co3sn2s2", Nature communications **11**, 1–8 (2020).

[46]S. Howlader, R. Ramachandran, Y. Singh, G. Sheet, et al., "Domain structure evolution in the ferromagnetic kagome-lattice weyl semimetal co3sn2s2", Journal of Physics: Condensed Matter **33**, 075801 (2020).

[47]K. Fujiwara, J. Ikeda, J. Shiogai, T. Seki, K. Takanashi, and A. Tsukazaki, "Ferromagnetic co3sn2s2 thin films fabricated by co-sputtering", Japanese Journal of Applied Physics **58**, 050912 (2019).

[48]P. C. Canfield, T. Kong, U. S. Kaluarachchi, and N. H. Jo, "Use of frit-disc crucibles for routine and exploratory solution growth of single crystalline samples", Philosophical magazine **96**, 84–92 (2016).

[49]M. A. Kassem, Y. Tabata, T. Waki, and H. Nakamura, "Single crystal growth and characterization of kagomé-lattice shandites $Co_3Sn_2-xInxS_2$", Journal of Crystal Growth **426**, 208–213 (2015).

[50]M. Tanaka, Y. Fujishiro, M. Mogi, Y. Kaneko, T. Yokosawa, N. Kanazawa, S. Minami, T. Koretsune, R. Arita, S. Tarucha, et al., "Topological kagome magnet co3sn2s2 thin flakes with high electron mobility and large anomalous hall effect", Nano Letters **20**, 7476–7481 (2020).

[51]E. Hall, "On a new action of magnetic on electric currents", Am. J. Math **2**.

[52]S. Nair, S. Wirth, S. Friedemann, F. Steglich, Q. Si, and A. Schofield, "Hall effect in heavy fermion metals", Advances in Physics **61**, 583–664 (2012).

[53]N. Nagaosa, J. Sinova, S. Onoda, A. H. MacDonald, and N. P. Ong, "Anomalous hall effect", Reviews of modern physics **82**, 1539 (2010).

[54]E. Pugh and T. Lippert, "Hall emf and intensity of magnetization", Physical Review **42**, 709 (1932).

[55]Y. Taguchi and Y. Tokura, "Enhancement of anomalous hall effect in a filling-changed pyrochlore-type molybdate", EPL (Europhysics Letters) **54**, 401 (2001).

[56]P. Bruno, V. Dugaev, and M. Taillefumier, "Topological hall effect and berry phase in magnetic nanostructures", Physical review letters **93**, 096806 (2004).

[57]B. I. Ismail and W. H. Ahmed, "Thermoelectric power generation using waste-heat energy as an alternative green technology", Recent Patents on Electrical & Electronic Engineering (Formerly Recent Patents on Electrical Engineering) **2**, 27–39 (2009).

[58]E. Velmre, "Thomas johann seebeck (1770-1831).", Estonian Journal of Engineering **13** (2007).

[59]K. Behnia and H. Aubin, "Nernst effect in metals and superconductors: a review of concepts and experiments", Reports on Progress in Physics **79**, 046502 (2016).

[60]T. Tomita, M. Ikhlas, and S. Nakatsuji, "Large nernst effect and thermodynamics properties in weyl antiferromagnet", in Proceedings of the international conference on strongly correlated electron systems (sces2019) (2020), p. 011009.

[61]R. Schwarz and J. Vuorinen, "Resonant ultrasound spectroscopy: applications, current status and limitations", Journal of Alloys and Compounds **310**, 243–250 (2000).

[62]F. F. Balakirev, S. M. Ennaceur, R. J. Migliori, B. Maiorov, and A. Migliori, "Resonant ultrasound spectroscopy: the essential toolbox", Review of Scientific Instruments **90**, 121401 (2019).

[63]G. Li and J. Gladden, "High temperature resonant ultrasound spectroscopy: a review", International Journal of Spectroscopy **2010** (2010).

[64]Y. Luan, "Elastic properties of complex transition metal oxides studied by resonant ultrasound spectroscopy", (2011).

[65]R. Maranganti and P. Sharma, "A novel atomistic approach to determine strain-gradient elasticity constants: tabulation and comparison for various metals, semiconductors, silica, polymers and the (ir) relevance for nanotechnologies", Journal of the Mechanics and Physics of Solids **55**, 1823–1852 (2007).

[66]P. Mukhopadhyay and A. Raychaudhuri, "Elastic properties of reentrant spin glass", Journal of applied physics **67**, 5235–5237 (1990).

[67]K. Fischer, "Ultrasound in spin glasses ii", Zeitschrift für Physik B Condensed Matter **50**, 107–111 (1983).

[68]C. Müller, V. Zestrea, V. Tsurkan, S. Horn, R. Tidecks, and A. Wixforth, "Spin-lattice coupling in the ferrimagnetic semiconductor fe cr 2 s 4 probed by surface acoustic waves", Journal of applied physics **99**, 023906 (2006).

[69]G. Venturini, R. Welter, B. Malaman, and E. Ressouche, "Magnetic structure of YMn_6Ge_6 and room temperature magnetic structure of $LuMn_6Sn_6$ obtained from neutron diffraction study", Journal of alloys and compounds **200**, 51–57 (1993).

[70]J. Rodrıguez-Carvajal, "Recent advances in magnetic structure determination by neutron powder diffraction", Physica B: Condensed Matter **192**, 55–69 (1993).

[71]Q. Wang, Y. Xu, R. Lou, Z. Liu, M. Li, Y. Huang, D. Shen, H. Weng, S. Wang, and H. Lei, "Large intrinsic anomalous hall effect in half-metallic ferromagnet co3sn2s2 with magnetic weyl fermions", Nature communications **9**, 1–8 (2018).

[72]R. G. Leisure and F. Willis, "Resonant ultrasound spectroscopy", Journal of Physics: Condensed Matter **9**, 6001 (1997).

[73]M. De Jong, W. Chen, T. Angsten, A. Jain, R. Notestine, A. Gamst, M. Sluiter, C. Krishna Ande, S. Van Der Zwaag, J. J. Plata, et al., "Charting the complete elastic properties of inorganic crystalline compounds", Scientific data **2**, 1–13 (2015).

[74]A. Migliori and J. Sarrao, *Resonant ultrasound spectroscopy: applications to physics, materials measurements, and nondestructive evaluation. 1997.*

[75]A. Fert, N. Reyren, and V. Cros, "Magnetic skyrmions: advances in physics and potential applications", Nature Reviews Materials **2**, 1–15 (2017).

Appendix

Table 4.1

c_{11}	168	162.25 ±0.29
c_{33}	193	193.00
c_{23}	55	46.56
c_{12}	64	61.58 ±0.35
c_{44}	61	56.52 ±0.08
c_{14}	-9	-9.01 ±0.04
K_avg	97	91.7
G_avg	57	55.8
v	0.26	0.247
Source	[2]	This work

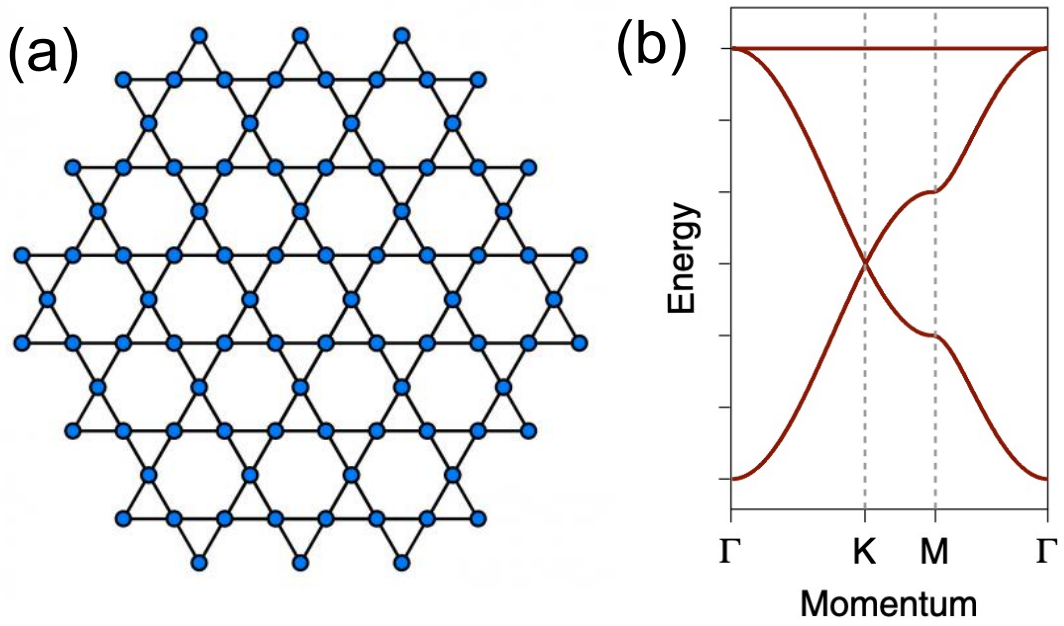

Figure 1.1: (a) Kagome lattice (b) Simplified band structure of kagome metal Fe_3Sn_2. Flat band and Dirac cones coexist.

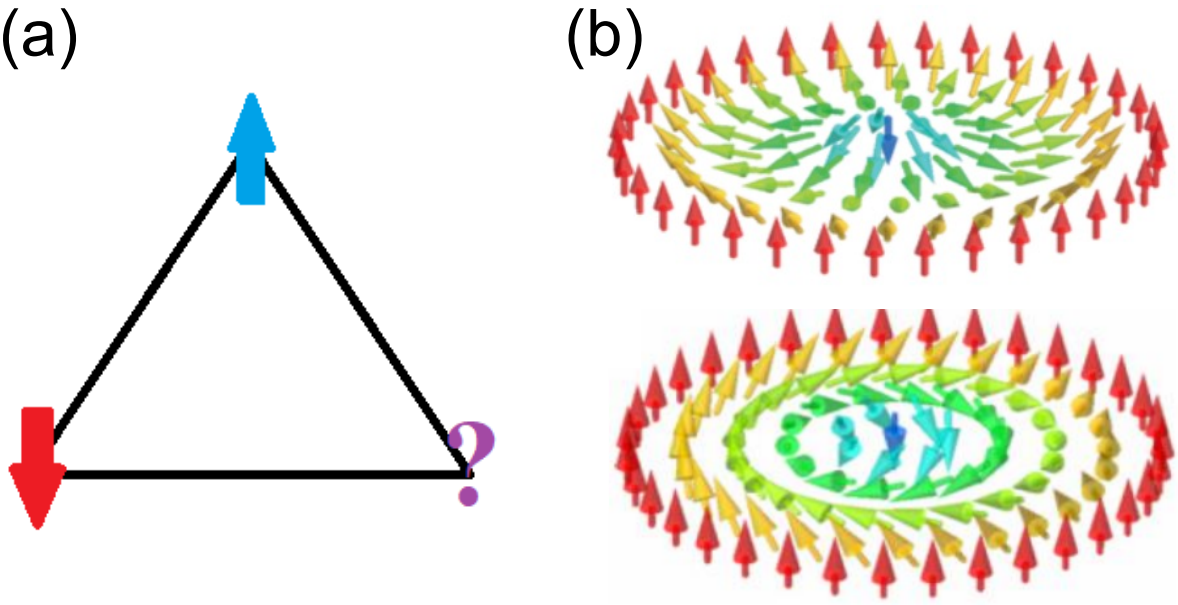

Figure 1.2: (a) Magnetic frustration (b) Two types of Skyrmions. Figures are adopted from [75].

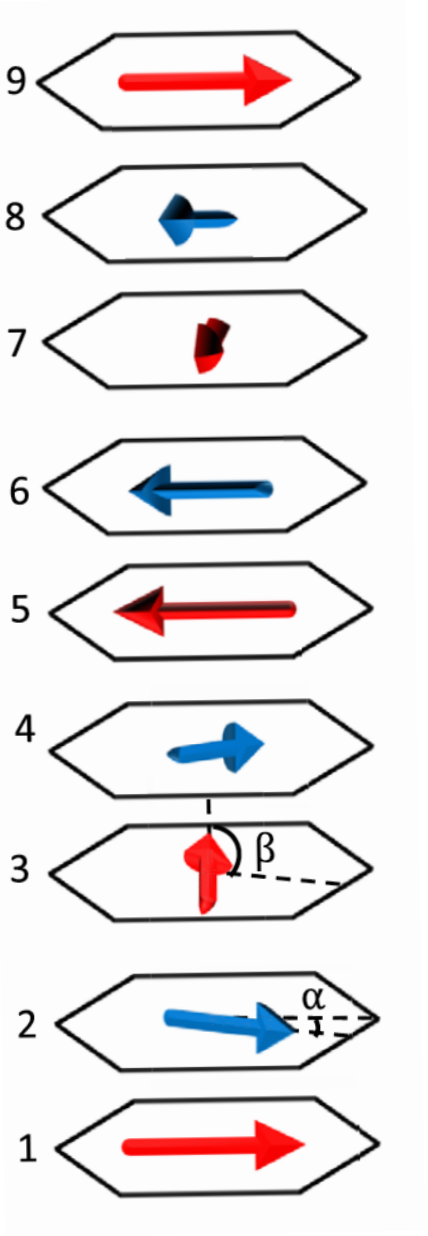

Figure 1.3: Crystal structure of YMn_6Sn_6.The figure is adopted from [33]

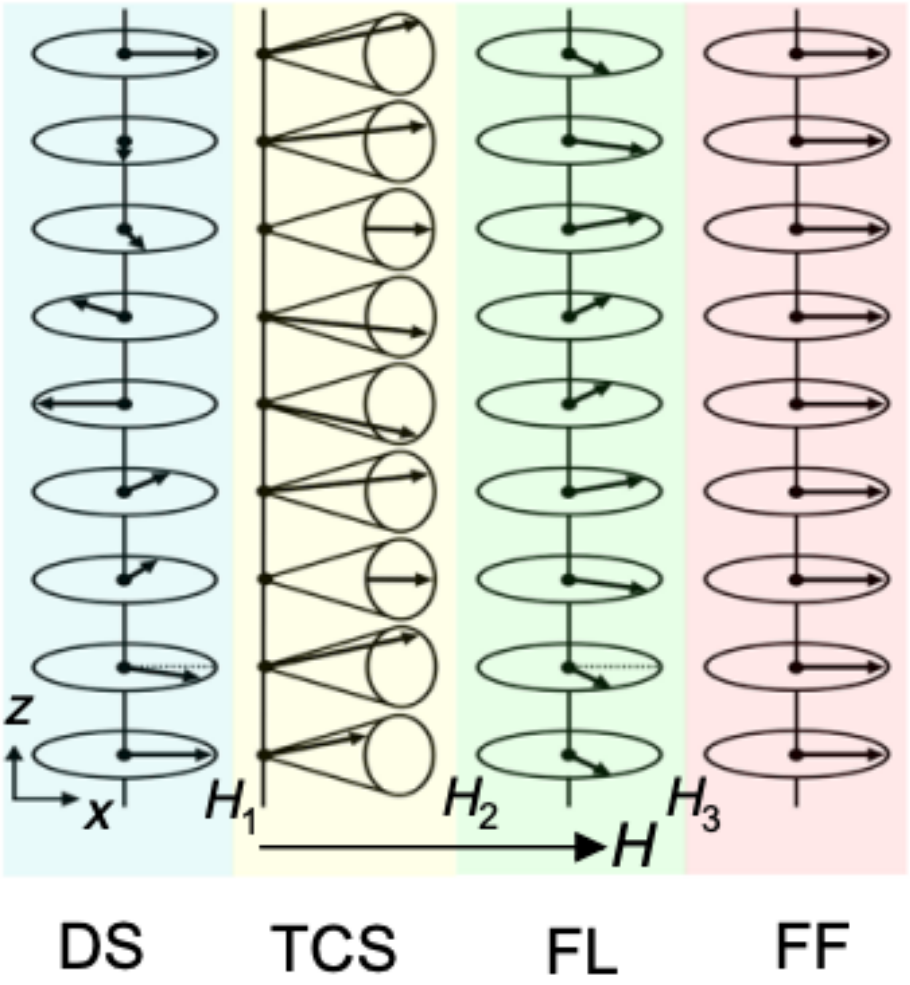

Figure 1.4: 4 magnetic phases in YMn_6Sn_6. The figure ia adopted from [33]

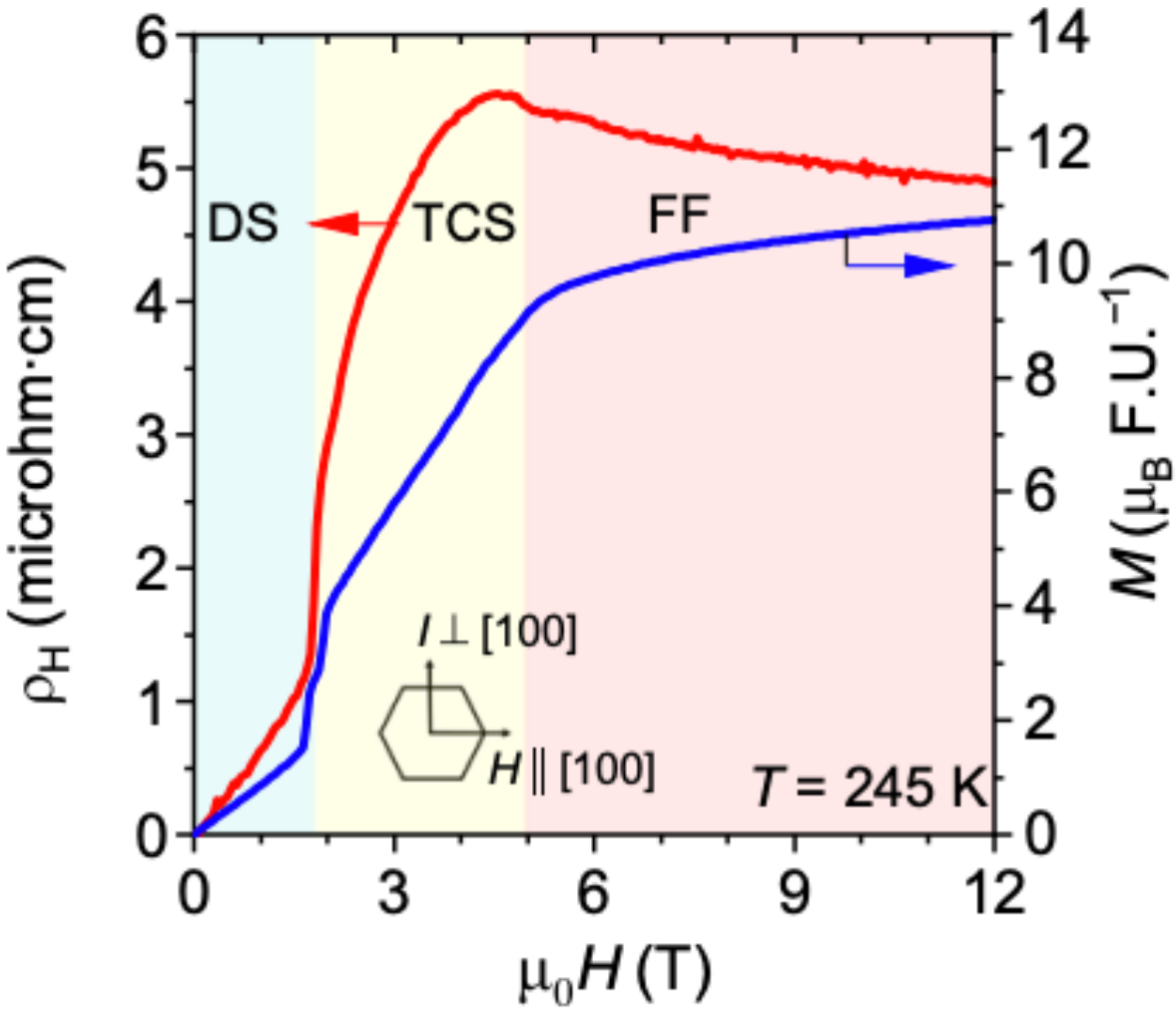

Figure 1.5: YMn_6Sn_6 topological hall effect. The figure is adopted from [33]

Figure 2.1: A sealed quartz tube use for flux growth. A set of crucible is put inside. Chemicals were placed inside the crucible set. Quartz wool was placed on both end inside the tube to prevent form breaking.

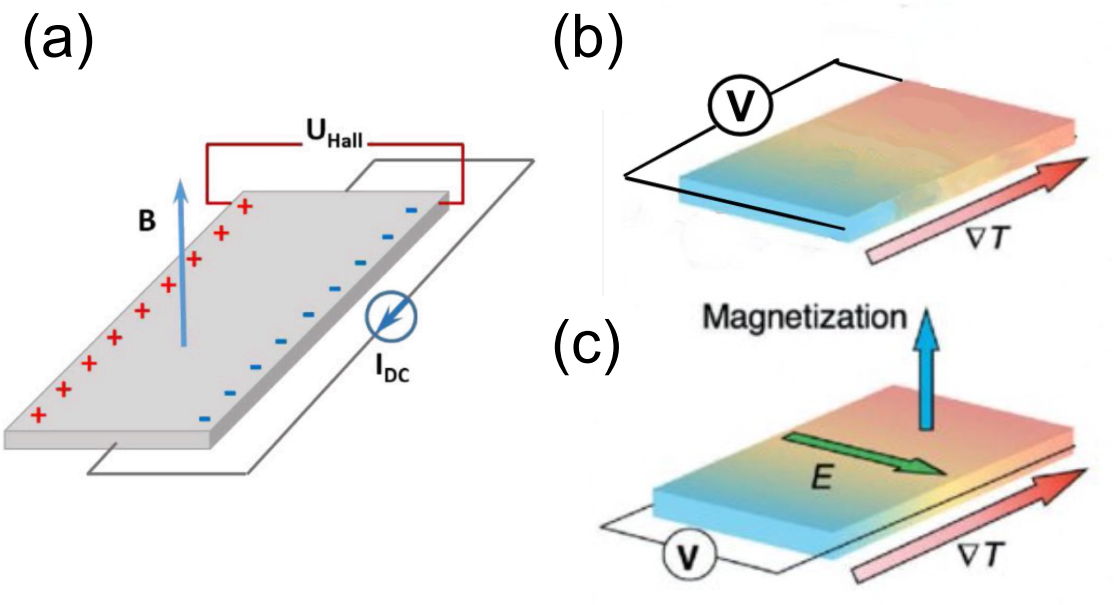

Figure 2.2: (a) Experimental condition for Hall effect. (b) Experimental condition for Seebeck effect. (c) Experimental condition for Nernst effect.

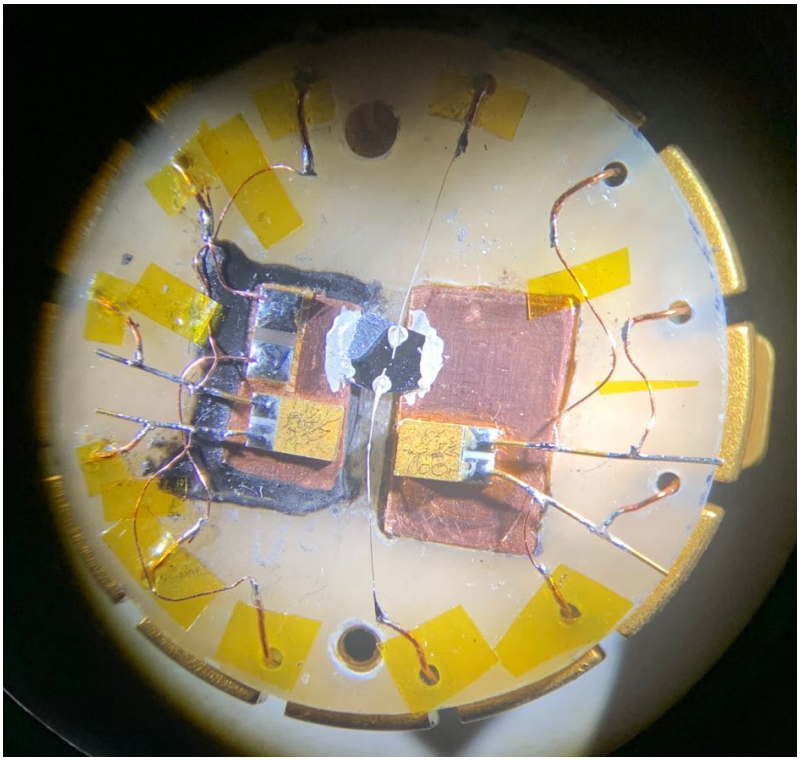

Figure 2.3: Thermoelectric measurement experimental setup

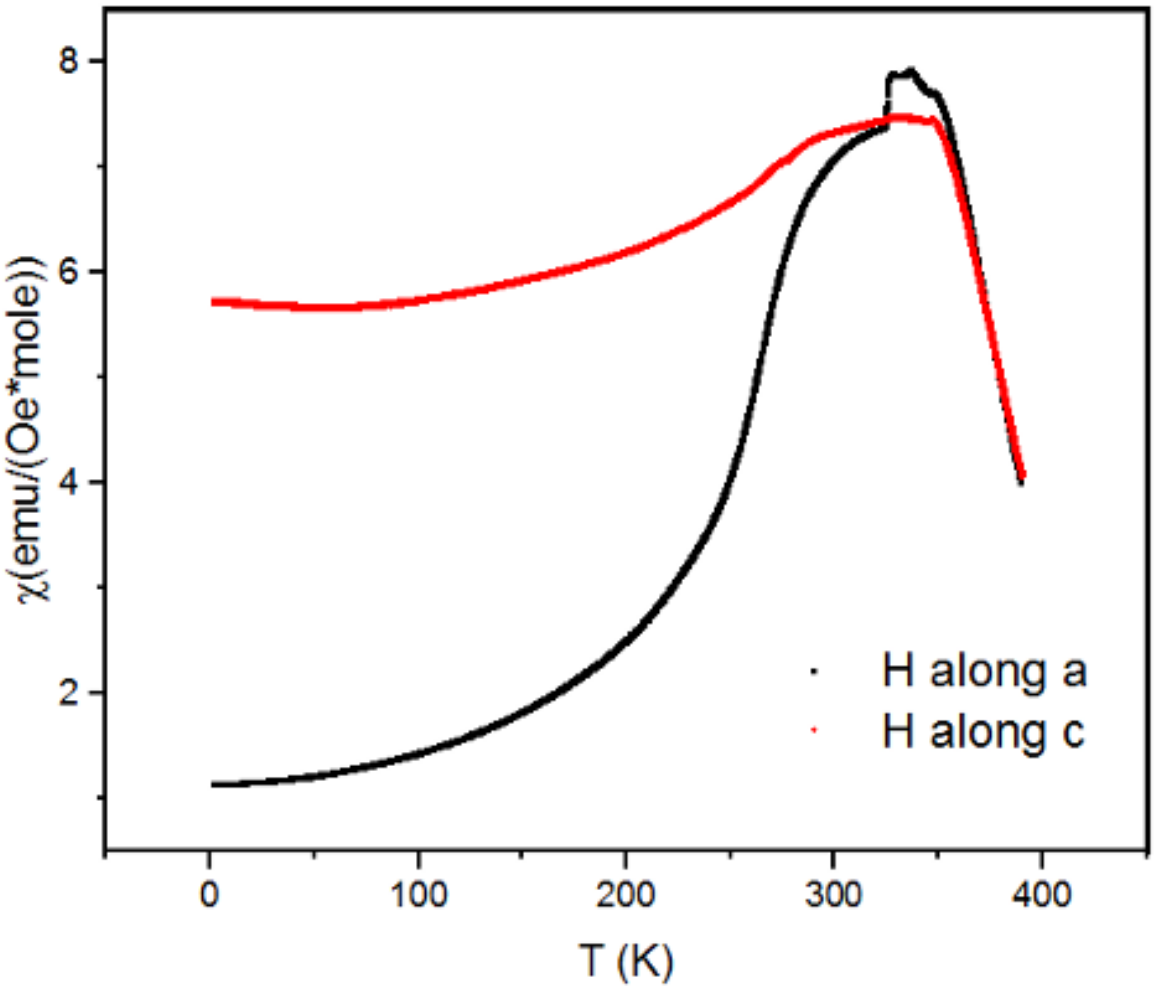

Figure 3.1: Temperature dependent magnetic susceptibility measured respectively when field is along a and c-axis

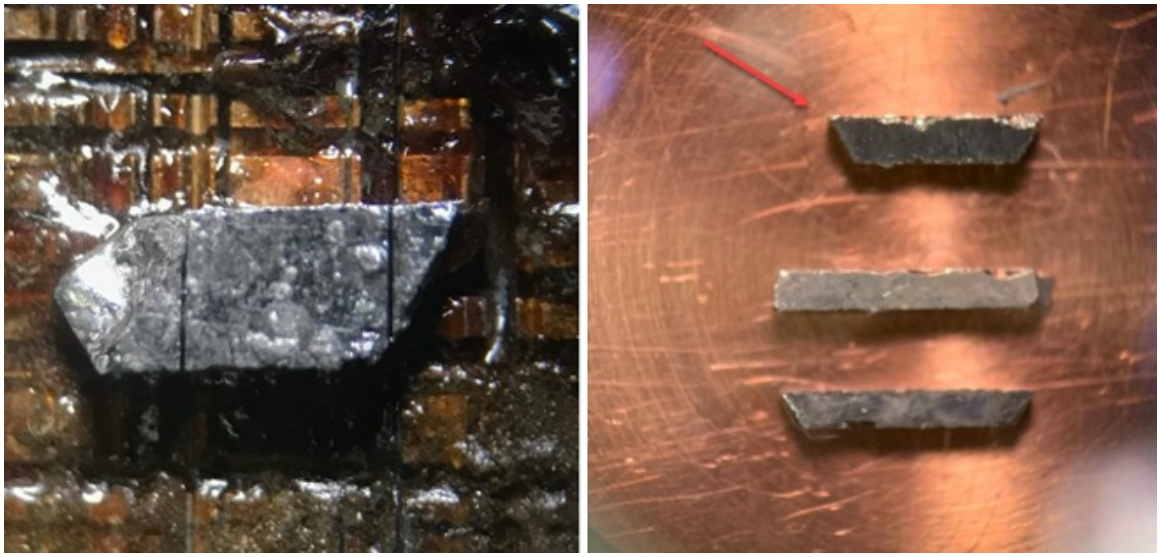

Figure 3.2: Single crystal YMn_6Sn_6 was aligned and cut

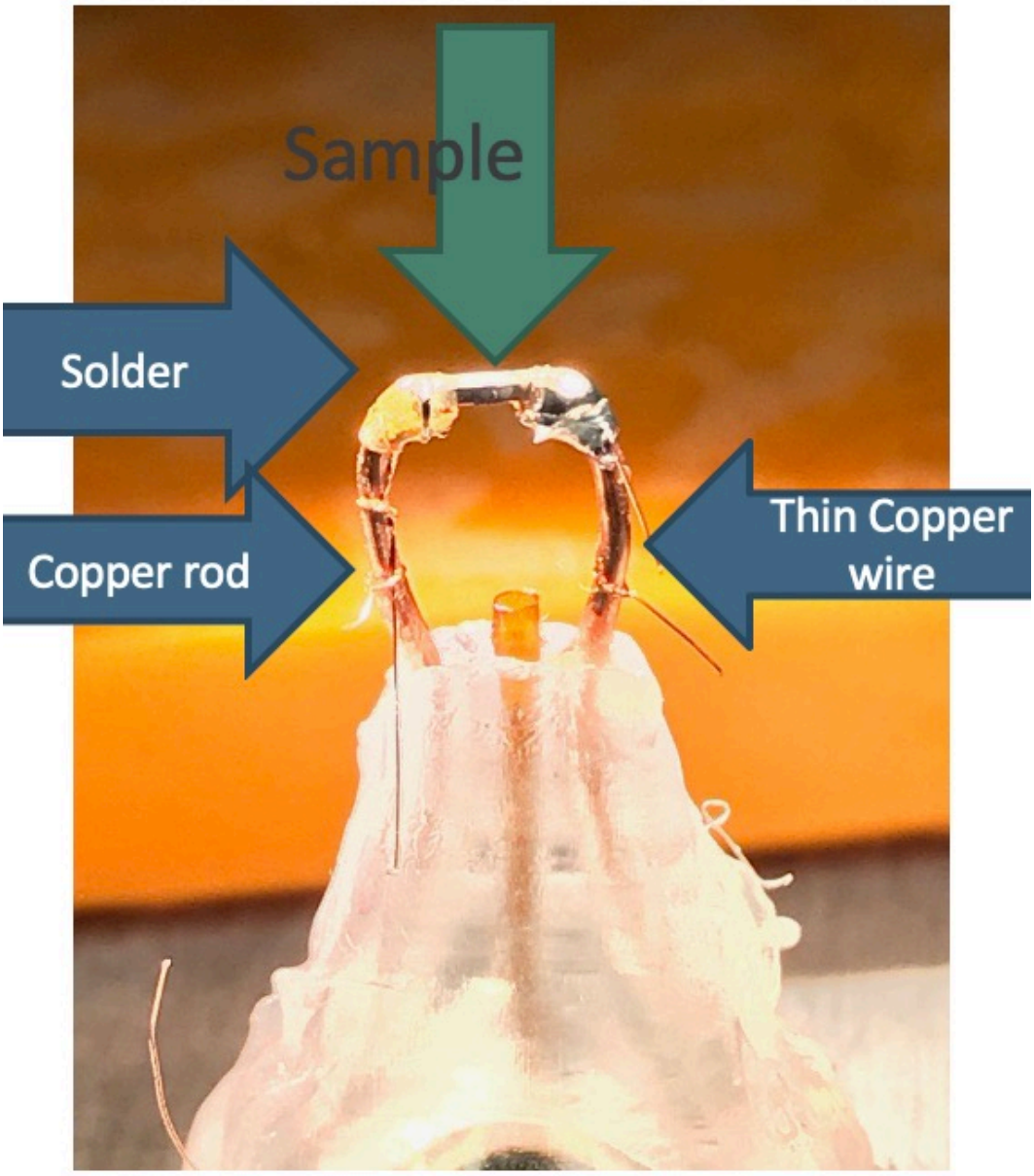

Figure 3.3: Experimental setup for current introduced neutron scattering.

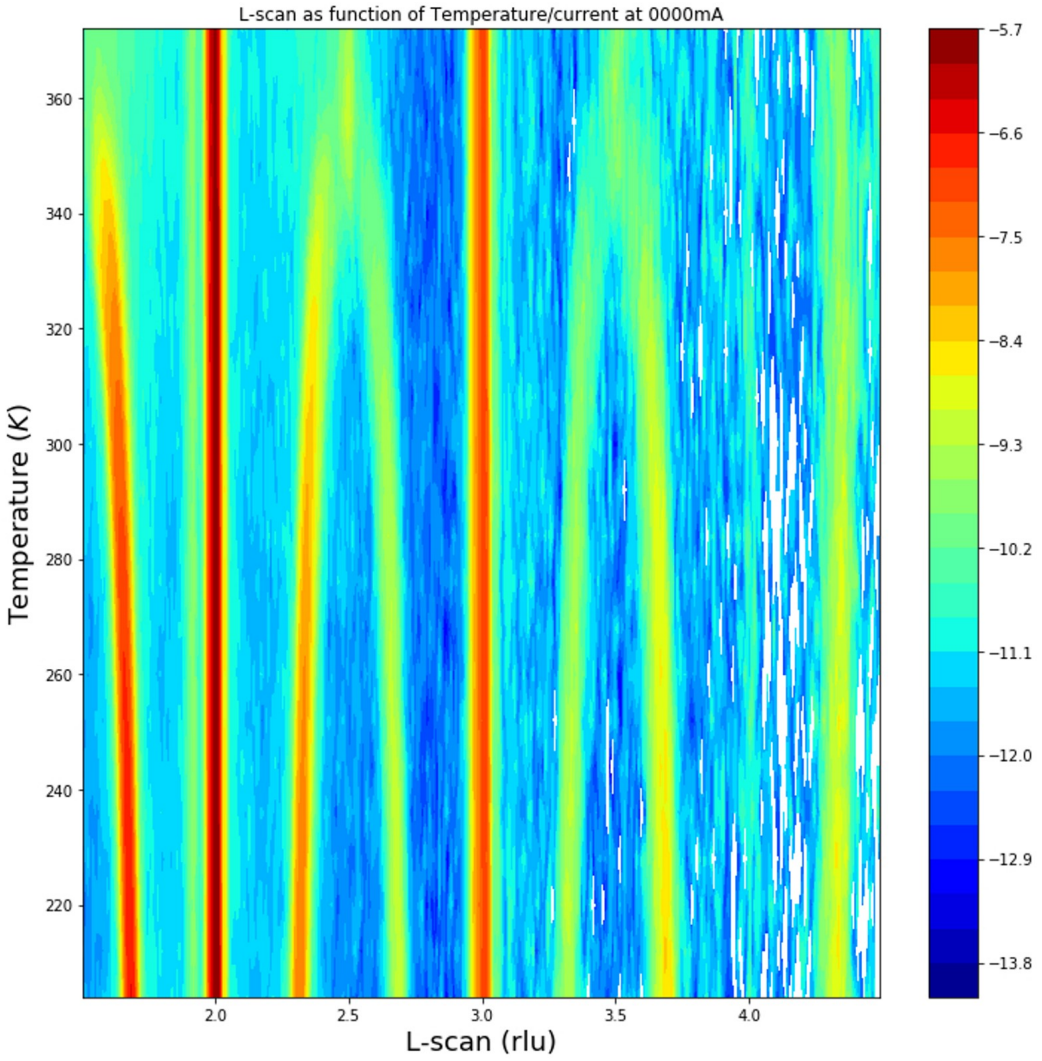

Figure 3.4: (00L) scan with temperature change under 0 A current.

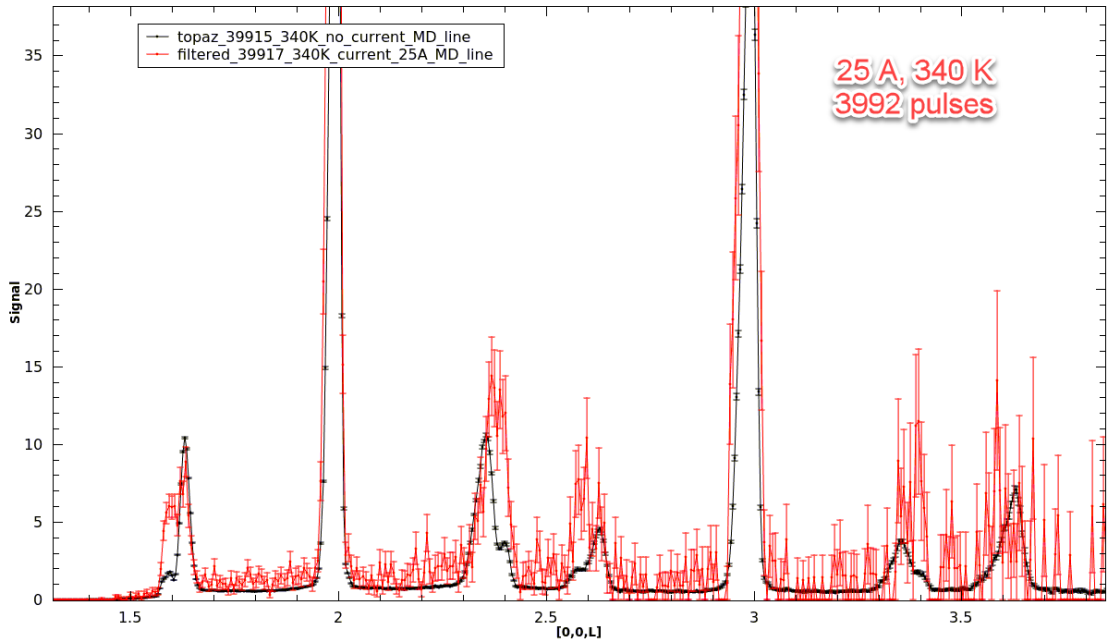

Figure 3.5: The neutron peak comparison between 0 A and 20 A. The temperature is 340 K.

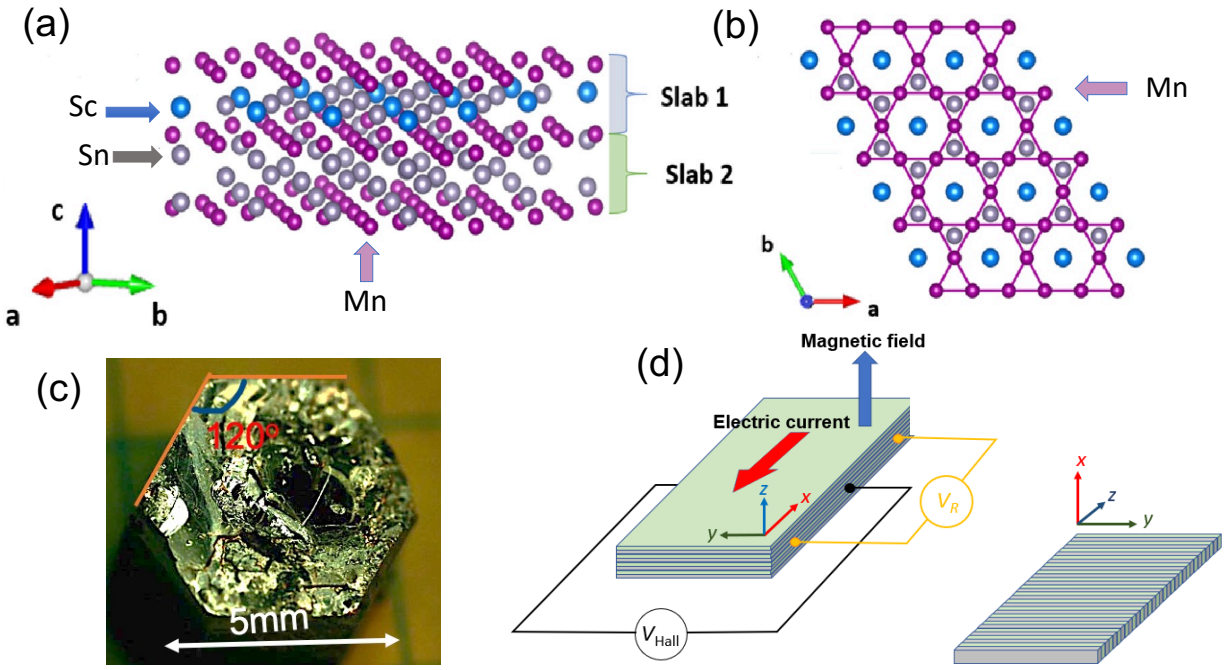

Figure 3.6: (a) Crystal structure. (b) Top-view of crystal structure. (c) Crystal picture. (d) Sample symmetries for Hall effect and MR measurement

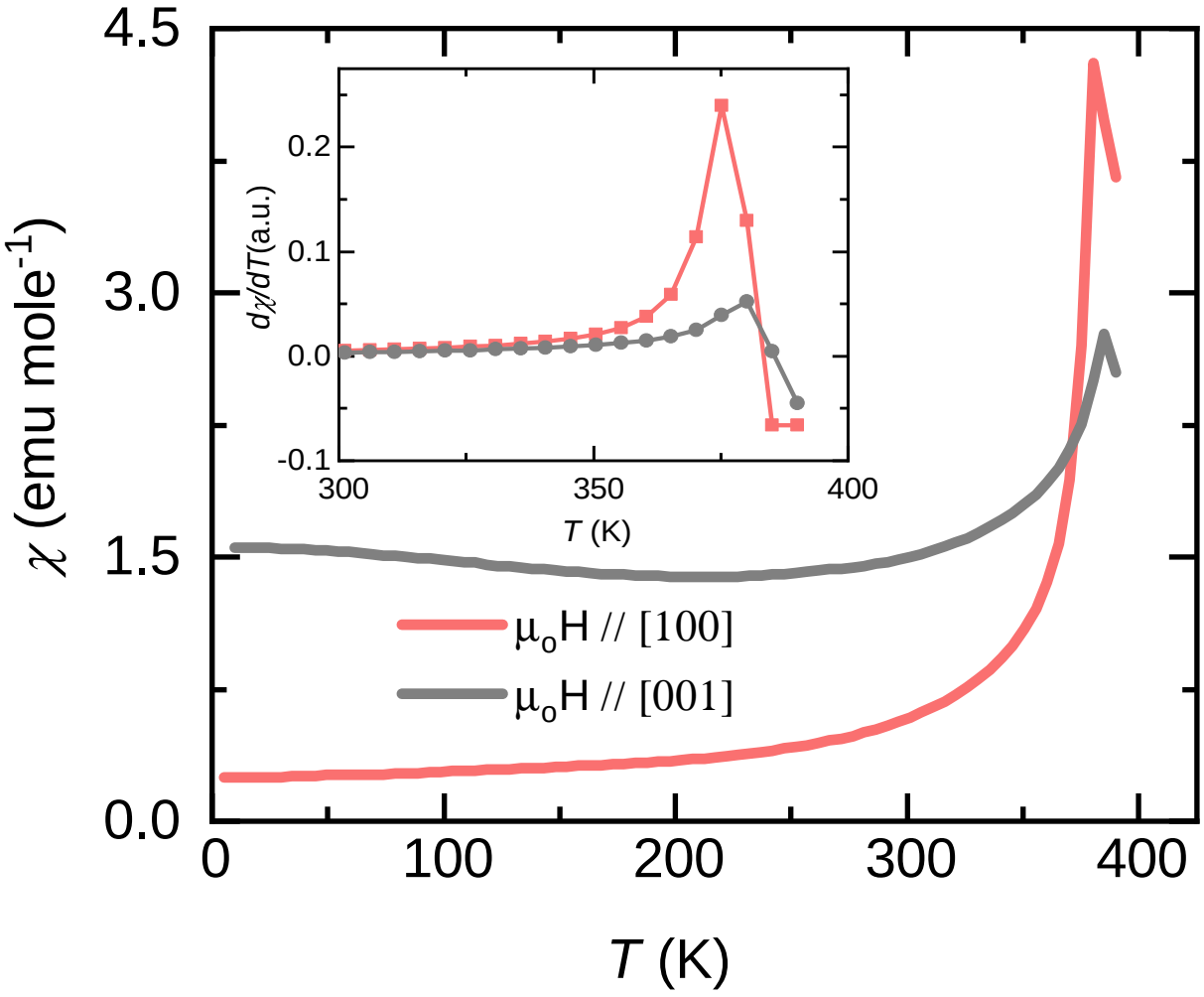

Figure 3.7: Temperature dependence of magnetization and the first derivative for single crystal $ScMn_6Sn_6$. The blue and green colors represent different magnetic field directions.

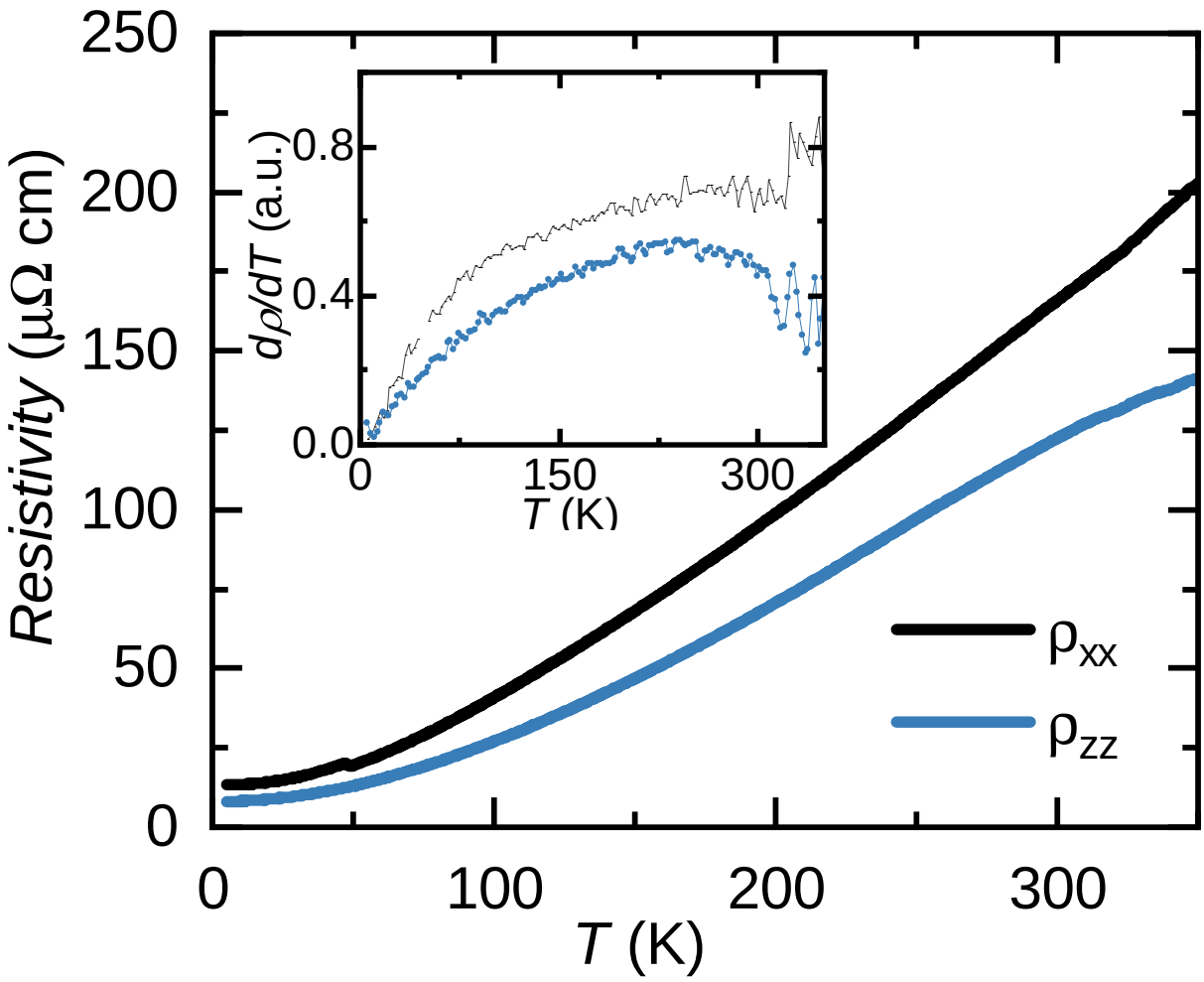

Figure 3.8: Temperature dependence of resistivity and the first derivative for single crystal $ScMn_6Sn_6$. The blue and green colors represent different current field directions.

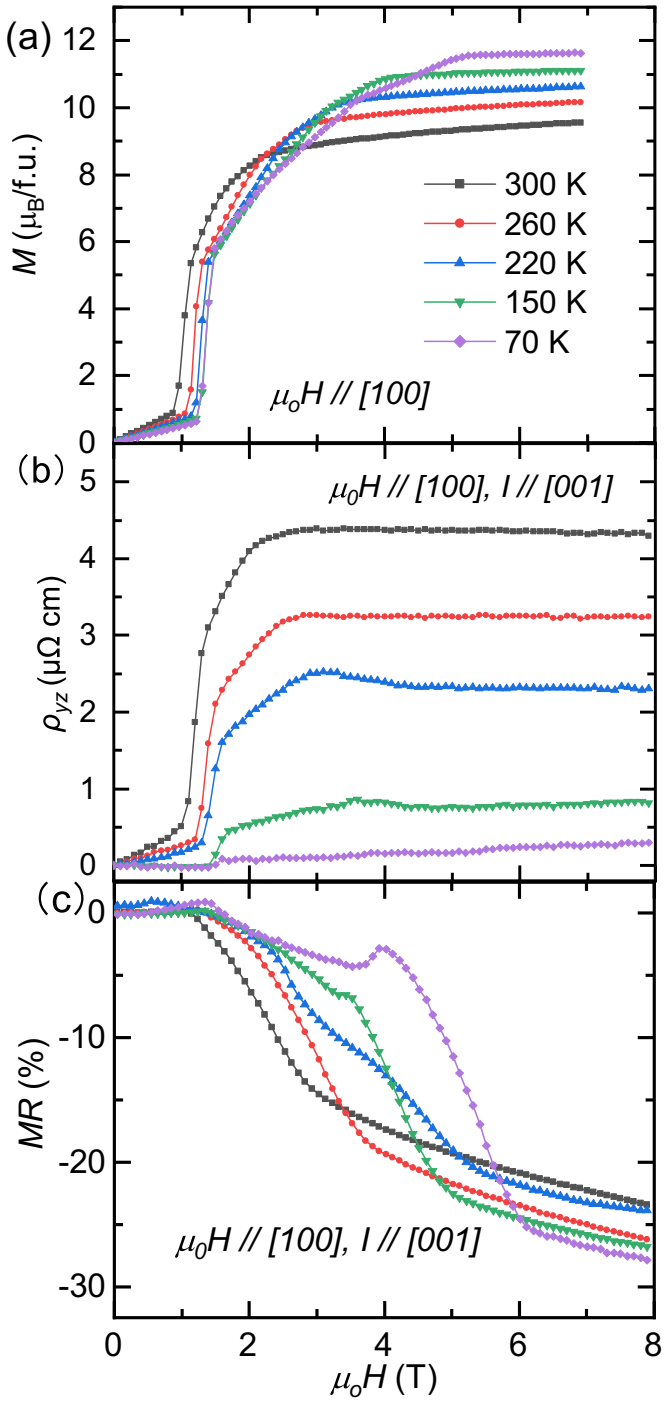

Figure 3.9: (a) Field-dependent magnetization is collected when the magnetic field is set along [100]. (b) Field dependent Hall effect data were collected at different temperatures. The current is along [001], and the magnetic field is along [100]. (c) field-dependent magnetoresistance data was collected at different temperatures. The current is along [001], and the magnetic field is along [100].

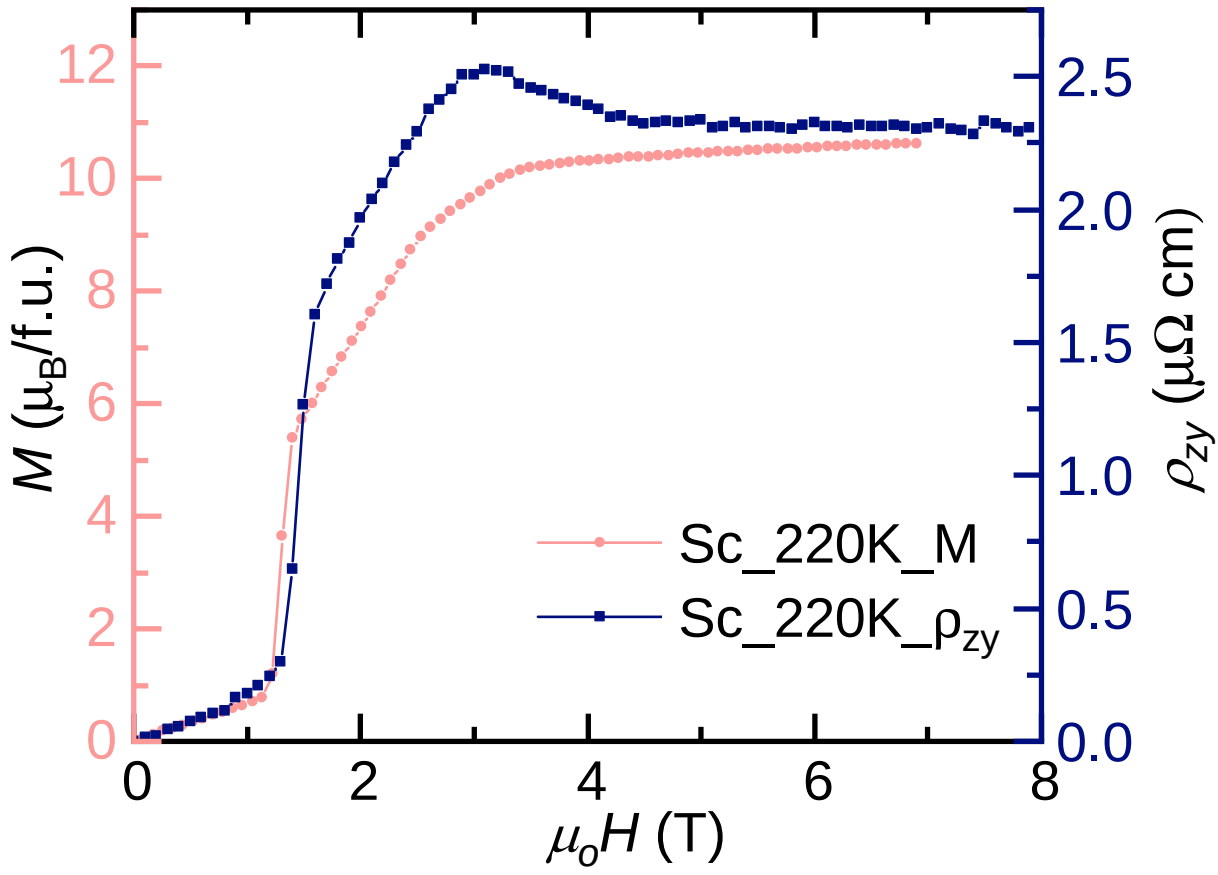

Figure 3.10: M vs H and Hall effect at 220 K on $ScMn_6Sn_6$. Current is along [001], magnetic field is along [100].

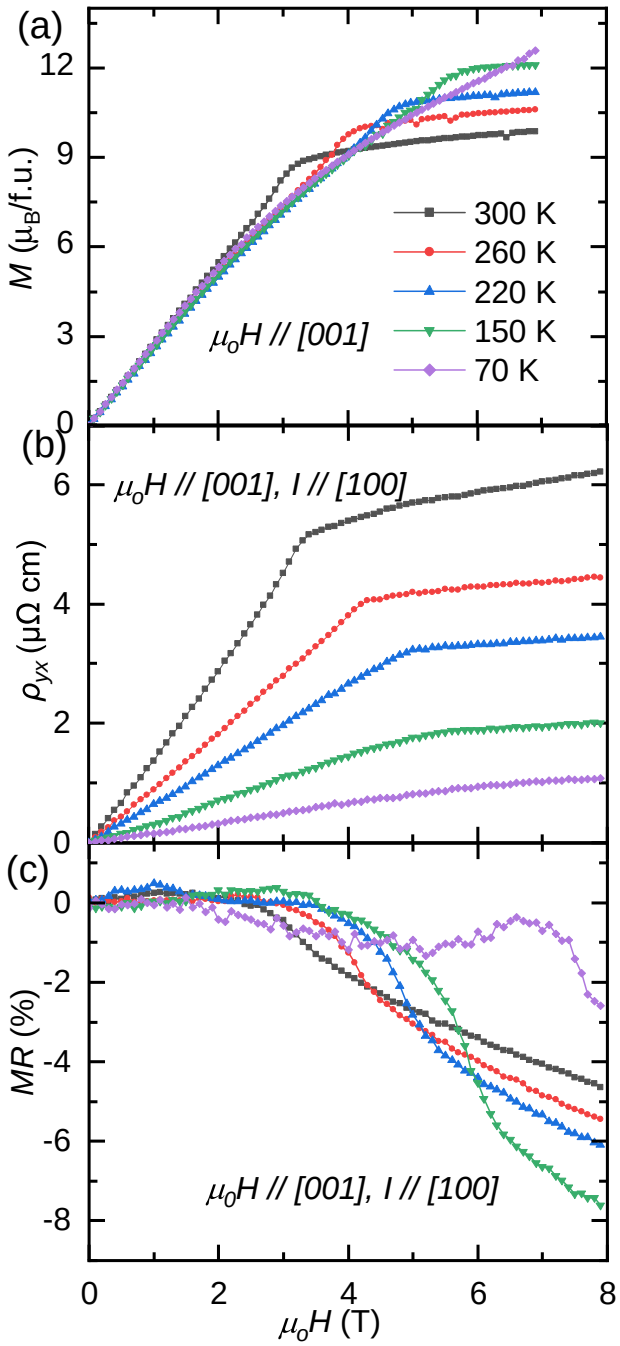

Figure 3.11: (a) field dependent magnetization is collected when the magnetic field is set along [001]. (b) field dependent Hall effect data is collected at different temperatures. The current is along [100], and the magnetic field is along [001]. (c) field dependent magnetoresistance data collected at different temperatures. The current is along [100], and the magnetic field is along [001].

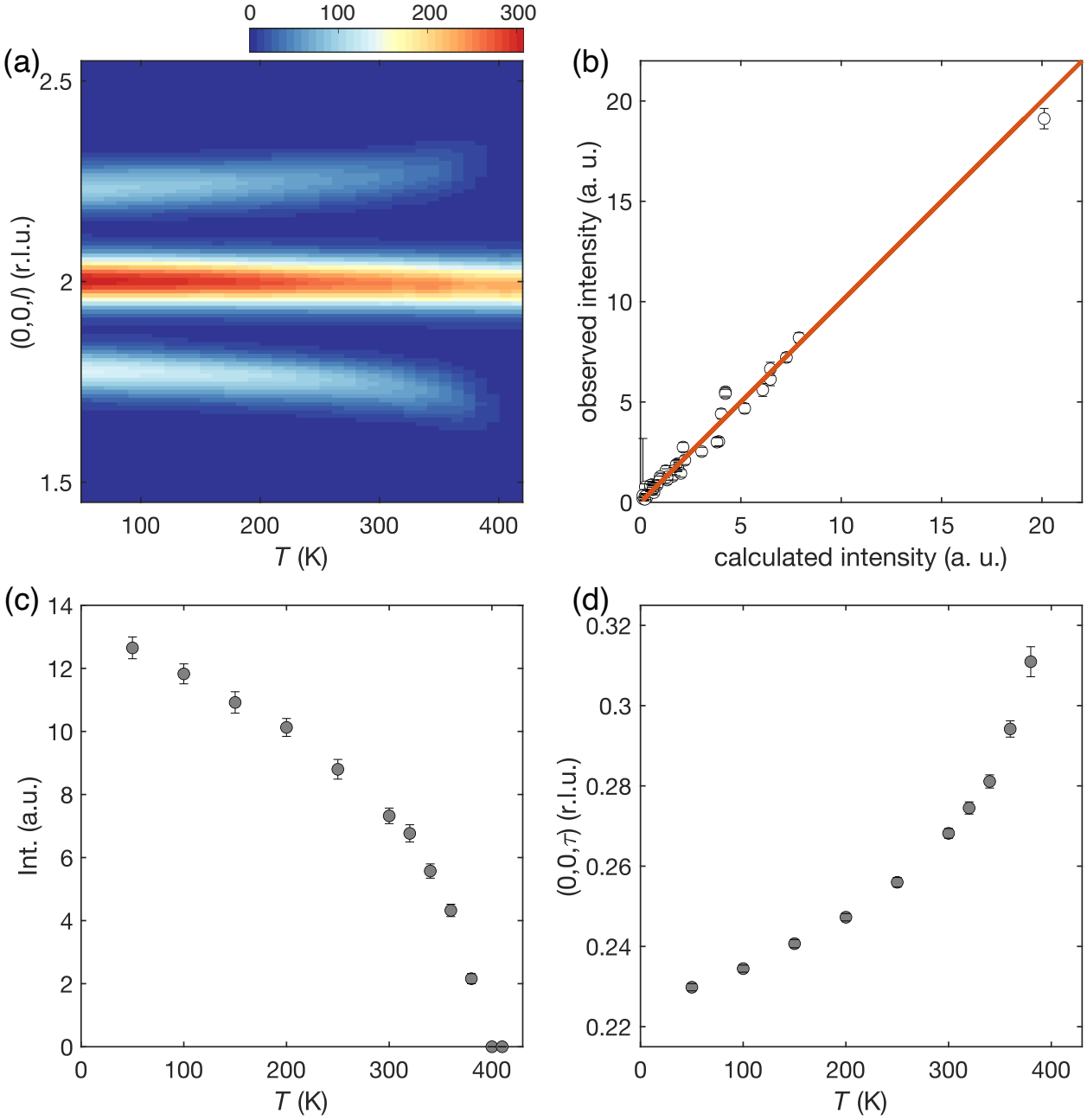

Figure 3.12: (a) Temperature dependence of the magnetic reflections (0,0,2±t) around the (0,0,2) nuclear reflection. (b) Comparison between the experimental and calculated neutron diffraction intensities assuming a double helical magnetic structure. The experimental dataset is collected at T = 15 K. The goodness-of-fit factors are RF2 = 12.1 % and RF = 8.0 %. (c,d) Temperature dependence of the fitted intensity and position of the magnetic reflection (0,0,2+t).

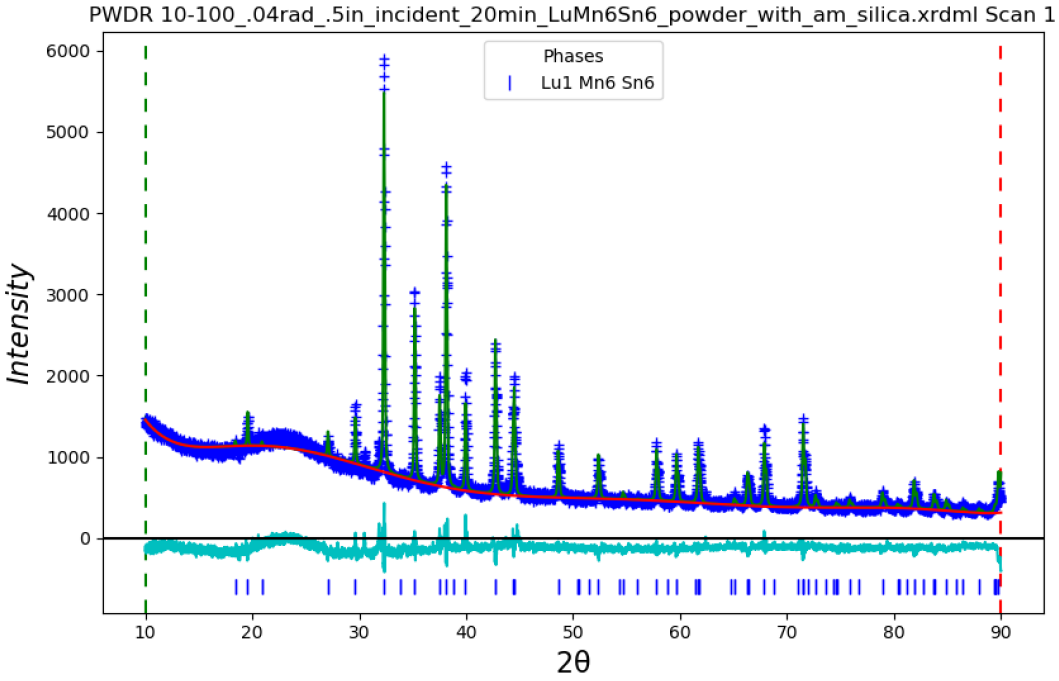

Figure 3.13: Powder X-ray diffraction for $LuMn_6Sn_6$

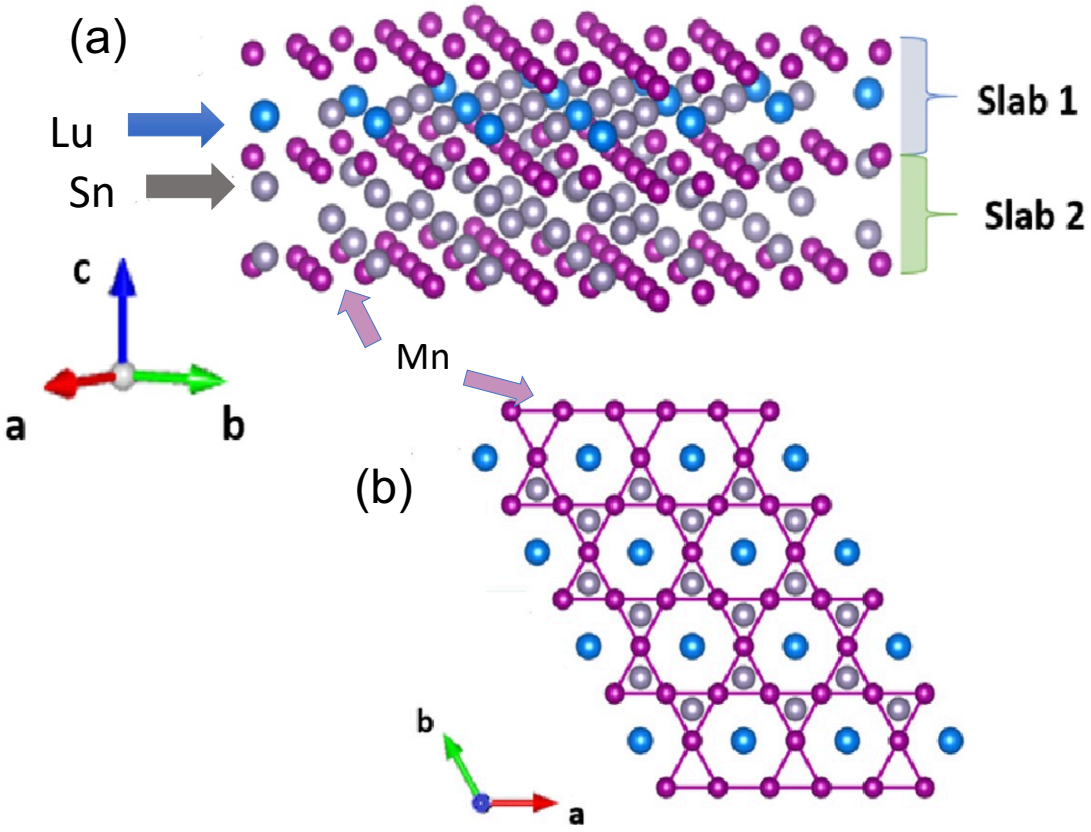

Figure 3.14: Three dimensional and top view Crystal structure of $LuMn_6Sn_6$

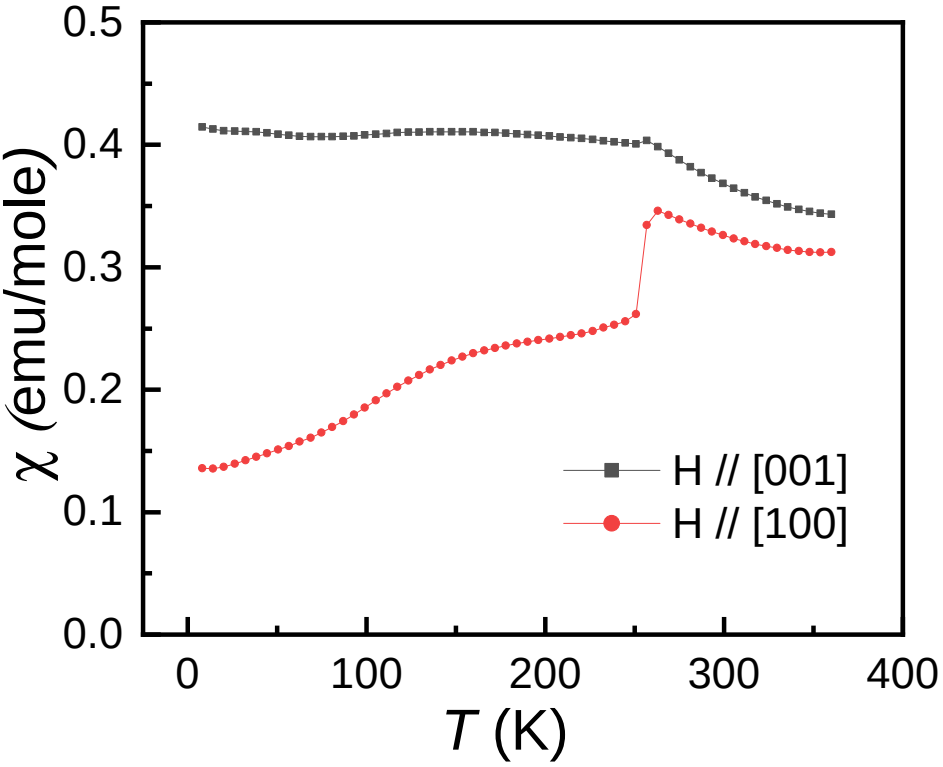

Figure 3.15: Temperature dependence of magnetization and the first derivative for single crystal $LuMn_6Sn_6$. Black and red color represent the different magnetic field directions.

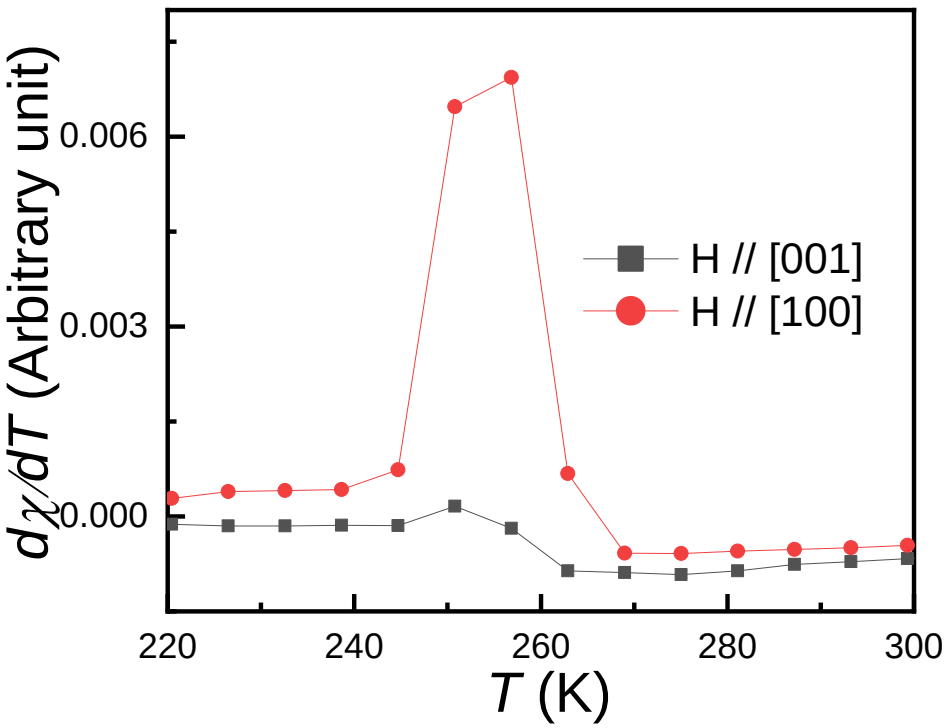

Figure 3.16: Temperature dependence of magnetization and the first derivative for single crystal $LuMn_6Sn_6$. Black and red color represent the different magnetic field directions.

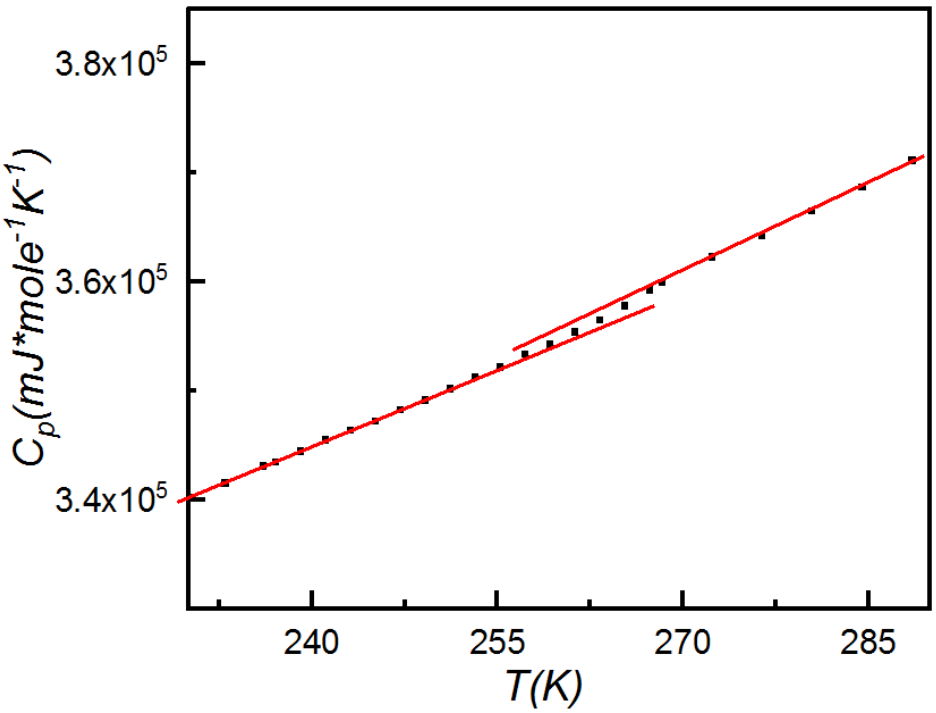

Figure 3.17: Heat capacity vs temperature. Data points were taken by PPMS.

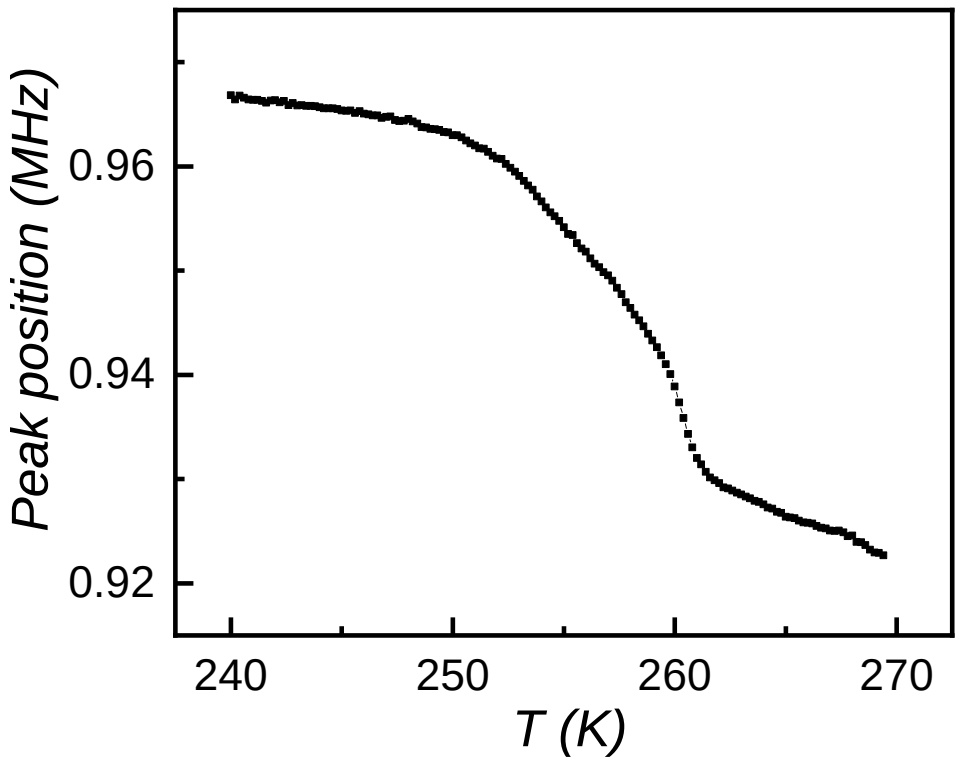

Figure 3.18: One ultrasound resonance position changes with temperature change

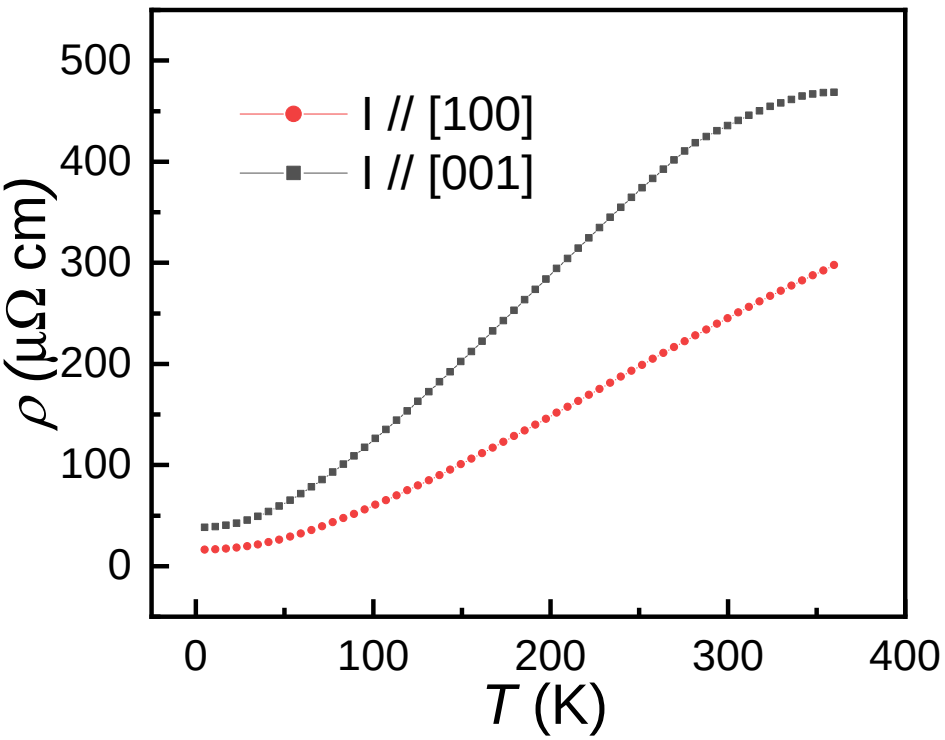

Figure 3.19: Heat capacity vs temperature. Data points were taken by PPMS.

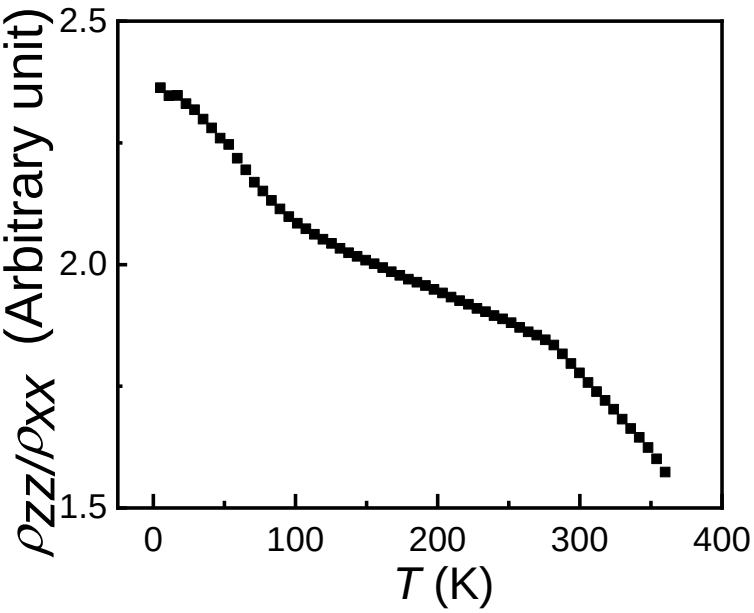

Figure 3.20: Temperature dependent ρ_{zz}/ρ_{xx}

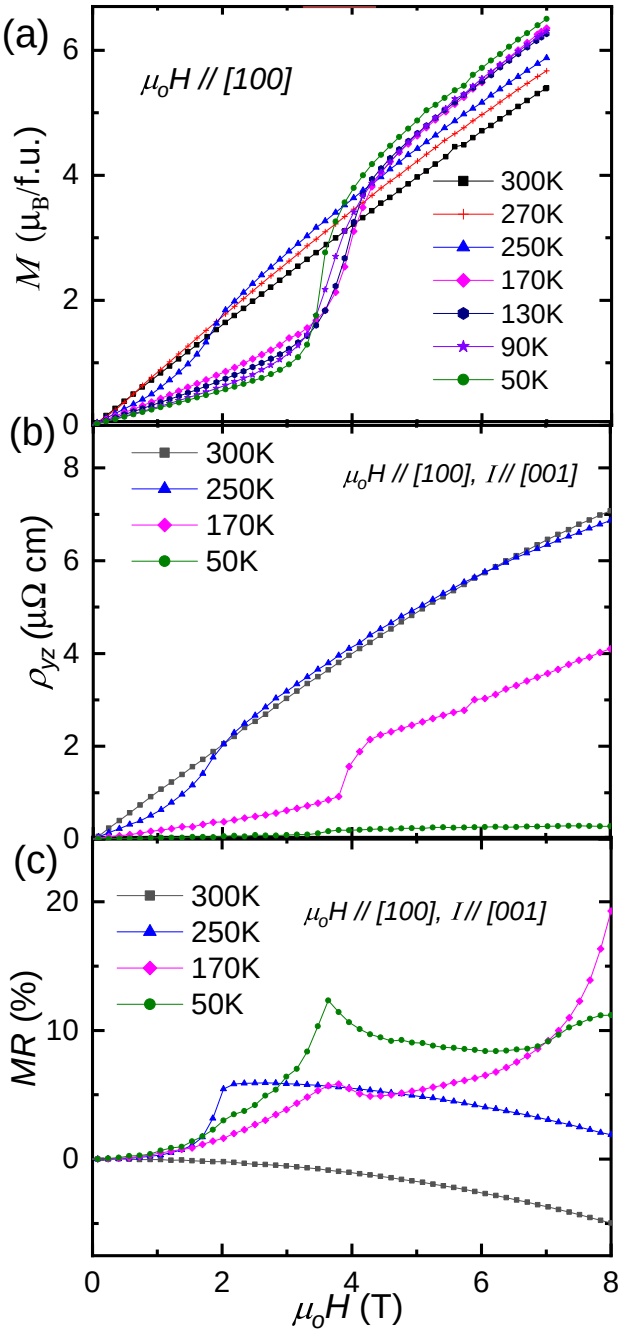

Figure 3.21: Field dependence on Magnetization, Hall effect, and magnetoresistance, respectively, when the field is along [100]. Colors showed the data taken under different temperatures.

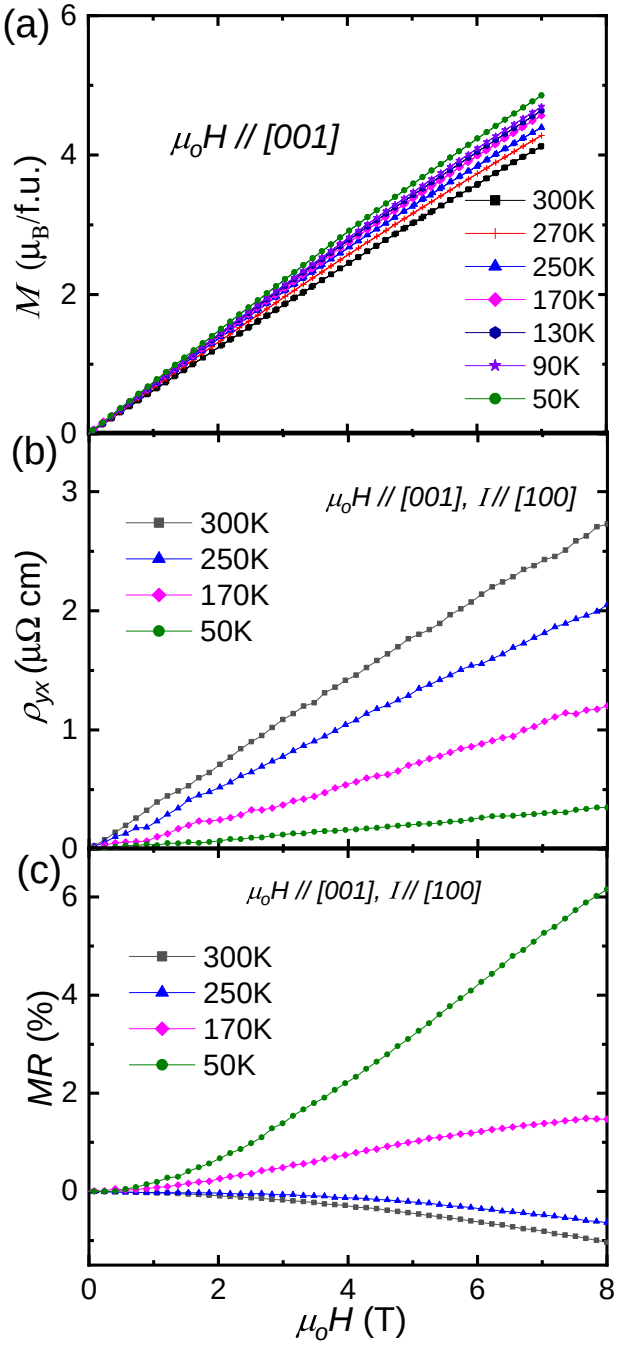

Figure 3.22: Field dependence on Magnetization, Hall effect and magneto resistance respectively when field is along (100). Colors showed the data taken under different temperatures.

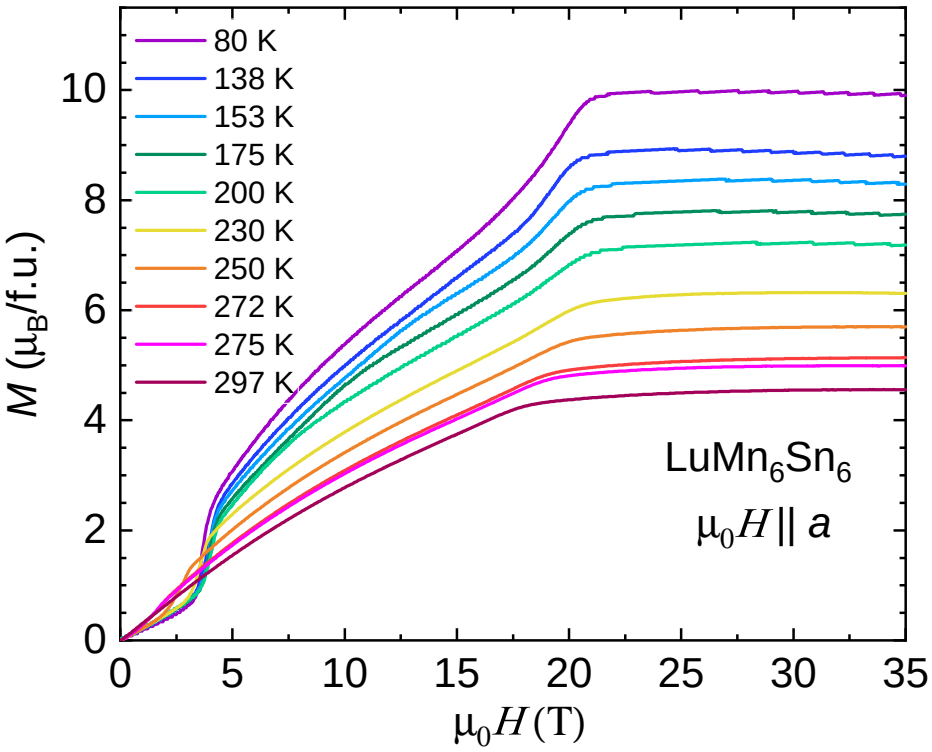

Figure 3.23: Field dependent magnetization when large field is along [001]. Colors showed the data taken under different temperatures.

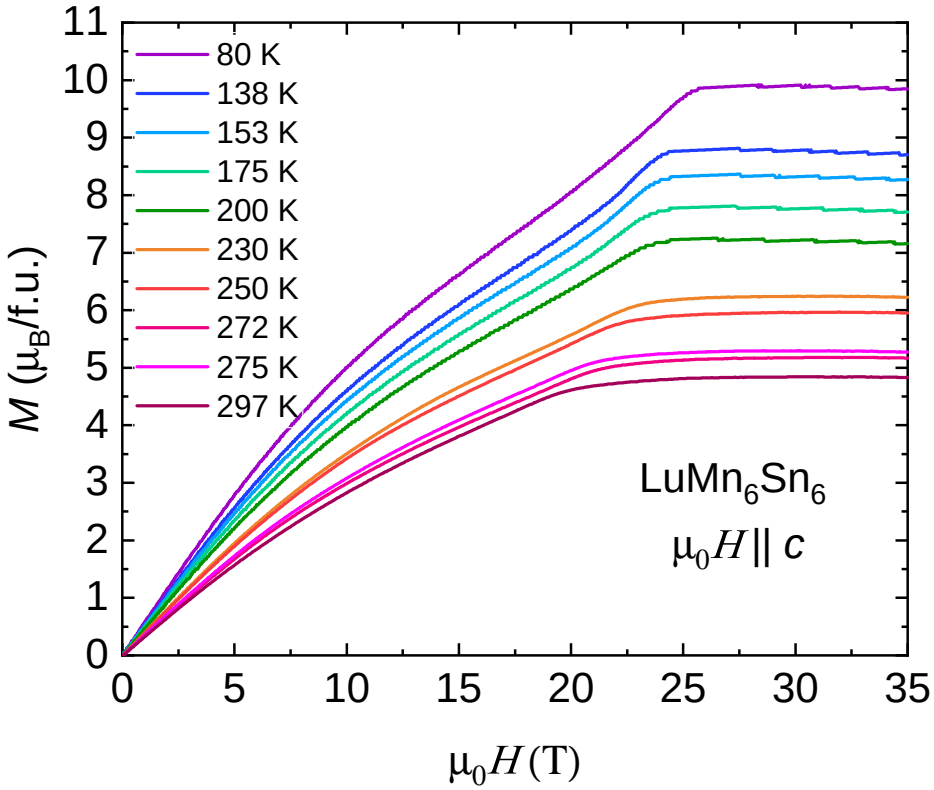

Figure 3.24: Field dependent magnetization when large field is along [100]. Colors showed the data taken under different temperatures.

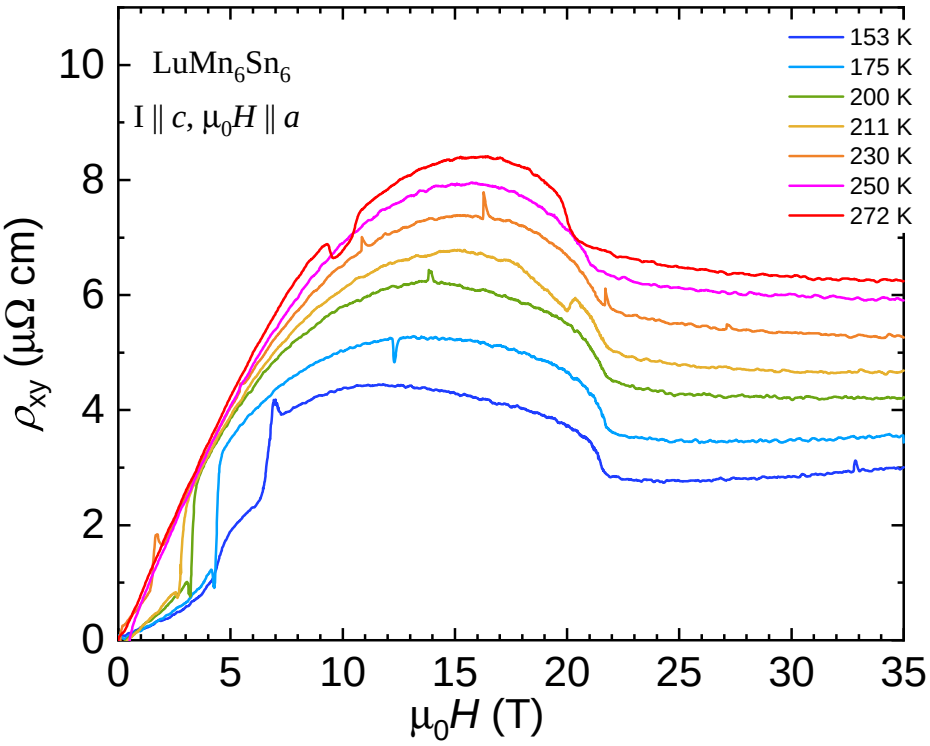

Figure 3.25: Field dependence on Hall effect when large field is along [001] and current is along [100]. Colors showed the data taken under different temperatures.

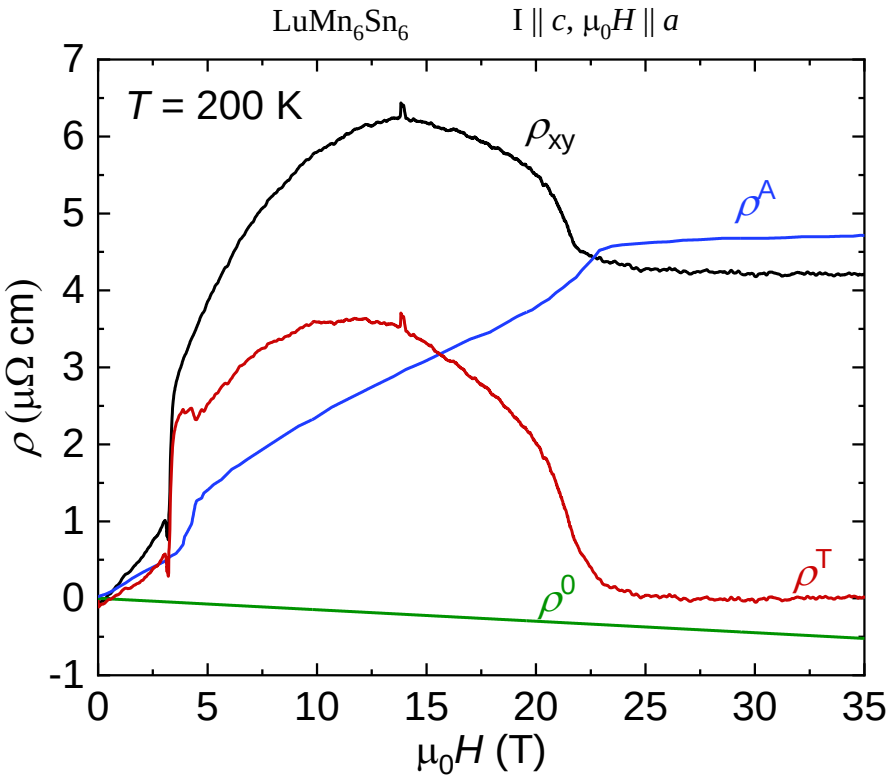

Figure 3.26: Field dependence on magneto resistance when large field is along (100). Colors showed the data taken under different temperatures.

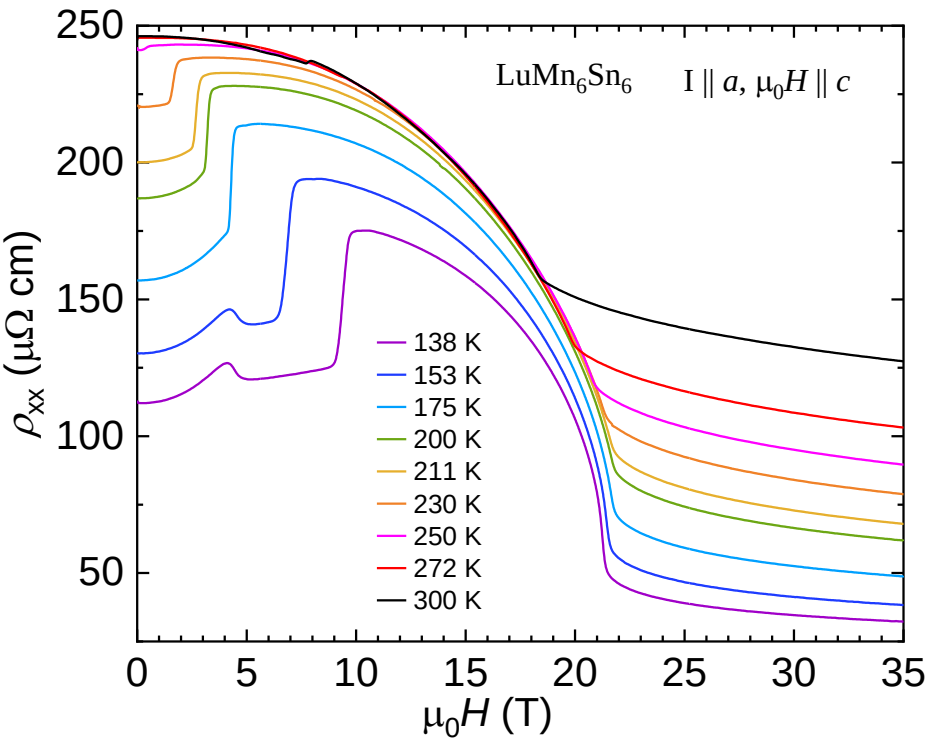

Figure 3.27: Field dependent magneto resistance of $LuMn_6Sn_6$.The magnetic field is along [001] and the current is along [100].

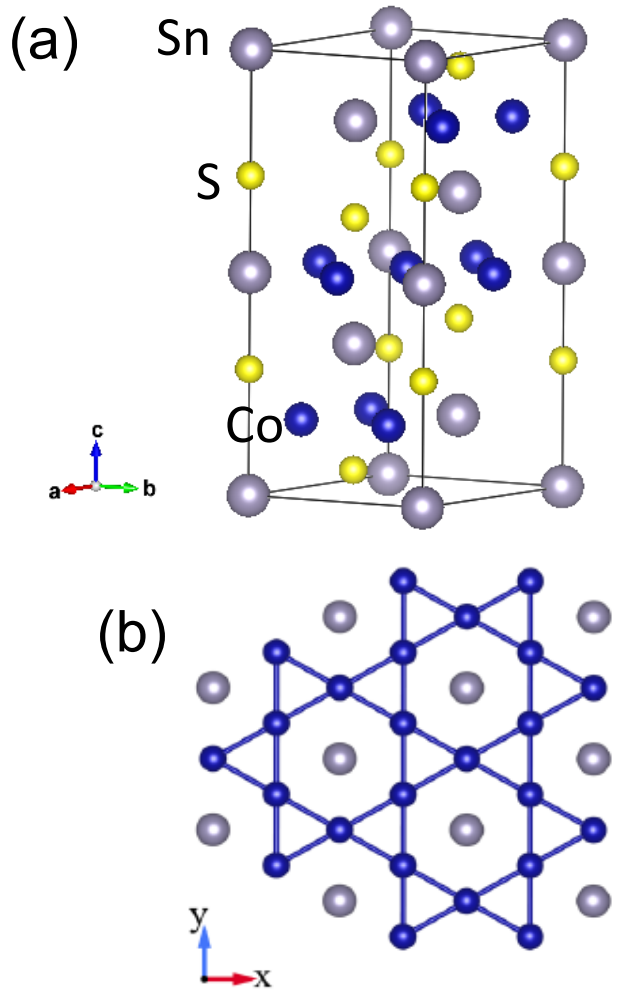

Figure 4.1: (a)Crystal structures of the single crystal $Co_3Sn_2S_2$, Grey element is Sn, Blue element is Co and yellow element is S.(b) The top view of the crystal structure.

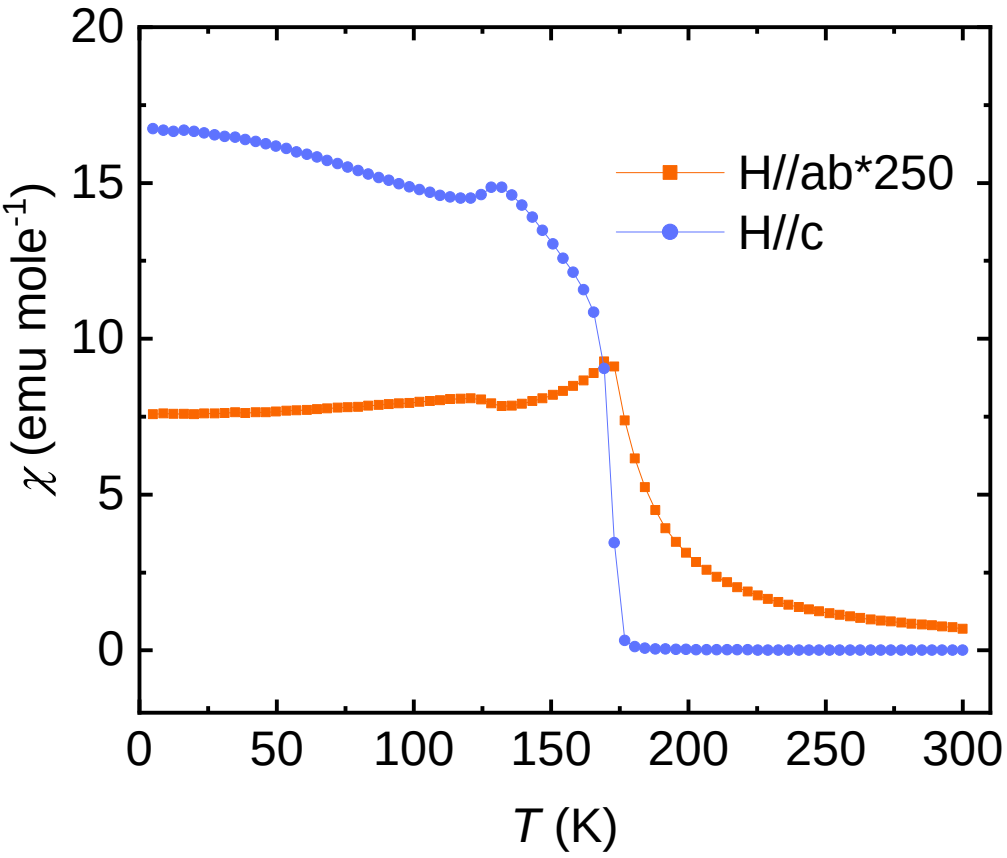

Figure 4.2: $Co_3Sn_2S_2$ magnetic susceptibility measured when field is along different crystal orientations. The blue curve was taken when magnetic field is along c-axis. The red curve was taken when magnetic field is along a-axis. The value of red curve is timed 250 times.

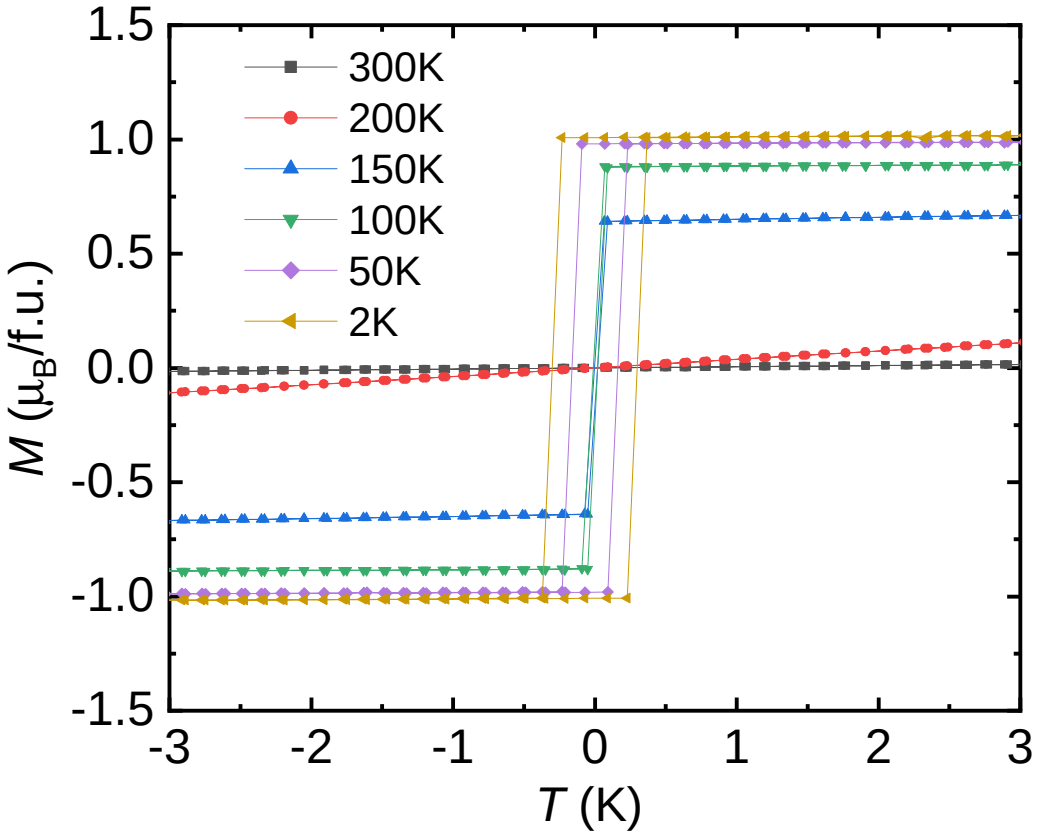

Figure 4.3: M vs H, magnetic field is along c-axis.

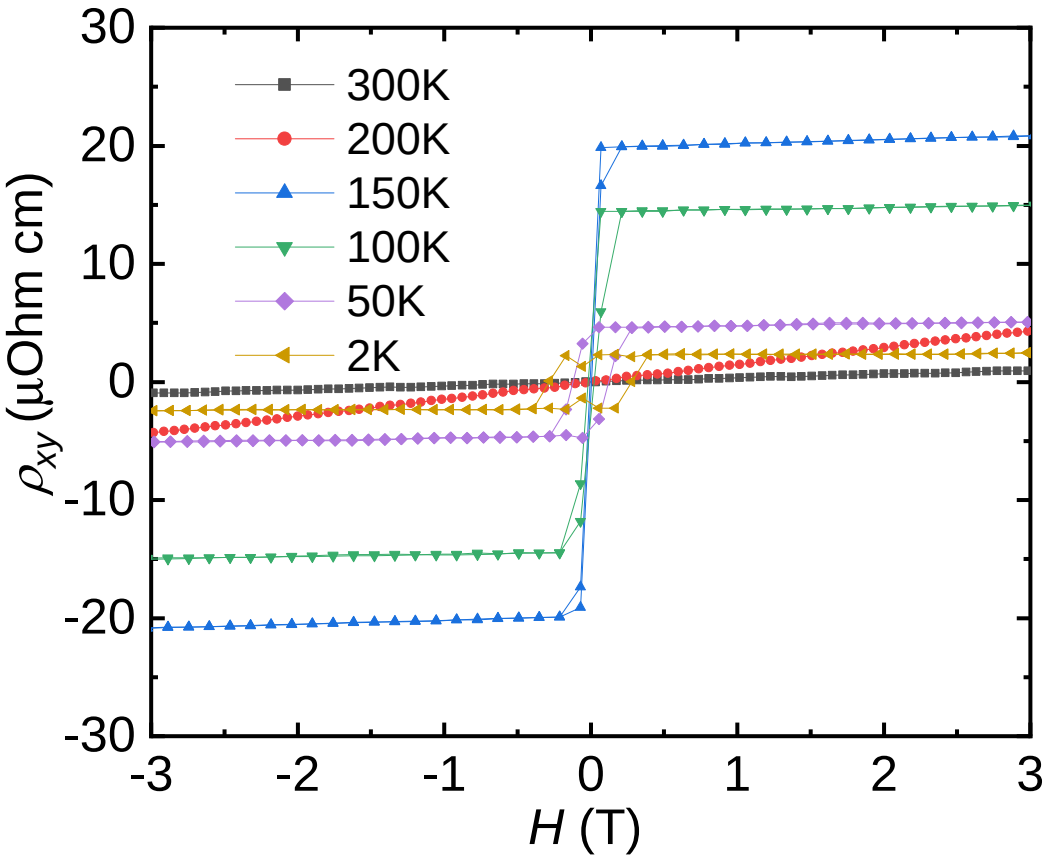

Figure 4.4: Hall resistivity measured when field is along c-axis.

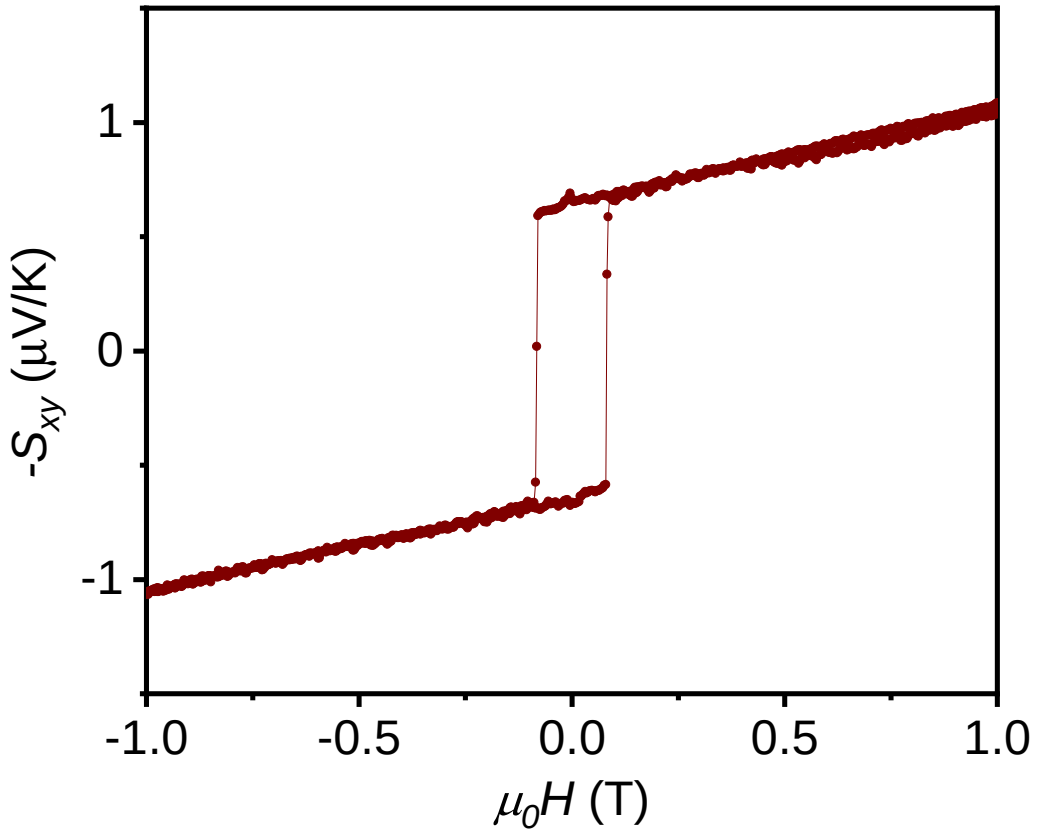

Figure 4.5: Nernst coefficient measured on flux grown single crystal. The temperature is set as 30 K.

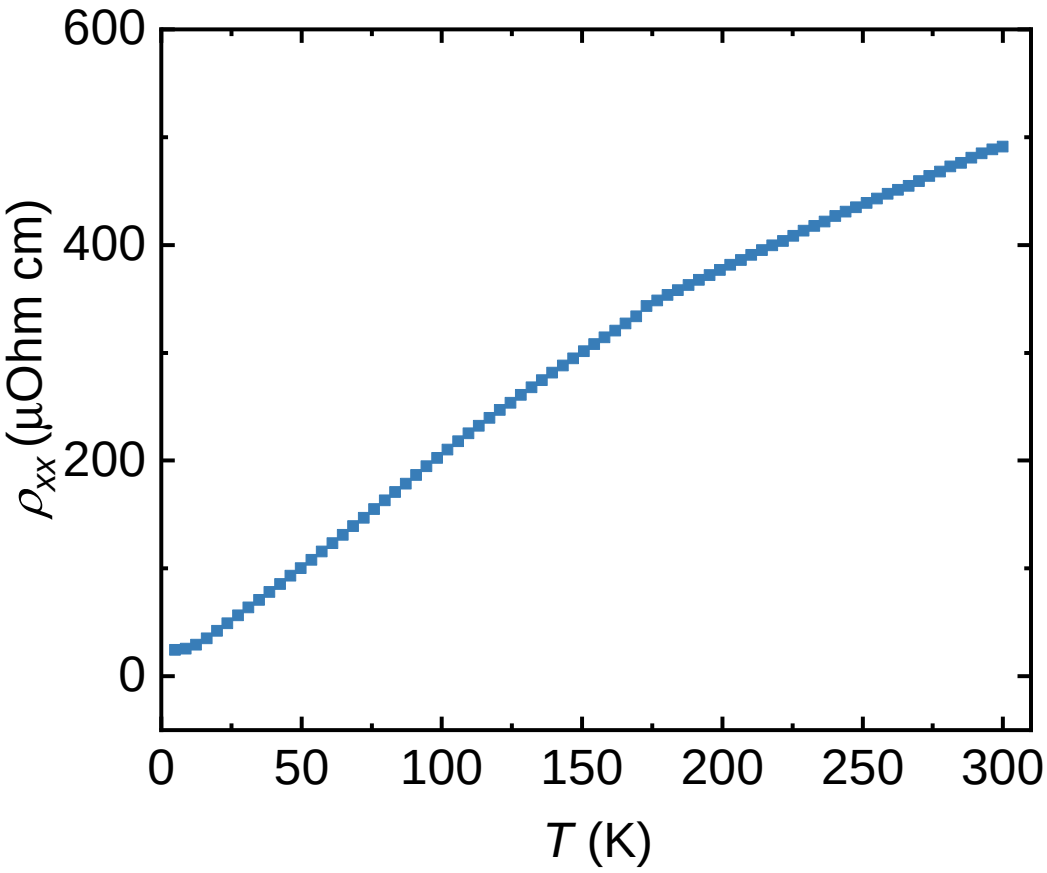

Figure 4.6: Resistivity measurement on $Co_3Sn_2S_2$

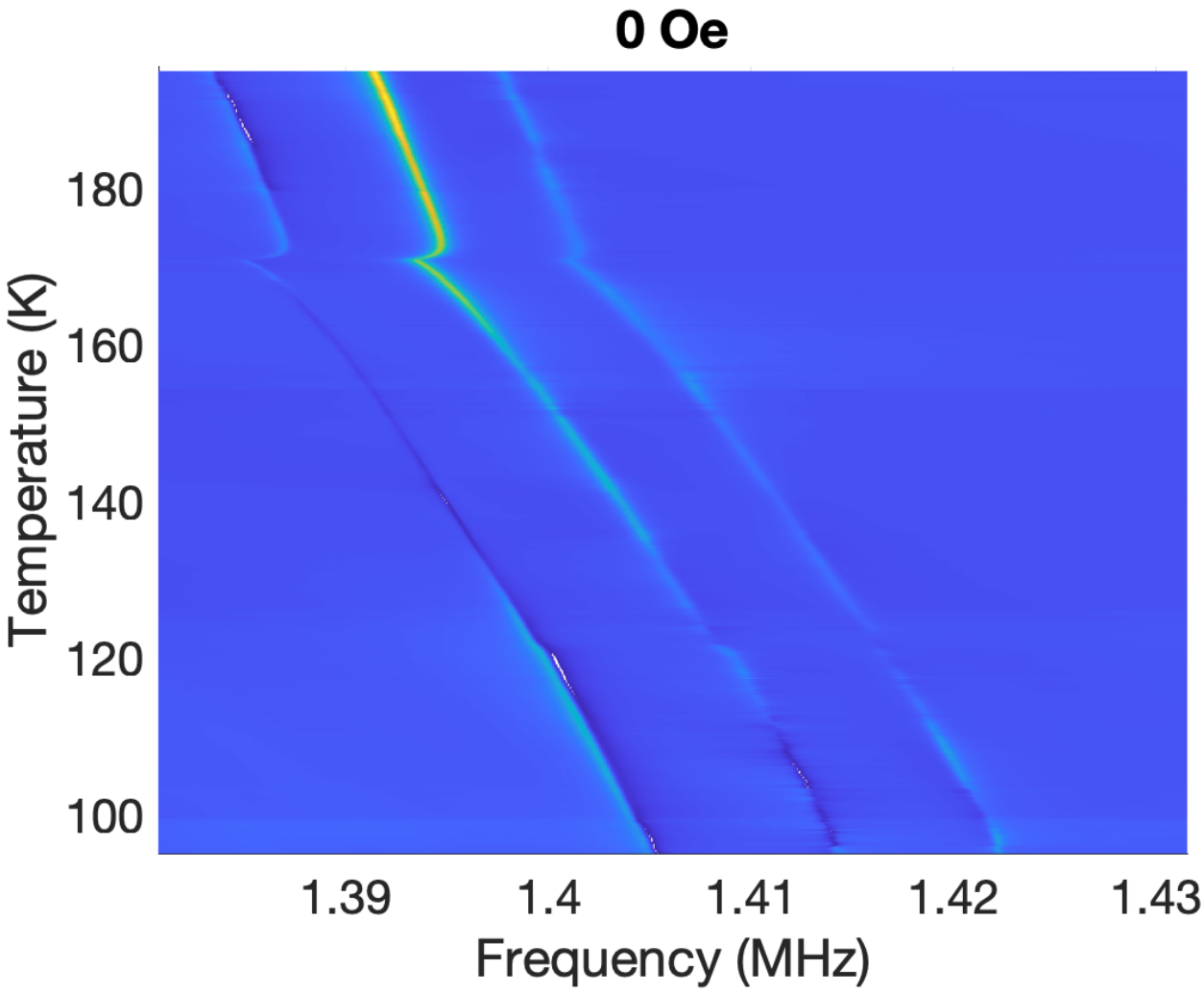

Figure 4.7: RUS scan from 1.38 MHz to 1.44 MHz. The temperature is from 90 K to 190 K. Magnetic field is 0 Oe.

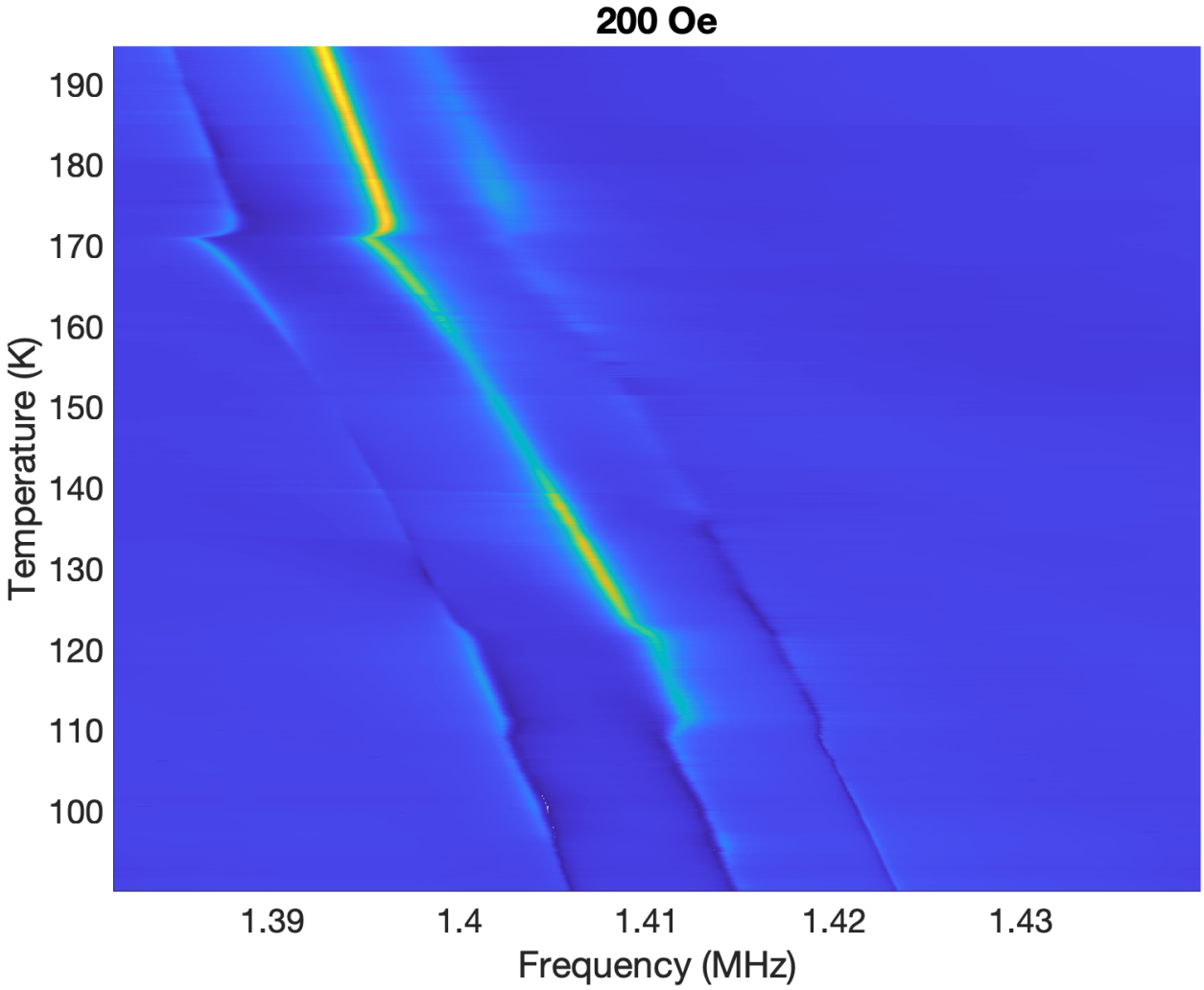

Figure 4.8: RUS scan from 1.38 MHz to 1.44 MHz. The temperature is from 90 K to 190 K. Magnetic field is 200 Oe.

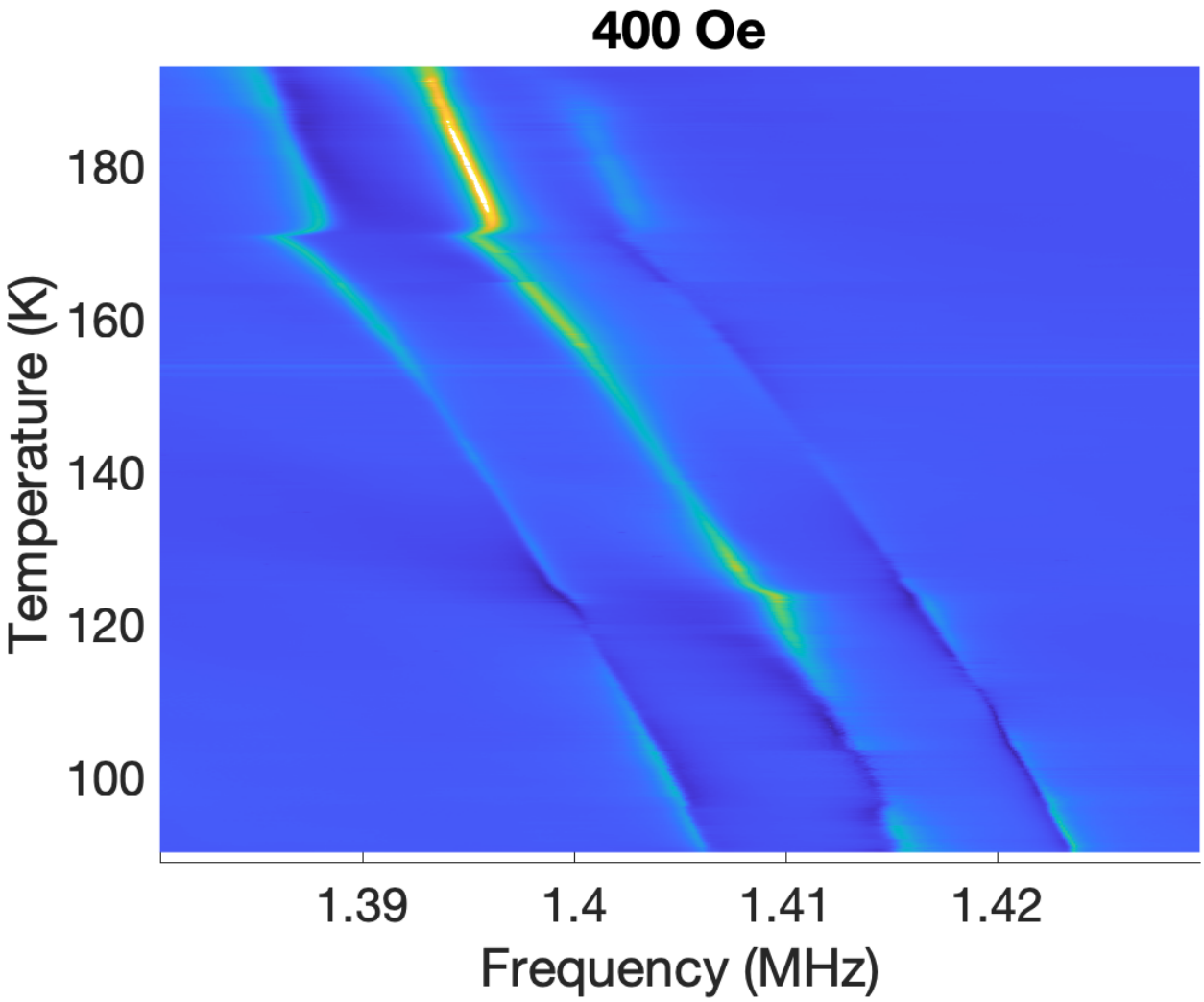

Figure 4.9: RUS scan from 1.38 MHz to 1.44 MHz. The temperature is from 90 K to 190 K. Magnetic field is 400 Oe.

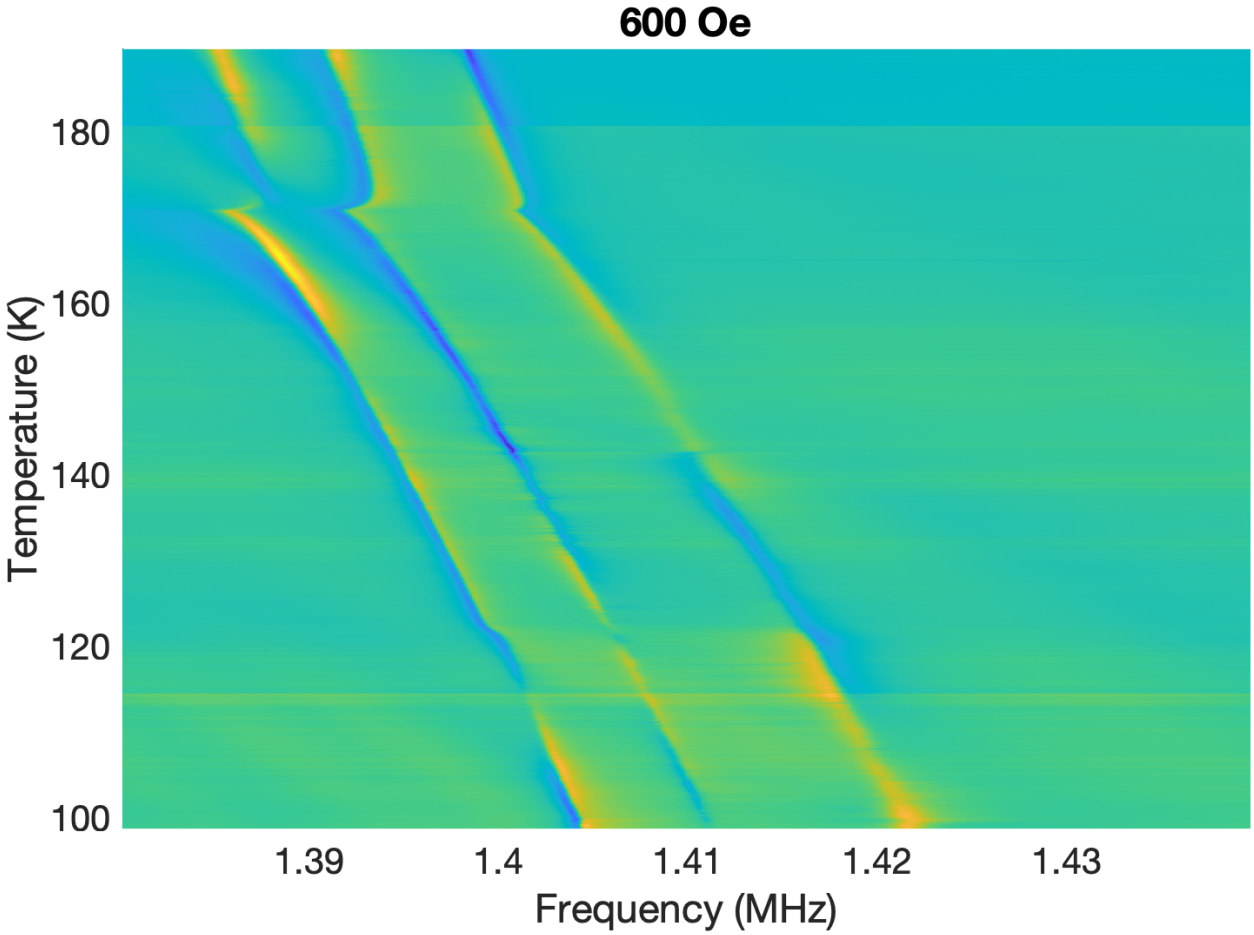

Figure 4.10: RUS scan from 1.38 MHz to 1.44 MHz. The temperature is from 90 K to 190 K. Magnetic field is 600 Oe.

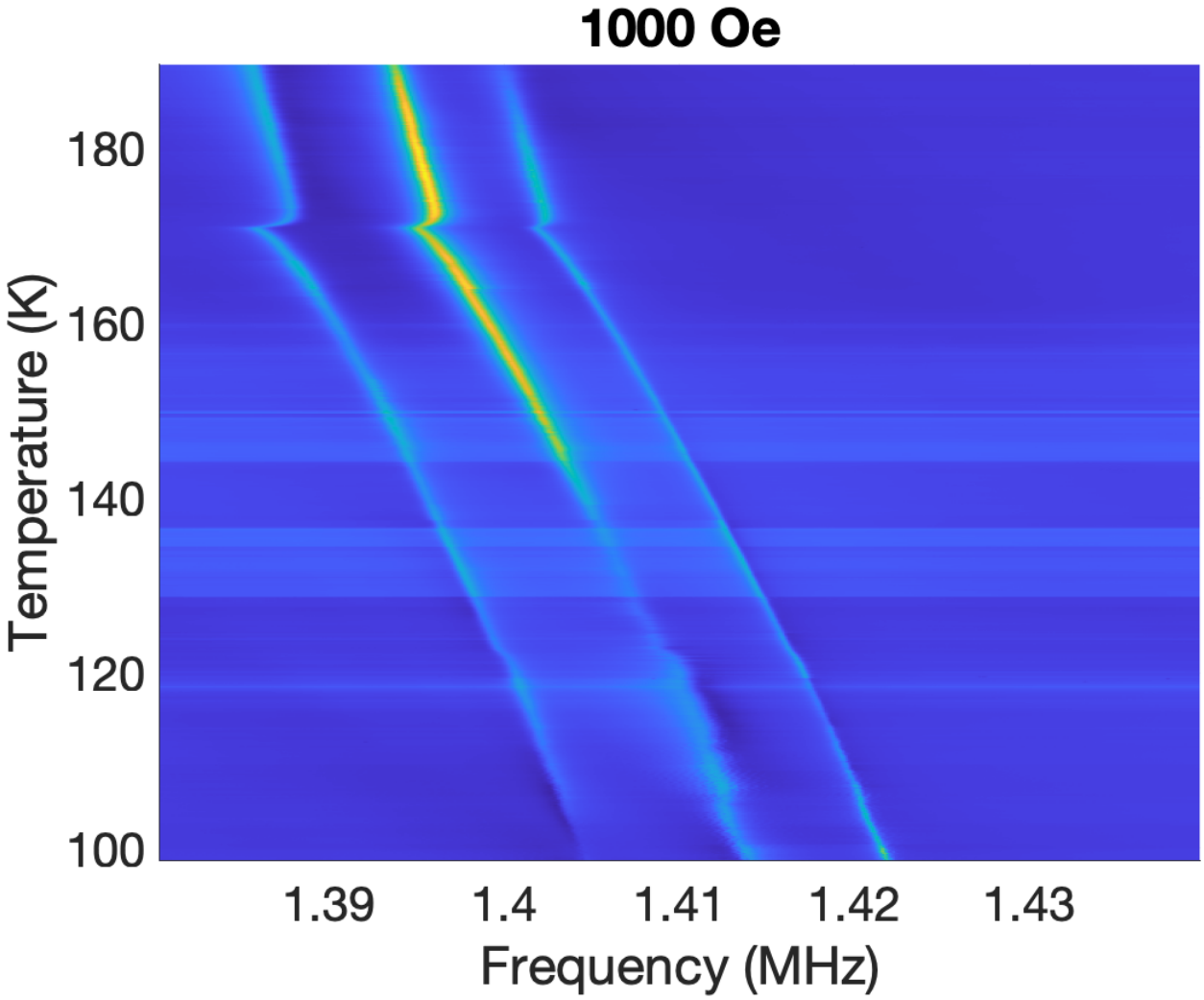

Figure 4.11: RUS scan from 1.38 MHz to 1.44 MHz. The temperature is from 90 K to 190 K. Magnetic field is 1000 Oe.

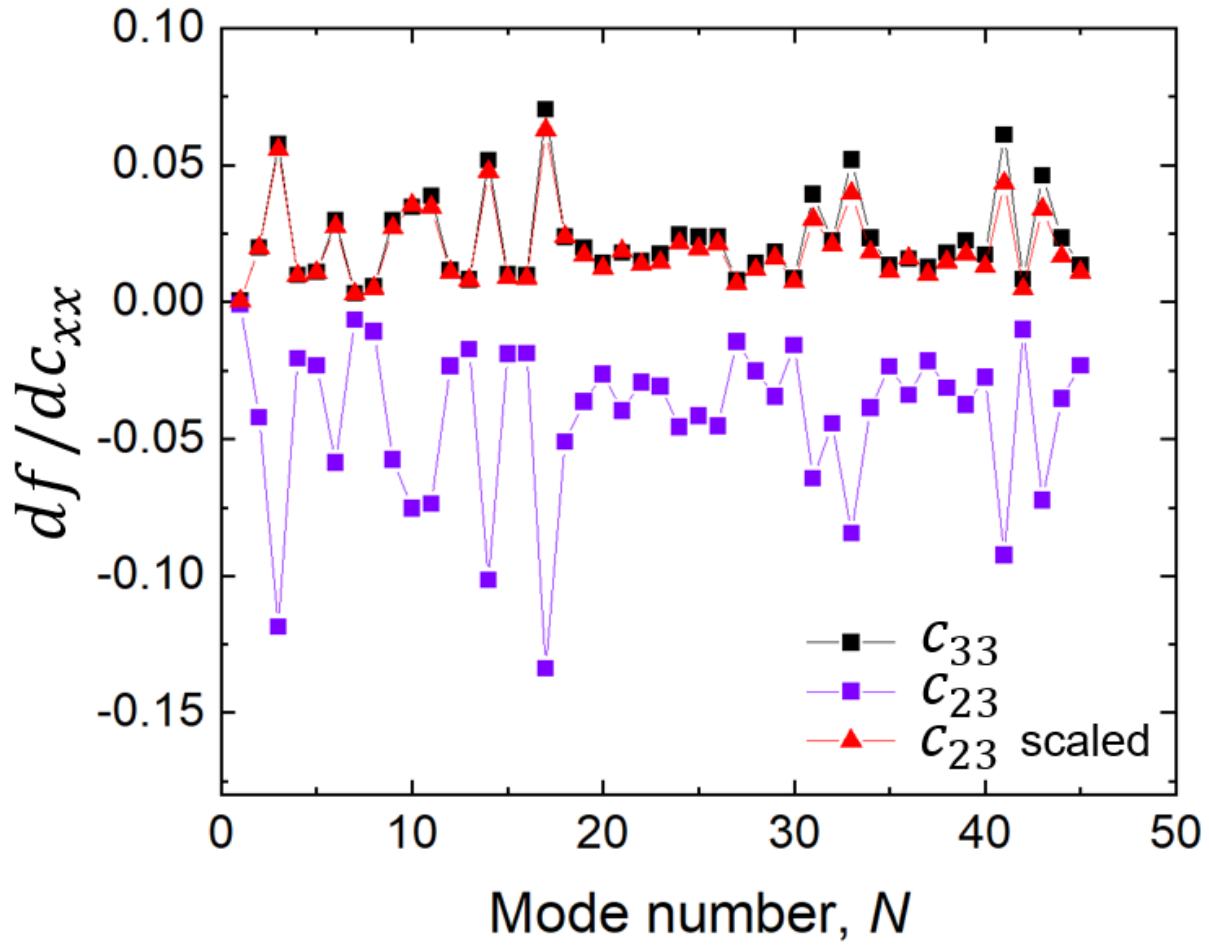

Figure 4.12: Dependence of each resonant mode with frequency f on each elastic constant, c_{33} and c_{23}. A scale factor of -0.47 was applied to data for c_{23} (red triangles). Lines serve as guides to the eye.

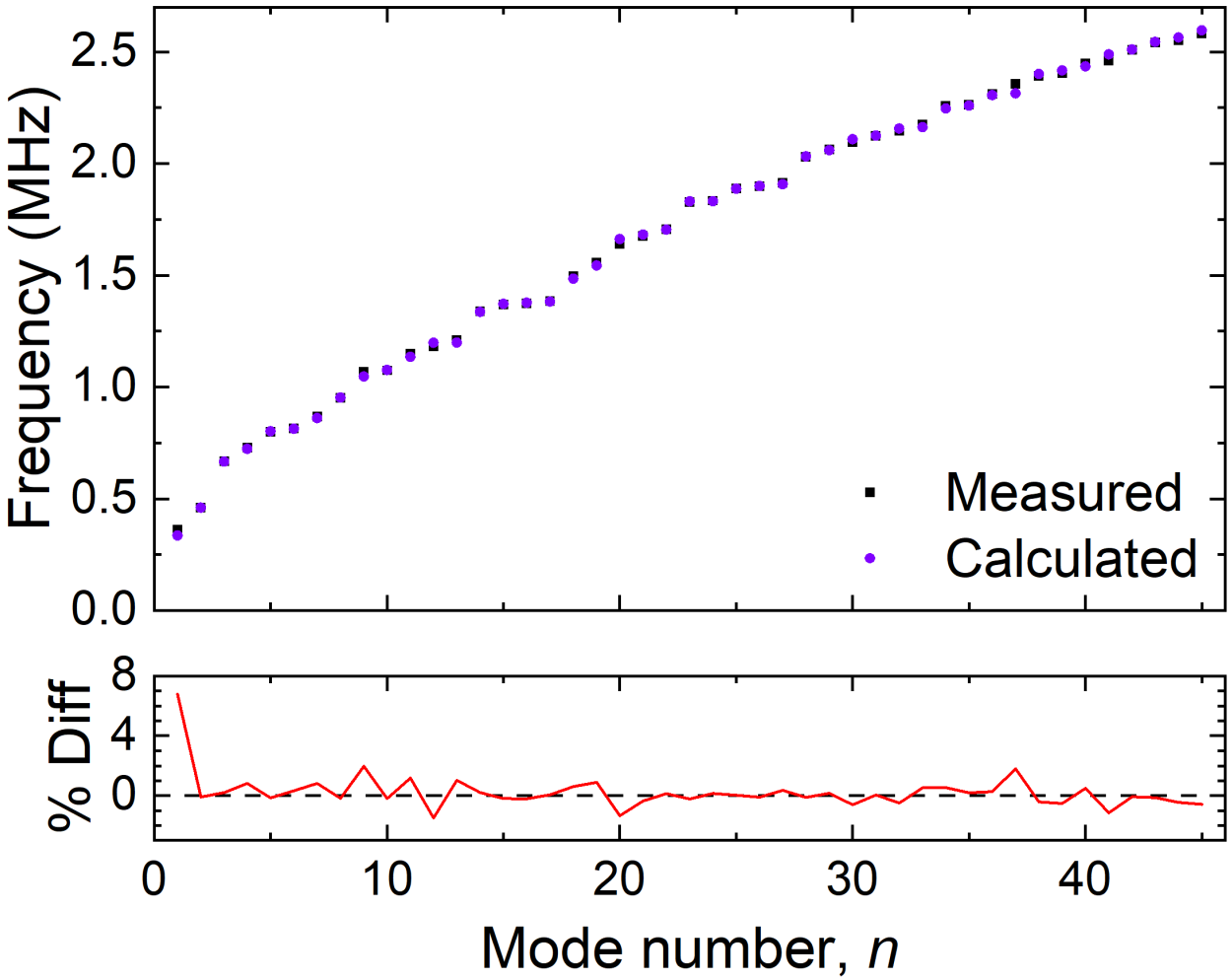

Figure 4.13: Shift in resonant frequency relative to the measured value at 88 K and attenuation factor Q^{-1} as a function of temperature.

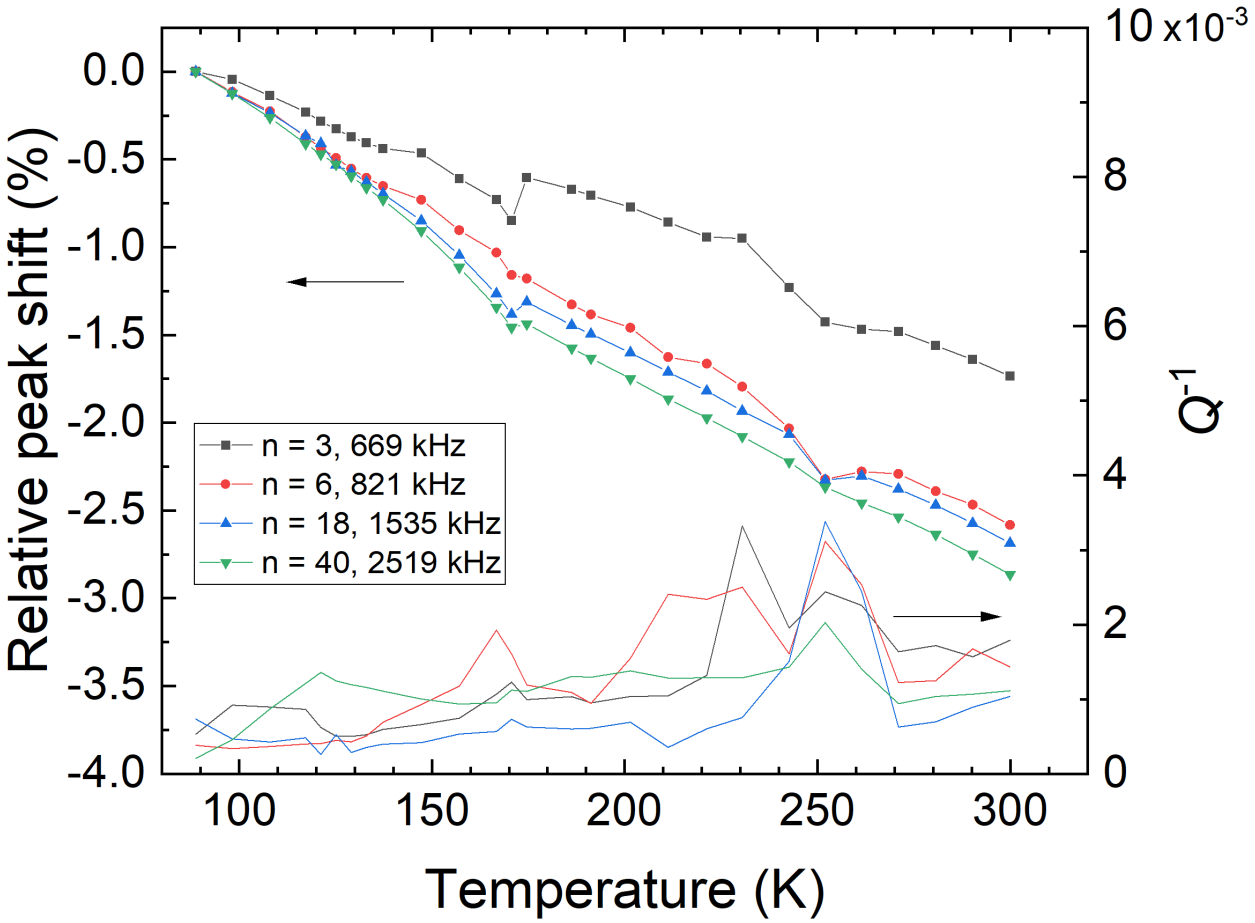

Figure 4.14: Comparison between the measured and calculated frequencies of 45 modes.

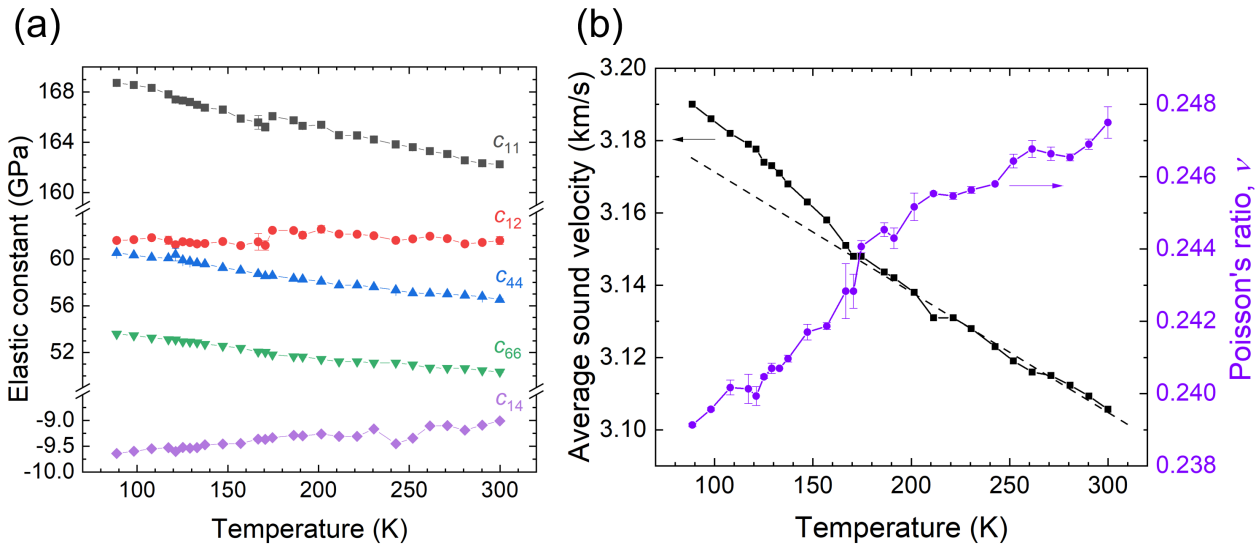

Figure 4.15: Temperature dependence of (a) the elastic constants and (b) sound velocity and Poisson's ratio. Note the breaks in the vertical axis in (a). Lines serve as guides to the eye. The dashed line in (b) corresponds to the line of best fit to data above 170 K.

Vita

Rui Xue was born in Luoyang, Henan, China. She went to Shandong Normal University to study physics in 2011. In the year 2013, Rui traveled to the U.S. as an exchange student at East Tennessee State University. After getting her bachelor of science in physics, she went to the University of Tennessee, Knoxville, to accomplish her Ph.D. degree in condensed matter Physics. She is expected to receive his Ph.D. in August of 2022.